BERGISCHE UNIVERSTÄT WUPPERTAL

Fakultät für Elektrotechnik, Informationstechnik und Medientechnik

Spatial atomic layer deposition of electrically (non-)conductive gas diffusion barriers

zur Erlangung des akademischen Grades eines Doktors der Ingenieurwissenschaften (Dr.-Ing.) genehmigte

Dissertation

von M.Sc. Lukas Hoffmann

Referenten:
Prof. Dr. rer. nat. Thomas Riedl
Prof. Dr.-Ing. Wolfgang Kowalsky

Eingereicht am: 23.04.2018
Mündliche Prüfung am: 08.06.2018

Die Dissertation kann wie folgt zitiert werden:

Vorwort / Preface

Die vorliegende Arbeit entstand im Rahmen einer wissenschaftlichen Tätigkeit am *Lehrstuhl für Elektronische Bauelemente* an der Bergischen Universität Wuppertal. Die Arbeit basiert auf den Projektinhalten zum BMBF Projekt *ANAKONDA*, geht aber hinsichtlich elektrisch leitfähiger Gasdiffusionsbarrieren sowie deren Umsetzung in Perovskit-Solarzellen weit über die im Projekt gesteckten Ziele hinaus. Im Rahmen dieser Dissertation sind vier wissenschaftliche Veröffentlichungen (Ref.[1–4]) und mehrere internationale Konferenzbeiträge entstanden.

An erster Stelle gilt mein Dank meinem Doktorvater Prof. Dr. rer. nat. Thomas Riedl für die Möglichkeit zur Anfertigung dieser Dissertation. Seine fachliche Betreuung sowie die wertvollen Ratschläge hinsichtlich der wissenschaftlichen Veröffentlichungen haben mir sehr weitergeholfen, den Fokus für das Wichtige beizubehalten. Vielen Dank! Prof. Dr. Wolfgang Kowalsky danke ich für die Übernahme des Koreferats und die schnelle Anfertigung des Gutachtens. Ein herzlicher Dank gilt auch Dr. Detlef Theirich, dessen Projektleitung ich sehr zu schätzen gewusst habe. Seine sachliche, unaufgeregte Art war grundlegend für die erfolgreiche Umsetzung der Projektpläne und schuf die Basis für die daraus entstandenen Veröffentlichungen und Konferenzbeiträge. Weiterhin möchte ich mich bei Tim Hasselmann bedanken, der mich in Form von Bachelor- und Masterarbeit, sowie als wissenschaftlicher Mitarbeiter über die komplette Zeit der Promotion unterstützte. Zudem danke ich Kai Brinkmann für seinen nimmermüden Einsatz bei der Erstellung unserer Veröffentlichung zu Perovskit-Solarzellen.
Zudem bin ich sehr dankbar für die jederzeit freundliche und couragierte Zusammenarbeit am Lehrstuhl. Dafür danke ich den aktuellen, sowie ehemaligen Mitarbeitern Dr.-Ing. Ralf Heiderhoff, Dr.-Ing. André Räupke, Dr.-Ing. Andreas Behrendt, Dr.-Ing. Sara Trost, Dr.-Ing. Kirill Zilberberg, Dr.-Ing. Morteza Fakhri, Karsten Brennecke, Andreas Makris, Tim Becker, Tobias Gahlmann, Tobias Haeger, Manuel Theisen, Neda Pourda-

Abstract

The objective of this study is the spatial atomic layer deposition of conductive and non-conductive gas diffusion barriers as promising high performance encapsulation layers in flexible electronic devices. Aluminum oxide and tin oxide are deposited in spatial ALD with TMA and TDMASn. Water, ozone and an Ar/O_2 plasma are used as oxidants. Water vapor transmission rates in the range of 10^{-5}-$10^{-6}\,gm^{-2}d^{-1}$ are achieved at deposition temperatures between 80-150°C. In addition, the deposited tin oxide thin layers provide electrical conductivities in the range of 50-100 $(\Omega cm)^{-1}$. Both material systems show high optical transmittance as well as reasonable mechanical flexibility at substrate velocities up to 4.5m/min. Tin oxide layers are used exemplarily as barrier layers in perovskite solar cells, providing long-term (heat and moisture) stable perovskite solar cells with power conversion efficiencies around 13%. All in all, the deposition of gas diffusion barriers in a roll-to-roll compatible spatial ALD is demonstrated, enabling large-scale continuous encapsulation of flexible electronic devices.

Contents

List of Figures

List of Tables

Abbreviations and symbols

Abbreviation	Description
Al_2O_3	Alumininum oxide
ALD	Atomic layer deposition
AP ALD	Atmospheric pressure ALD
APP ALD	Atmospheric pressure plasma ALD
Ag	Silver
Ar	Argon
C	Carbon
Ca	Calcium
CB	Conduction band
CVD	Chemical vapor deposition
DBD	Dielectric barrier discharge
DMA	Dimethylamine
FF	Fill factor
GDB	Gas diffusion barrier
GPC	Growth per cycle
H_2	Molecular Hydrogen
H_2O	Water
HDMA	Hexamethylendiamine
ITO	Indium tin oxide
LP ALD	Low pressure ALD
N_2	Molecular Nitrogen
O_2	Molecular Oxygen
O_3	Ozone
OH-	Hydroxyl-group
OLED	Organic light emitting diode
PCE	Power conversion efficiency
PE ALD	Plasma enhanced ALD
PVD	Physical vapour deposition
PSC	Perovskite solar cell
RT	Room temperature
SALD	Spatial ALD
S-DBD	Surface dielectric barrier discharge

Abbreviation   Description

Abbreviation	Description
Sn	Tin
SnO_x	Tin oxide
TCO	Transparent conductive oxide
TDMASn	Tetrakis dimethylamino tin
TiO_x	Titan oxide
TMA	Trimethylaluminium
VB	Valence band
ZnO	Zinc oxide
ZrO_2	Zirconium dioxide

Symbol   Description

Symbol	Description
α	Absorption coefficient
A	Area
c	Concentration
C_s	Sorption sites density
D	Diffusion coefficient
δ	Thickness of the boundary layer
d_d	Momentum diffusion length
e	Electric charge of an electron
E	Energy
η	Dynamic viscosity
h	Gap height (between substrate table and ALD head)
I	Current
I_L	Light intensity
$I_{L,0}$	Initial light intensity
J	Current density
J_{Ph}	Photo current density
J_{diff}	Diffusive flux
k	Extinction coefficient
k_B	Boltzmann constant
L_H	Width of the hydrodynamic entrance region

Symbol	Description
λ	Wavelength
M_{Ca}	Molar mass of calcium
$M_{Ca(OH)_2}$	Molar mass of calcium hydroxide
M_{H_2O}	Molar mass of water
M_{O_2}	Molar mass of oxygen
μ	Electron mobility
n	Refractive index
n_{pn}	Ideality factor of the Shockley equation
N	Amount of substance
ν	Kinetic viscosity
p	Pressure
P	Permeation coefficient
P_{in}	Incoming power
ρ	Density
R	Universial gas constant
R_e	Reynolds number
$d\sigma/d\Omega$	Cross section
t	Time
τ	Shear stress
T	Temperature
V	Voltage, Volume
Y	Precursor yield
Z	Atomic number

1

Introduction

With the increasing demand for thin film technologies and their miniaturization towards smaller, flexible or even transparent electronic devices, gas diffusion barriers (GDBs) are mandatory to protect the (photo)active materials. The integrity of those sensitive thin layers is essential for the lifetime of the devices. In a wide field of electronics, gas diffusion barriers are applied as an encapsulation against attacks by environmental gases, e.g. moisture and oxygen.[5–7] In another scenario, barrier layers are desired to prevent the diffusion of species orginating from constituents inside the device. In this case, these layers are aimed to shield the rest of the device from ambient gases and simultaneously to prevent corrosive constituents to migrate through the device, e.g. in a perovskite solar cell (PSC) or an organic light emitting diode (OLED).

In the late 2000s, glass could be seen as gold-standard in terms of gas diffusion barriers for the top-encapsulation.[8] Linked to this glass encapsulation, there are several drawbacks like the rigidity of the devices and the incompatibility of the fabrication process with low-cost, continuous manufacturing. Here, the economic viability of a commercial nanotechnology such as the fabrication of solar cells mainly depends on its products value and its production capacity.[9] To this end, roll-to-roll processes lower the cost and simultaneously increase the throughput in the manufacturing of these devices. Furthermore, in roll-to-roll processes, it is desired to use flexible and light weight polymer foils as substrates, which also reduce the overall weight of the devices. Due to the typi-

cally high water permeability of those plastic materials, it is essential to add appropriate thin film gas permeation barriers onto the plastic substrate. As a result, high performance gas diffusion barriers with ultralow water vapor transmission rates (WVTRs) are required, enabling the deposition onto foils in a roll-to-roll compatible process. For OLEDs, barriers which transmit $< 10^{-5}\,\mathrm{gm^{-2}d^{-1}}$ of water are required,[10,11] dramatically exceeding the requirement for the barrier performance for specialized food or medical packaging ($10^{-2}\,\mathrm{gm^{-2}d^{-1}}$).[11]

Atomic layer deposition (ALD) is well known for its controlled self-limiting growth, resulting in dense conformal thin films even at relatively low growth temperatures on the order of 50-100°C.[12–14] Barrier films deposited via ALD have shown very low gas permeability with WVTRs on the order of $10^{-6}\,\mathrm{gm^{-2}d^{-1}}$[13–15] and therefore fullfilled the barrier requirements for e.g. OLED encapsulation.[10] Conventional ALD is a chemical deposition process which is based on the sequential exposure of the surface to be coated by two different chemicals, also known as precursors, which react with their respective counterpart but not with themselves in a surface monolayer reaction. The ALD development dates back to the 1970s.[16] Since then, its principle has been used to deposit a variety of materials, not only metal oxides, but also metals, fluorides and nitrides[17] for a wide field of applications. In general, metal oxide layers prepared by atomic layer deposition provide the most promising avenue to realize functional protection layers. Originally, ALD is a vacuum and batch based deposition process, where precursors are dosed in a dedicated time sequence of pulses and purges. In terms of the roll-to-roll processing spatial ALD (SALD) at atmospheric pressure has been proposed by Levy et al. in 2008.[18,19] In spatial ALD the time separated pulsing is transfered to a spatially separated injection of the precursor/pulse sequence. In the laboratory, an oscillating or rotating substrate movement between the different precursor regimes is used instead of a continuously moving web. As such, this concept is sheet-to-sheet, but also roll-to-roll compatible. The realization of those concepts have already shown growth rates in the order of nm/s and thus the industrial throughput requirements of approximately 3600 wafers/h could be achieved.[20,21] It is therefore not surprising that spatial ALD has been implemented into industry in the last years.[22,23] Nevertheless, the typical oxidant used in spatial ALD is water. Here, plasma assisted processes have been considered to overcome limitations associated with the use of water as oxidant in low temperature ALD processing (e.g., low vapor pressure, high sticking coefficient to wall surfaces).[21,24]

In this thesis, spatial plasma enhanced ALD of conductive tin oxide based and nonconductive aluminum oxide based gas diffusion barriers is presented. Aluminum oxide (Al_2O_3) thin layers (10-200 nm) were deposited by trimethylaluminium (TMA) and different oxidants (Ar/O_2 plasma, H_2O and ozone) at moderate process temperatures

(75-150°C). All barriers were deposited in a home-built plasma-enhanced spatial ALD setup at atmospheric pressure specifically designed for this study. The use of dielectric barrier discharge plasma sources enable the oxidization step of the TMA molecules at atmospheric pressure. The resulting barriers were the first reported ones, deposited by spatial plasma ALD at atmospheric pressures (APP ALD), providing WVTRs on the order of 10^{-5}-10^{-6} $gm^{-2}d^{-1}$.

In addition, first spatial ALD based conductive gas diffusion barriers based on tin oxide (SnO_x) are reported. Their electrical conductivity and high optical transmittance allowed to integrate them as functional charge transport layer into the device stack of a perovskite solar cell. Over the past few years those hybrid halide perovskite solar cells have seen an unprecedented progress as power conversion efficiencies (PCEs) have reached a level beyond 20%,[25–27] aiming for the efficiencies of conventional Si-based solar cells. In 2018, the actual record in efficiency for PSCs reached 22.7%.[28] Nevertheless, a serious concern about stability is associated with all perovskite-based solar cells, as the photoactive perovskites tend to decompose upon exposure to moisture and/or elevated temperatures.[5,29–32] In addition, halide-containing species resulting from the decomposition of the perovskite can corrode metal electrodes used in the cells and thereby compromise the device stability.[33,34] Organic, metal oxide, and even modified two-dimensional perovskite capping layers have been proposed to mitigate these stability issues and to enhance the stability of PSCs.[35–42] Although all these concepts achieve some kind of stability improvement, the reported PSCs still face notable long-term degradation, especially when exposed to elevated temperatures. This could be directly related to limited barrier properties of the layer proposed in those studies. Here, conductive gas diffusion barrier layers by ALD come into account. The use of insulating layers inside a device stack is limited to at best a few monolayers through which carriers can still tunnel. In this work, PSCs based on spatial ALD SnO_x with power conversion efficiencies (PCEs) around 13% with excellent long-term stability beyond 1000 h in ambient air and over 3000 h at 60°C are demonstrated.

Furthermore the role of substrate velocity in spatial ALD is investigated. The dependence of the coverage on substrate speed is validated experimentally, but also by gas flow simulations. For both metal oxides (Al_2O_3 and SnO_x) a constant saturation regime in the growth per cycle (GPC) could be found up to substrate velocities up to 40-60 mm/s. The decay in GPC for higher substrate velocities could be directly reasoned by an insufficient precursor supply.

Notation: This thesis is divided into six chapters and based on four scientific journal publications. The physical and chemical fundamentals necessary for the spatial ALD are detailed in the second chapter. Here, the principle of permeation through gas diffusion barriers as well as the thin film growth of ALD is described in detail, creating a basis for the understanding of the experimental observations. In addition, the concept of perovskite solar cells is presented. The spatial ALD system as well the dielectric plasma sources used in this work are discussed in chapter three. In addition, the most dominant measurement techniques are provided: The optical Ca test, Rutherford backscattering Spectrometry (RBS) and Nuclear reaction analysis (NRA). The fourth chapter is about aluminium oxide based gas diffusion barriers deposited by batch-based and spatial ALD at atmospheric pressure as reported in Ref.[1,2] The fifth chapter deals with transparent and conductive SnO_x encapsulation layers grown by spatial ALD and their use as barrier layer in perovskite solar cells (see Ref[3,4]). Chapter six puts special emphasis on the role of substrate speed for the growth of both oxide layers mentioned above, while chapter seven draws a conclusion and gives prospects for future development.

2

Physical fundamentals

In the following, the physical fundamentals for the work done in this thesis will be explained. The chemical fundamentals of conventional and spatially separated atomic layer deposition will be discussed. The concepts provided in this chapter are essential for understanding the functionality and the growth of barrier layers deposited via batch-based and spatial ALD. Gas diffusion barriers will be classified as well as the respective gas permeation mechanisms. As the barrier layers are used, for example, in perovskite solar cells, their functionality will be presented.

2.1 Spatial atomic layer deposition

In this section the physical and chemical basics of (spatial) ALD are presented. First reports on ALD date back to the 1970s in Finland by Suntola et al.,[17,43,44] originally known as ALE, Atomic Layer Epitaxy, a term also used today for atomic layer etching. At the same time, there were reports on *molecular layering* in 1965 in the Soviet Union by Aleskovskii et al.[16] As Suntola et al. used this technique for electroluminescent flat panel displays, in the 1990s ALD attracted increasing interest due to its conformal, well-controlled growth in the field of microelectronics. As with increasing miniaturization

and enlargement of application areas of electronic devices the need for high-throughput on flexible substrates arose, spatial ALD was proposed in 2008.[18,19] Nowadays, ALD is famous for its well-controlled film thickness in the nanometer-scale, its homogeneous coating even in large-scales as well as the capability to conformally coat high-aspect-ratio patterned substrates.[17] For barrier layers, ALD is known to lead to thin films which differ from other thin film deposition techniques by their amorphous, dense character, providing outstanding barrier properties.[45,46] In the following, the fundamentals of conventional ALD and the physical fundamentals of the spatial ALD related parts (especially the gas dynamics inside the ALD reactor and the dielectric barrier discharge plasma source) will be discussed.
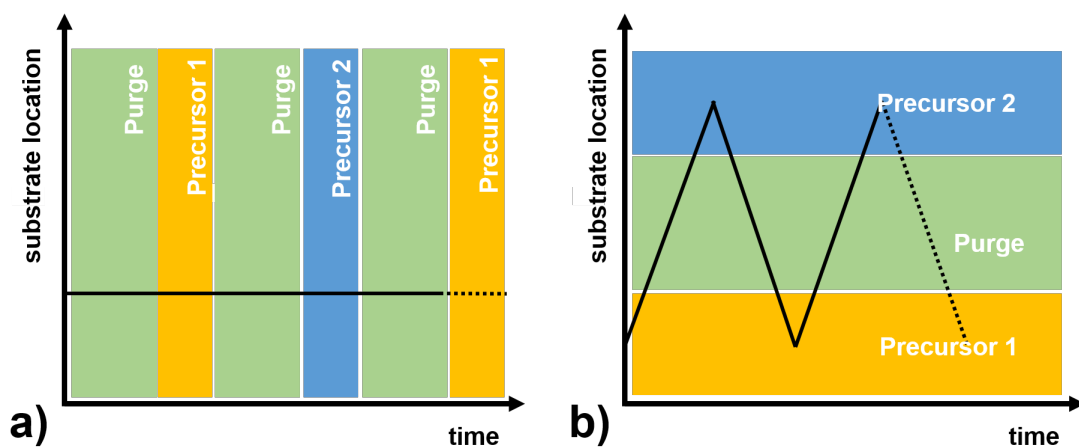
Figure 2.1.: Converting batch-based ALD into spatial ALD means converting the time separated process (a) into an spatially separated (b) one. In the conventional (batch-based) ALD the substrate (black line) is exposed to the different fabrication steps chronologically. In the concept of spatial ALD, this chronology is achieved by the spatial separation of the different precursor and the spatial movement of the substrate. Inspired by Ref.[21]

ALD is the physical process of the binary alternating sequences in which two surface reactions from different precursors take place separated by a purge step. Both precursors can not react by themselves but with the available (finite) surface sites of the other, respectively. Therefore, the process is self-limiting and able to deposit a film with atomic layer level of control. The precursor and purge sequence could be achieved by a time separation or by a separation in space. Separation in space is achieved by the spatial substrate movement with respect to the precursor and purge zones. This concept is illustrated in Figure 2.1. Here, the black line represents the substrate, which is, in case of the conventional batch-based ALD, fixed in space but exposed to the respective ALD step by the alternating purge/precursor dosage. In the case of the spatial ALD, the

purge/precursor zones are fixed in time, but with respect to the substrate not in space. Most commonly, the substrate moves between the different exposure zones. Nevertheless, also a moving precursor head and a simultaneously fixed substrate fulfills the concept of spatial ALD.

2.1.1 Conventional atomic layer deposition

The fundamentals of spatial ALD are based on the chemical reactions which take place also during the conventional (batch-based) atomic layer deposition. Therefore, the ALD reaction is commonly based on a chemical reaction between two precursors. Most commonly, ALD is used to deposit metal oxides, but also nitrides, chalcogenides and even metals are applicable.[45] In terms of the ALD of metal oxides, a metal oxide precursor and its oxidant is used, which provides the exchange of the metal ligands. As ALD is a type of chemical vapor deposition, both reactants are gaseous, commonly achieved by exploiting the vapor pressure of liquid or solid precursors. Due to this, metal-organic or metal-halide compounds which fullfill the mentioned demands are suited as precursors. Basically those precursors differ in their ligands, or in other words, which molecules are bonded covalently to the respective central metal atom. Here, akyles (like trimethyl aluminium or diethyl zinc) are probably the most common precursors. In akyles the metal compound is bonded to ligands such as $-CH_3$. Another widely disseminated precursor group is the akyl amides (like TDMATi or TMDASn). Generally, both precursor groups enable the deposition of nitrides, oxides and even sulfids.[47] But also cyclopentadienyls or β-diketonates permit the deposition of a variety of metal based ALD films.[48,49] Choosing the suitable precursor/co-reactant system is always a trade-off between chemical reactivity, vapor pressure, thermal stability, toxicity but also price and resulting film properties. The latter could be strongly dependent on the precursor/co-reactant system e.g. tetrakis dimethylamido titanium (TDMATi), titanium isopropoxide (TTIP) and titanium chloride ($TiCl_4$) as precursor for TiO_2 films.[50]

In the following, the ALD principle should be explained by the most common precursor system, TMA and water, whose deposition is also demonstrated experimentally in this thesis. A schematic of this chemical process is shown in Figure 2.2. Steps 1 to 4 are composited and called one cycle of ALD. At the beginning of this cycle the TMA molecules, which consist of one aluminum atom (Al) and three methyl groups (CH_3), are dosed into the reaction chamber (or in terms of spatial ALD onto the substrate) and react with
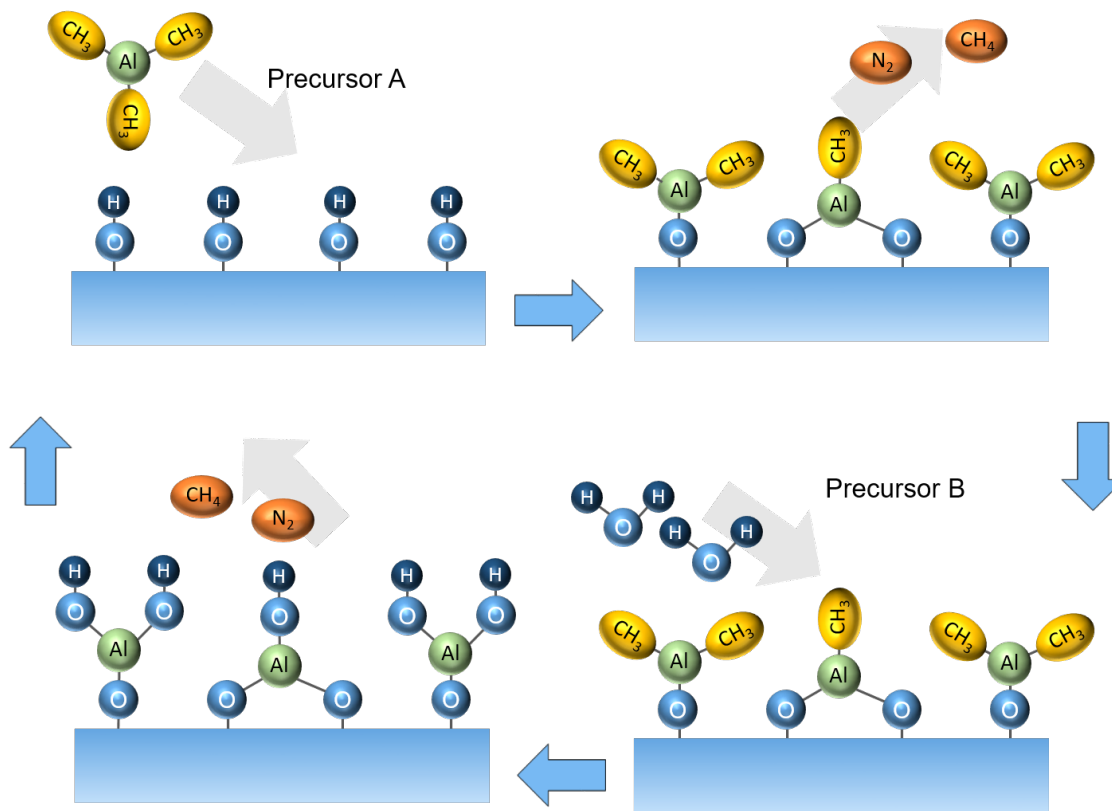
Figure 2.2.: Schematic depiction of the chemistry of the TMA/water ALD reaction. The ALD chemistry can be divided into four parts: Exposure of precursor A (TMA) (1) Inert gas purge step (2,4), Exposure of precursor B (H_2O) (3). Both precursor exposure steps are self-limiting and thus limited to the reacting surface sites underneath. The chemical reactions are represented in Equation 2.1-Equation 2.3, respectively. Note that the deposition takes place on an substrate with an -OH-based surface.

the surface as described in Equation 2.1.

$$Al-OH^* + Al(CH_3)_3 \longrightarrow AlO-Al(CH_3)_2{}^* + CH_4 \quad . \tag{2.1}$$
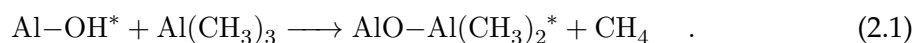
The *-mark refers to surface-bound species. The free methyl group reacts with the hydrogen of the hydroxyl group to methane (CH_4). Ideally, this reaction takes place until all free OH-bonds have reacted. Then, no further TMA molecule can be bound to the surface. Therefore, the reaction is called self-limited. In the second part the surface is purged with an inert gas (e.g. N_2 or Ar). All residual gas molecules (e.g. CH_4) are removed from the deposition zone. In the third step, the surface gets exposed to the second precursor (H_2O). One hydrogen atom of the respective water molecule reacts with the methyl group, orginally bonded to the aluminum atom, leaving AlOH at the

surface, as well as a free gaseous methane molecule:

$$\text{AlCH}_3^* + \text{H}_2\text{O} \longrightarrow \text{AlOH}^* + \text{CH}_4 \quad . \tag{2.2}$$

The OH-compound bonded to the aluminum atom reacts again with nearby methyl group leaving Al-O. If all free methyl groups were hydrolyzed by the water molecule, self-limitation is given. No further reaction can take place. All residual byproducts are purged again in step four. Both reaction equations can be summed up to:

$$2\text{Al}(\text{CH}_3)_3 + 3\text{H}_2\text{O} \longrightarrow \text{Al}_2\text{O}_3 + 6\text{CH}_4 \quad . \tag{2.3}$$
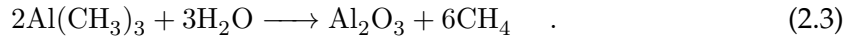
Equation 2.3 describes the overall reaction for the TMA/water-based ALD. Other systems could be characterized analogously, e.g. the reaction of TDMASn with H_2O. The corresponding chemical reaction equations are[51,191]

$$(\text{OH})_x^* + \text{Sn}(\text{DMA})_4 \longrightarrow (\text{O})_x\text{Sn}(\text{DMA})_{4-x}^* + x\text{HDMA} \tag{2.4}$$

$$(\text{O})_x\text{Sn}(\text{DMA})_{4-x}^* + 2\text{H}_2\text{O} \longrightarrow (\text{OH})_x^* + \text{SnO}_2 + (4-x)\text{HDMA} \quad . \tag{2.5}$$
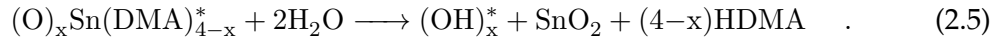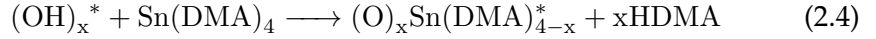
Here, DMA represents the dimethylamino ligand while the HDMA compound is called the dimethylamine, which is released to the gas phase (analogous to CH_4 molecules in the TMA/H_2O reaction). The x represents the number of ligands released during the TDMASn pulse. Commonly, on average $x = 2.5$ is reported for H_2O as co-reactant,[51] while other co-reactants (as H_2O_2, or O_3) lead to a somewhat higher x value, strongly dependent on the temperature.

Generally, growth could only take place when a surface site is accessible to the precursors of the subsequent cycle. The resulting surface coverage (e.g. the film growth) could be described after the so-called Langmuir adsorption model.[52] The Langmuir adsorption model is based on a finite number of surface site applicable for film growth. The resulting coverage of surface sites with a precursor or molecule Q in dependency on a precursor partial pressure p could be expressed as:

$$Q = \frac{k_1 \cdot p}{k_2 + k_3 \cdot p} \quad . \tag{2.6}$$

This term is normally called the langmuir adsorption isotherm. k_1 - k_3 are coefficients containing the surface concentration of the respective molecule as well as the concentration of bare sites. Especially, $k_2 = 1$ is called the Redlich-Peterson isotherm.[53]

In general, the growth rates measured for ALD processes are lower than expected for optimal surface saturation. On the one hand, this is reasoned by a lower number of surface bonding sites as required for the maximum ligand coverage. As a consequence, free space remains on the surface even when the reaction is self-terminated. The second factor for lower growth rates is called the steric hindrance, shown in Figure 2.3. Steric hindrance describes the physical blocking of reaction sites by overlaying ligands, attached to their neighboring sites, respectively.[54] As the CH_3 ligands block part of the surface which would be accessible for the reactants, the surface could be considered occupied or saturated.
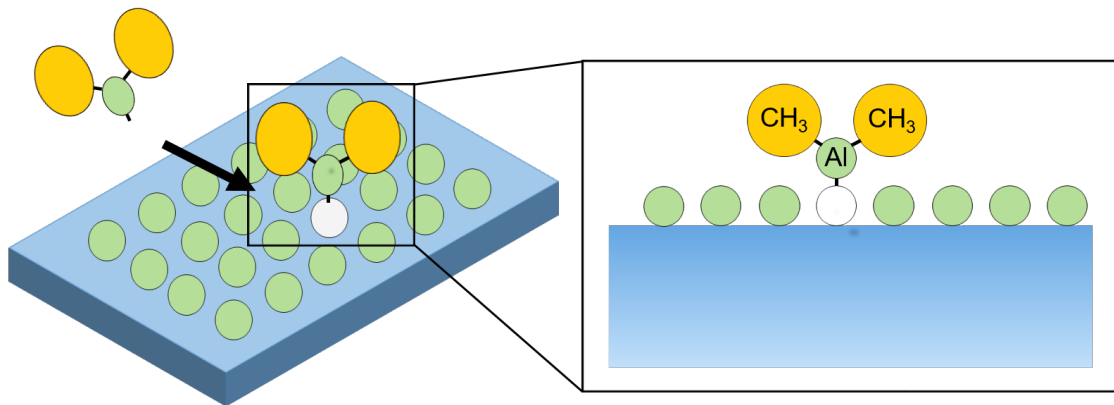
Figure 2.3.: Schematic illustration of the principle of the steric hindrance in ALD film growth (represented by the TMA molecule). Groups of methyl ligands block the reaction sites physically, which are no longer accessible for the respective reactants.

Generally, this chemical description of the ideal ALD growth is valid in a certain temperature regime. Here, the concept of the ALD window is the common description of the temperature-dependent growth rate, illustrated in Figure 2.4. It provides a temperature regime (the ALD window) in which ALD type of growth takes place and in which both half reactions are prevented from condensation, decomposition or desorption of the respective chemical compound. Towards lower process temperatures the necessary reaction (activation) energy (given by the process temperature) could not be guaranteed, leading to slow or even incomplete precursor reactions with lower growth rates. An increased growth rate at low temperatures can be explained by the condensation of precursor material on a too cold substrate surface, not corresponding to the principle of self-saturated ALD. At higher deposition temperatures the surface species can desorb (and lead to lower growth rates) or decompose leading to additional CVD reaction in the gas phase.[17] Inside the ALD window, the growth rate is almost constant, strongly dependent on the precursor and oxidant used in the process.
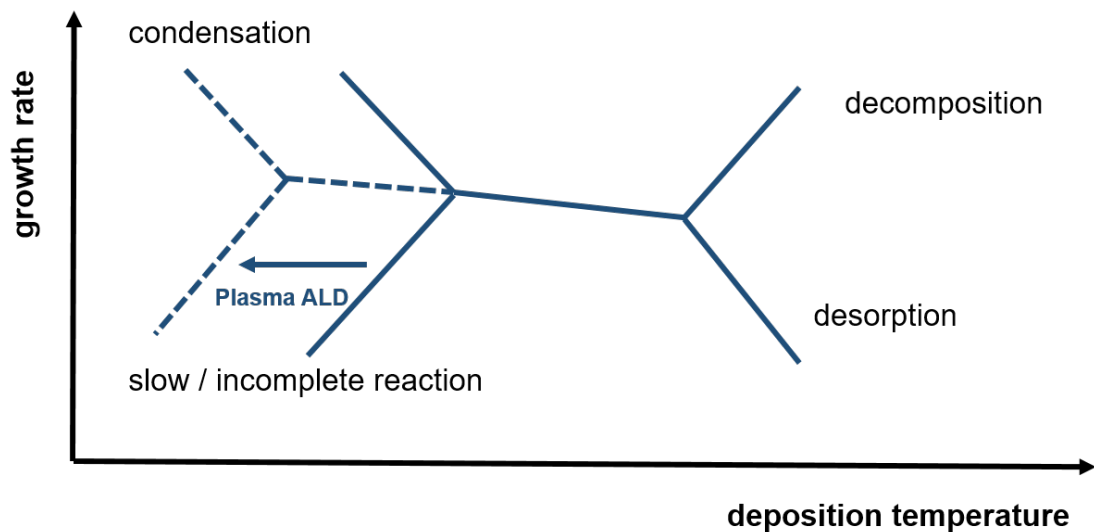
Figure 2.4.: The tpyical ALD window for metal oxide chemistry. Dependency of the deposition temperature on the growth rate. Condensation, desorption, decomposition or slow (or even incomplete) reactions are possible processes outside the ALD window (towards higher or lower deposition temperatures). Inspired by Ref.[55]

For most metal oxide systems, temperature regimes typically span from 80-100°C to 400°C, where the growth rate slightly decreases with increasing temperature, exemplified by the gradual loss of surface groups with increasing substrate temperatures.[56] Therefore, a change in growth rate does not always indicate whether the thin film growth shows ALD characteristics or not. On the other hand, some precursor systems do not show an ALD window at all or the corresponding ALD windows starts at temperatures exceeding the limits of other compartments e.g. in heat-sensitive organic solar cells or perovskite solar cells. A method to widen the ALD window is the use of other oxygen sources than water, e.g. ozone or plasma. The concept of plasma enhanced ALD is described in the following section.

2.1.2 Plasma enhanced atomic layer deposition

In plasma enhanced ALD (PE ALD) plasma is used to generate the desired radical or reactive species necessary for the second half-reaction in the ALD cycle. This technique was first reported in 1991. Kejser et al. deposited gallium arsenide with the use of atomic hydrogen (H^+) generated by a plasma.[57] In general, the plasma species does not necessarily need to become part of the deposited layer, but it may as well serve as reducing agent, e.g. in ALD of pure metals like silver or copper.[58,59] Here, species as H can re-

duce the surface ligands and lead to the formation of pure metal thin films. Plasma ALD is considered favorable in literature due to the high reactivity of the plasma species on the deposition surface. Thus, plasma ALD provides more freedom in processing conditions and a wider range of material properties than achieved with conventional thermal ALD.[60] In addition, plasma enhanced ALD enables the deposition at lower substrate temperatures and therefore the enlargement of the ALD window, as illustrated in Figure 2.4. For most cases, the GPCs for plasma enhanced ALD are reported to be higher compared to those resulting from conventional ALD,[55,61,62] due to the high reactivity of the plasma and a higher density of reactive surface sites. Exemplary, the reaction of plasma generated species with TMA can be described by:[60]

$$AlCH_3^* + 4\,O \longrightarrow AlOH^* + CO_2 + H_2O \qquad . \qquad (2.7)$$
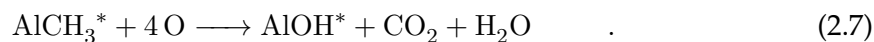
In plasma ALD, the substrate is either located directly inside the plasma discharge or close to it. Those approaches are labeled with different notations in literature. When the substrate position is located near, or even inside, the plasma, the process is called the *direct plasma* ALD or just *plasma enhanced* ALD (PE ALD). When the plasma is spatially separated from the substrate, the terms *radical enhanced* ALD or *remote plasma* ALD are used to label the process conditions. In linear flow reactors the remote position is also called the *downstream* position.[60] The latter is distinguished from radical enhanced ALD by the influence of the electron and ion densities, which have not decreased to zero on the surface of the substrate.[63,64] For this reason, the distance between the plasma discharge and the substrate is of special importance, resulting in different radical fluxes. The interaction of these plasma-based species and the surface can be seen is the major advantage of PE ALD.[55] With the use of plasma, highly reactive ions, metastable states or UV photons are generated and enabled to reach the substrate surface. This bombardment can also provide additional energy necessary for the ligand-reactant reaction or to enhance the mobility of single ligands resulting in improved film forming reactions. In the radical enhanced plasma ALD, the bombardment of (highly) energetic ions and electrons on the substrate is eliminated due to the larger distance and low lifetimes of those particles. In terms of atmospheric plasma ALD this elimination is increased as the increased pressure favors particles collision linked with shorter (ion) lifetimes.

2.1.3 Gas kinetics

Gas kinetics plays an important role for the precursor distribution below the ALD head. Even if the ALD head is designed without any knowlegde of computational simulations, the latter helps to understand and to classify the experimental results. Generally speaking, two parameters define the nature of the gas kinetics under the ALD head: The *Reynolds number* and the the *Knudsen number*. To evaluate if the gas kinetics in the ALD head are of turbulent or laminar nature, the Reynolds number is crucial. To estimate if the pathway of the gas can be simulated by a continious mass flow rather than discrete particles, the so-called Knudsen number comes into account. In the following, both parameters were calculated considering typical SALD dimensions. The Reynolds number R_e, already presented by Arnold Sommerfeld in 1908, is defined by the product of the gas density ρ, its velocity v and the characteristic length d devided by its dynamic viscosity η:[65]

$$R_e = \frac{\rho v d}{\eta} = \frac{v d}{\nu} \qquad . \tag{2.8}$$

This equation is valid, since the dynamic viscosity η is the quotient of the kinetic viscosity ν divided by the density ρ. In the case of spatial ALD used in this work the 1 mm wide pipes are a typical system length. As such, the Reynolds number results in:

$$R_e = \frac{\rho v d}{\eta} = \frac{1.165 \frac{kg}{m^3} \cdot 0.2 \frac{m}{s} \cdot 1\,mm}{1.76 \cdot 10^{-5} \frac{kg}{ms}} = 13.6 \tag{2.9}$$

Here, d is the width of the entrance of the gas flow and set to 1 mm and v to $0.2\frac{m}{s}$ due to the 1000 sccm (typical point of operation for the flow rate) passing the precursor or purge slits. The dynamic viscosity μ is set to 1.76 kg m^{-1}s^{-1}.[66] As the resulting value is more than two orders of magnitude lower than the critical value $R_{e,crit}$ = 2300 (or $R_{e,crit}$ = 2000 originally proposed by Reynolds[65]), the gas kinects could be seen as laminar.[67,68] Even for the gas flow in the gap between substrate table and ALD head (which is roughly 300 μm high) the gas kinetics can be seen as laminar as the corresponding Reynolds number could be calculated analogous to R_e = 6.82.

Furthermore, the gas particle collision must be prefered over the collision of the gas particle and the wall (of the domain). Therefore, the Knudsen number is expressed by the mean free path of the particles (λ) divided by the physical (characteristic) length.[69] The mean free path is defined as:

$$\lambda = \frac{RT}{\sqrt{2} \cdot N_A \cdot \sigma \cdot p} \qquad . \tag{2.10}$$

Here, R expresses the universal gas constant ($R = 8.314 \, \mathrm{J(Kmol)^{-1}}$), N_A is the Avagadro number and $\sigma = 0.43 \cdot 10^{-18} \, m^2$ the collision cross section of N_2.[70] The mean free path of the particles equals:

$$\lambda = \frac{8.134 \, J(Kmol)^{-1} \cdot 293 \, K}{\sqrt{2} \cdot 6.022 \cdot 10^{23} mol^1 \cdot 0.43 \cdot 10^{-18} \, m^2 \cdot 10^5 \, Pa} \tag{2.11}$$

$$= 65 \, nm \quad . \tag{2.12}$$

Considering the height h of the gap between ALD head and substrate table to be 200 μm, the Knudsen number can be calculated:

$$Kn = \frac{\lambda}{h} = \frac{65 \, nm}{200 \, um} = 3.2 \cdot 10^{-3} \quad . \tag{2.13}$$

As the Knudsen number is smaller than 0.01, the flow is considered to be a continuum flow[71] and the Navier-Stokes equations with conventional no-slip boundary conditions could be applied. In addition it becomes obvious that bigger dimensions (e.g. the 1 mm wide gas slits) lead to even smaller Knudsen numbers. As the gap between ALD head and substrate table is the smallest dimension in this domain, the flow dynamic could be seen (and simulated) as continuous flow in all parts of the ALD system. If the characteristic length in the range of the the mean free path, Knudsen flow must be considered (also called *slipflow* regime), which is the transition regime to molecular flow. At atmospheric pressure this is in the range of 50-100 nm, but low pressure ALD would enlarge the Knudsen number towards the molecular kind of flow. Beyond Kn = 0.1, alternative simulation techniques (e.g. Monte Carlo simulations) must be considered.[71] All in all, the use at atmospheric pressure provides for the gas kinetics at all points throughout the simplified domain a laminar (continuous) viscous gas flow.

Furthermore, it is notable that convection is not able to transport the precursor molecules or their carrier gas directly onto the solid surfaces, especially to their reacting counterparts on the substrate. The streamlines never come in contact with surfaces which is why the convective surface flux is zero, so to say: Convection does not lead to any kind of deposition.[72] In contrast, diffusion does enable the mass transport onto surfaces an enables the ALD growth as described in the following. The tangential velocity of the viscous flow is always zero at the boundary or at least equal to the respective wall velocity (in case of a static wall = 0). The gas is brought to rest by the shear stress τ at the boundary. Orthogonal to that boundary, the velocity increases up to the maximum value in the main stream of the flow. The distance between the boundary and the maximum value is called the thickness of the boundary layer δ. This profile of the boundary layer of a 2-D surface and in a 2-D pipe is depicted in Figure 2.5.
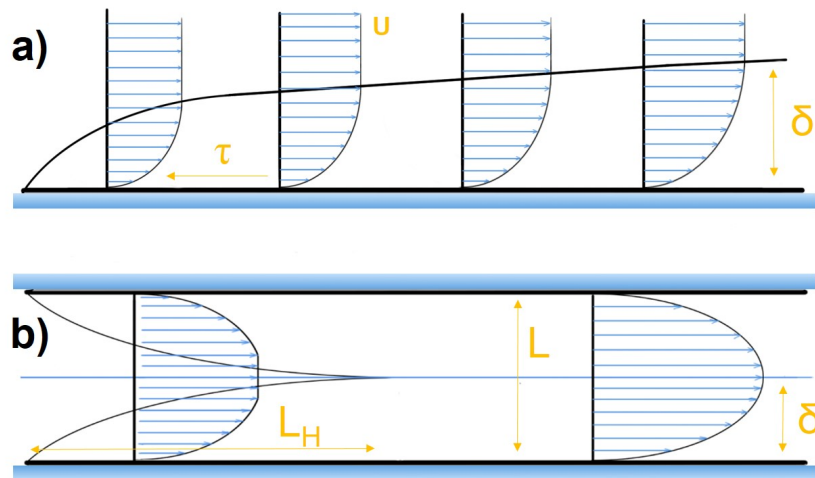
Figure 2.5.: Formation of the boundary layer (with the thickness δ) of viscous flow over a static wall (a) and in a 2-D pipe with the height L (b). The velocity profiles are depicted with blue arrows. τ represents the shear stress at the boundary, L_H defines the end of the hydrodynamic entrance region.

In case of the 2-D pipe which represents the gas conditions in the spatial ALD assembly, both boundary layers (formed by the shear stress at the bottom and the top of the assembly) merge at the end of the so-called *hydrodynamic entrance region* at the distance L_H.[73] At this point, the flow is fully developed and the boundary layer thickness is equal to the half of the channel height. The mass transport (e.g. of precursor molecules) through those boundary layers is always driven by diffusion. The latter is based on Fick's law as introduced for the permeation mechanisms in the following (subsection 2.2.1).

2.2 Gas diffusion barriers

Gas diffusion barriers (GDBs) currently play a decisive role for opto- and microelectronic devices. With the continuous miniaturization of electronic devices, the containing components get smaller and smaller, in the range of several nanometers. In these dimensions, physical effects on the scale of a few nanometers can dominate the functionality. Single molecules (of water or oxygen) can have a big influence on the physical processes in those devices, e.g. water can lead to decomposition mechanisms in perovskite solar cells[74] or harm the organic functional layers inside organic light emitting diodes.[75] Gas diffusion barriers prevent the infiltration of those molecules into the electronic devices, prolonging their lifetimes to 10.000 hours and beyond.[10] Even in the early 90s, the need for those barriers for example for preventing degradation of OLEDs has been reported. Here, barrier layers by glass encapsulation could extend the lifetime dramatically.[8] This glass encapsulation are stuck to the devices with epoxy glue, compare Figure 2.6a. This method was the gold-standard in the early 2000s and even now. With the request for all-in-line processes on flexible substrates, the demand for alternative techniques providing comparable barrier properties comes into account. Al_2O_3, fabricated by reactive sputtering showed very promising barrier properties already in 2008.[76] As ALD was known to lead to dense, amorphous films those sputtering processes were replaced by ALD. The deposition via ALD of comparable thin films leads to WVTRs in the range of 10^{-6} $gm^{-2}d^{-1}$.[77] With the upcoming industrialization of spatial ALD systems those barriers could be deposited in an in-line roll-to-roll process.

In the following, the different encapsulation techniques are discussed in more detail, also illustrated by Figure 2.6. Here, the choice of substrate is of special importance. While glass substrates serve as a sufficient barrier against environmental influences from below, flexible foils as substrates require an additional gas diffusion barrier underneath the device. The top encapsulation can be achieved by a glued glass, as already described, or by the use of an additional gas diffusion barrier (for example deposition via ALD). In the traditional glass encapsulation, additional getter material (e.g. calcium) also could absorb chemically H_2O diffusing through the epoxy glue.[13,77,79] Here, an ALD coating directly on the device could exclude the permeation of moisture through the epoxy glue, but requires (in most instances) moderate process temperature of $\leq 100°C$. If both of the above-mentioned top encapsulation possibilities on the device are not possible e.g. due to temperature limitations and the need of a flexible encapsulation, it is also possible to adhere an additional foil, which is already coated with a gas diffusion barrier, to the component (see Figure 2.6 d).
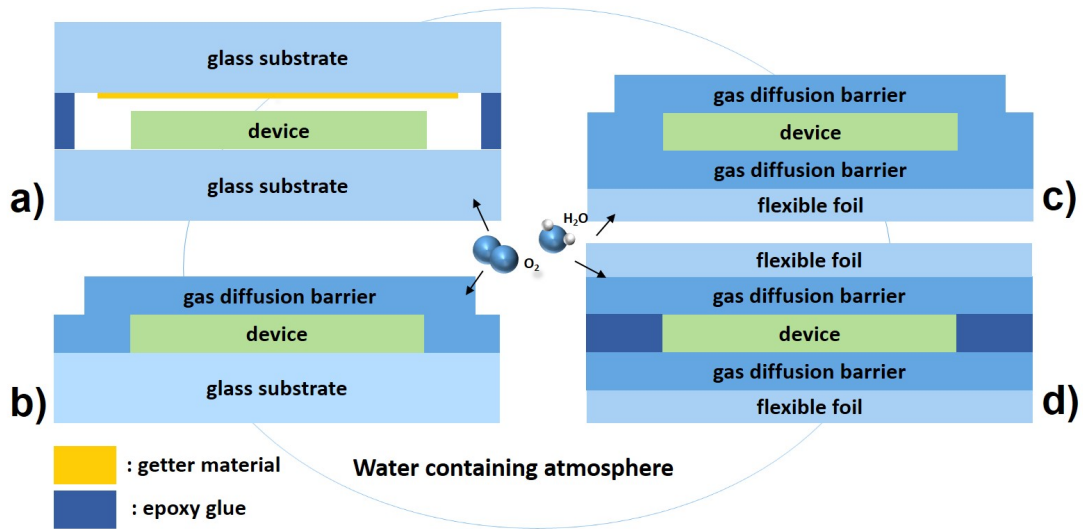
Figure 2.6.: Methods of encapsulation in thin film electronics on glass (a,b) and on flexible foils (c,d). The device (e.g. a perovskite solar cell or an organic light emitting diode) could be encapsulated with a glass which is glued on the substrate underneath or with an encapsulating deposition technique like ALD or PVD. Alternatively, a flexible barrier foil could be glued on top of the device. For all foil-based substrates a barrier layer underneath the device has be provided. Inspired by.[78]

Note that all top encapsulation layers could be glued with edge sealing or in a full area glue avoiding additional getter material. All in all, the encapsulation technique is strongly dependent on the physical demands of the device and on the requirements of the final product. Nowadays, different techniques are employed in the industry to provide stable roll-to-roll optoelectronics, e.g. the cold or hot lamination of barrier foils by pressure sensitive adhesives.[80]

2.2.1 Permeation

In the following, the physical process of permeation is described in detail as the need for gas diffusion barriers is strongly linked to its nature. In addition, understanding the different permeation mechanisms helps to improve the encapsulation methods. Here, permeation describes the physical process of the mass transport of a gas or a liquid through a solid. This process can be basically separated into three steps: The adsorption of the permeate at the surface of the solid, the diffusion of the permeating molecule through the solid in a random-walk and the desorption of the permeate from the solid surface into the gas phase. The process of the diffusion of the permeate at a given concentration $c(x,t)$ and a given diffusion coefficient D is called the (one-dimensional) flux

J_x. Generally, the concentration $c(x,t)$ is strongly dependent on its place x and the time t. The overall flux can be described by Fick's first law:[72]

$$
\begin{aligned}
J_x &= -D\frac{\partial c(x,t)}{\partial x} & (2.14)\\
&= -D\frac{c_1(t) - c_2(t)}{d} & (2.15)\\
&= \frac{\Delta N}{\Delta t} \cdot \frac{1}{\Delta A} & (2.16)
\end{aligned}
$$

Here, the partial fraction could be replaced by the difference in concentration at the bottom and the top of the thin film, divided by its total thickness (in the x-direction) d. Note that only the perpendicular concentration gradient is taken into account. In addition, the particle current density J_x depicts the amount of substance ΔN diffusing in a certain time Δt through a given area ΔA.[81] Furthermore, the concentration c could be described as[81]

$$
c = p \cdot S(c,p). \qquad (2.17)
$$

Here, p represents the partial pressure of the adsorbed gas over the surface A. S is the sorption coefficient of the gas, which can either adsorb physically on the surface by dipole-dipole-bonds (i.e weak van-der-Waals forces) or by covalent or even ionic bonds. As a result of the different nature of the bonding, it could be devided into *physisorption* (= physical adsorption) and *chemisorption* (= chemical adsorption).[82] However, the sorption coefficient $S(c,p)$ could be described in different models, assuming different dependencies.[83] $S(c,p) = S$ for example is called Henry's law and assumes a constant sorption coefficient, mostly applicable for low partial pressures and low concentrations of adsorbed gases at a wide surface.[84] Henry's law considers the physical situation where there is no competition for adsorption sites an adsorbed molecules nor adsorbed molecules could interact.[85] Another mode is called the langmuir sorption model, which considers monolayer adsorption with a limited space on the surface. Here, the sorption coefficient is strongly dependent on the partial pressure of the permeate at the surface.[85] Comparable langmuir models take place in terms of the surface coverage of ALD growth. For further details see subsection 2.1.1. Taking this sorption theory into account the flux could be described as:

$$
J_x = -D \cdot \frac{p_1(t) \cdot S_1(c,p_1) - p_2(t) \cdot S_2(c,p_2)}{d}. \qquad (2.18)
$$

Considering Henry's law (i.e. $S_1 = S_2$) and the permeability $P = D \cdot S$, the flux could be written as:

$$J_x = -P \cdot \frac{p_1 - p_2}{d}. \tag{2.19}$$

For most barriers, the diffusion coefficient but also the permeability could be seen as constant within the material. As of that, the permeation in the steady-state mode (with c independent of x and t) can be assumed to be inverse proportional to the diffusion path inside the material e.g. to the layer thickness. In the following, for all barriers it has to be separated between the ideal diffusion (described by Fick) or the diffusion through the defects. For example, the permeation through a glass encapsulation can be described by Fick's diffusion law as described above.[86] The permeation through metal oxide based thin films often provides higher permeation rates as expected from the Fickian model (based on bulk material) as these layers contain many defects promoting the overall diffusion of gases through this encapsulations.[86] Further details will be discussed in subsection 2.2.5.

2.2.2 Temperature-dependent permeation

In general, the diffusion of gas molecules through a solid can be considered as a temperature activated process[87][88][89].[90] The permeation can be described with the Arrhenius equation:

$$P(T) = P_0 \cdot exp\left(-\frac{E_A}{k_B T}\right) \qquad . \tag{2.20}$$

k_B is the Boltzmann constant and P_0 could be understood as proportionality factor. E_A is called the activation energy, given in kJ/mol, strongly dependent on the film properties and those of the permeate. This exponential behavior dominates the small temperature ranges, assuming otherwise unchanged film properties in the temperature regime. For example, for polymers but also metal oxides (which react with moisture at higher temperatures), the structure is not constant at elevated temperatures.[84] In addition, the concentration of gas molecules on the surface can change with increasing temperature, leading to a deviation from the Arrhenius-like behavior in Equation 2.20.

2.2.3 Time-dependent permeation

In the following, the time dependent permeation for ideal barriers is depicted, based on Fick's law. Taken the continuous equation leads to chronological change of concentration:[91]

$$\frac{\partial c}{\partial t} + \frac{J_x}{\partial x} = 0 \tag{2.21}$$

$$\frac{\partial c}{\partial t} = D\frac{\partial^2 c}{\partial x^2} \tag{2.22}$$

Note that in this case, only the x-direction with a diffusion coefficient not dependent on concentration and place is taken into account. To solve this (second order) differential equation, the expression has to be integrated over time.[92] For more information about the solution of those differential equations see Ref.[93,94] However, the time and space-dependent concentration is given by[93]

$$c(x,t) = c_1\left(1 - \frac{x}{d}\right) - \frac{2c_1}{\pi}\sum_{n=1}^{\infty}\frac{1}{n}\left(\frac{n\pi x}{d}\right)exp\left(\frac{-Dn^2\pi^2 t}{d^2}\right), \tag{2.23}$$

where c_1 is the concentration on the upstream side of the layer (with thickness d). The concentration of the permeate at the downstream position is set to zero. To calculate the overall amount of permeated substance, the flux J_x has to be integrated (compare Equation 2.16). For the time-dependent permeated amount of substance N could be applied:

$$N(t) = \frac{Dtc_1}{d} - \frac{dc_1}{6} - \frac{2dc_1}{\pi^2}\sum_{n=1}^{\infty}\frac{(-1)^n}{n^2}\exp\left(-\frac{D\pi^2 n^2 t}{d^2}\right). \tag{2.24}$$

For an equilibrium state ($t > t_{lag}$) this expression can be simplified to:

$$N(t \to \infty) = \frac{Dc_1}{d}\left(t - \frac{d^2}{6D}\right). \tag{2.25}$$

This solution represents a linear increase of the amount of permeated particles after a certain time, called lag-time t_{lag}, which is the time, the system needs to form the stationary steady-state. This dependency is demonstrated in Figure 2.7. Obviously, the lag-time $t_{lag} = d^2(6D)^{-1}$ is directly proportional to the barrier thickness d as well as to the inverse of the diffusion coefficient D. Knowing the lag-time, the diffusion coefficient could be estimated.
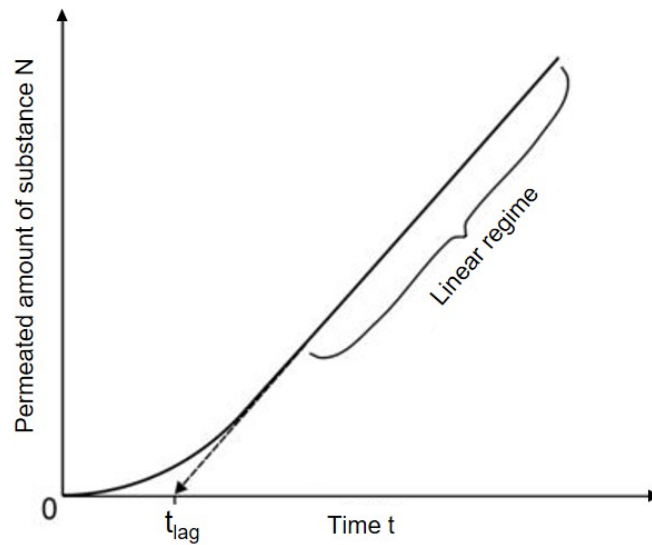
Figure 2.7.: Illustration of the time-dependent permeation. A thin film is exposed to a constant concentration c at $t = 0$. The permeate diffuses through the sample until the steady-state mode is occured, leading to a linear increase of diffused particles over time. Inspired by.[87]

Note that in practice for multilayer structures (e.g. the diffusion of water through a PET/Ca stack), the actual (apparent) lag-time can exceed the lag-time based on Fick's law due to the initial diffusion of the permeate through the structure above or underneath the test barrier.

2.2.4 Definition: Water vapor transmission rate

In practice, two different figures of merit for the diffusion properties of barrier layers and their the characterization have been established. These include the $WVTR$ (water vapor transmission rate) and the OTR (oxygen transmission rate), i.e. the amount of water and oxygen molecules to diffuse through a certain (barrier) layer (per time and per area). For the WVTR the following equation applies:[95]

$$WVTR = M_{H_2O} \cdot J_{(t \to \infty)} \quad .$$ (2.26)

Here, $J_{(t \to \infty)}$ represents the flux in the steady state mode. As the most of the barrier layers are evaluated by calcium tests, the diffusion of water molecules towards calcium sensors will be investigated in the following. Taken the expression for the flux into

account (compare Equation 2.16), the expression of the $WVTR$ can be simplified to:

$$WVTR \quad = \quad M_{\mathrm{H_2O}} \cdot \frac{\Delta N}{\Delta t} \cdot \frac{1}{\Delta A} \tag{2.27}$$

$$= \quad \frac{M_{\mathrm{H_2O}}}{M_{\mathrm{Ca(OH)_2}}} \cdot \frac{\Delta m}{\Delta V \Delta t} \cdot \Delta d \quad . \tag{2.28}$$

Here, the reaction Substituting the density $\rho = \Delta m / \Delta V$ and $\Delta d = \Delta d_{\mathrm{Ca(OH)_2}}$ leads to:

$$WVTR = 2 \cdot \frac{M_{\mathrm{H_2O}}}{M_{\mathrm{Ca(OH)_2}}} \cdot \rho_{\mathrm{Ca(OH)_2}} \cdot \frac{\Delta d_{\mathrm{Ca(OH)_2}}}{\Delta t} \quad . \tag{2.29}$$

The factor '2' comes into account as a reason for the amount of water molecules leading to oxidation of one calcium atom, assuming the simple equation

$$\mathrm{Ca} + 2\,\mathrm{H_2O(g)} \longrightarrow \mathrm{Ca(OH)_2} + \mathrm{H_2(g)}.$$
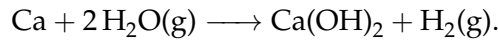
This reaction is reported as most dominant for the oxidation of calcium.[84,96,97] In addition Carcia et al. reported just a 3% difference in WVTR, assuming the reaction to calcium oxide[97]

$$\mathrm{Ca} + \mathrm{H_2O(g)} \longrightarrow \mathrm{CaO} + \mathrm{H_2(g)}.$$
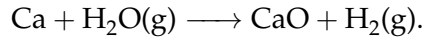
With the molar masses of water ($M_{\mathrm{H_2O}} = 18.02\,\mathrm{gmol^{-1}}$) and calcium hydroxide ($M_{\mathrm{Ca(OH)_2}}$ $= 74.09\,\mathrm{gmol^{-1}}$), and a fixed calcium density, the amount of corroded calcium and therefore the required amount of water for the corrosion process can be determined. As the WVTR specifies the amount of water, diffusing through a certain area of the barrier in a certain time, its unit is commonly given by $\mathrm{gm^{-2}d^{-1}}$. For multilayers the permeation rate through the entire stack could be calculated by the summation of the reciprocal of the permeation rates of every single film ($WVTR_n$) included:[93]

$$\frac{1}{WVTR_{tot}} = \frac{1}{WVTR_1} + \frac{1}{WVTR_2} + .. + \frac{1}{WVTR_n} \quad . \tag{2.30}$$

Obviously, the total water vapour transmission rate is dominated by those films which show superior intrinsic barrier properties while the permeation through inferior barriers like polymer foils (due to the reciprocal character) gets negligible. The same behavior also applies for the diffusion coefficient. Here, also the respective coefficient of each single layer could summed up reciprocally.[98] Further details on the WVTR are discussed in section 3.5, presenting the optical Ca test and its mode of operation.

2.2.5 Permeation through defects

In the field of thin film gas diffusion barriers, the deposited layers (e.g. metal oxides) always include defects, such as pinholes. Besides the intrinsic water diffusion through the ideal barrier (as described above), gas diffusion through these defects takes place. In literature, it is well known that the overall water vapor transmission rates are dominated by this defect-related diffusion, which typically renders the WVTR to be much larger than the intrinsic WVTR of the ideal defect-free material.[86,99–101] The defects which are promoting the diffusion are a result of dust particles on the substrate or residuals embedded during the fabrication process. Furthermore thin films can form growth defects during their deposition shown in Figure 2.8. Those defects can be basically classified into lattice defects, nano-defects and macro-defects.[100]
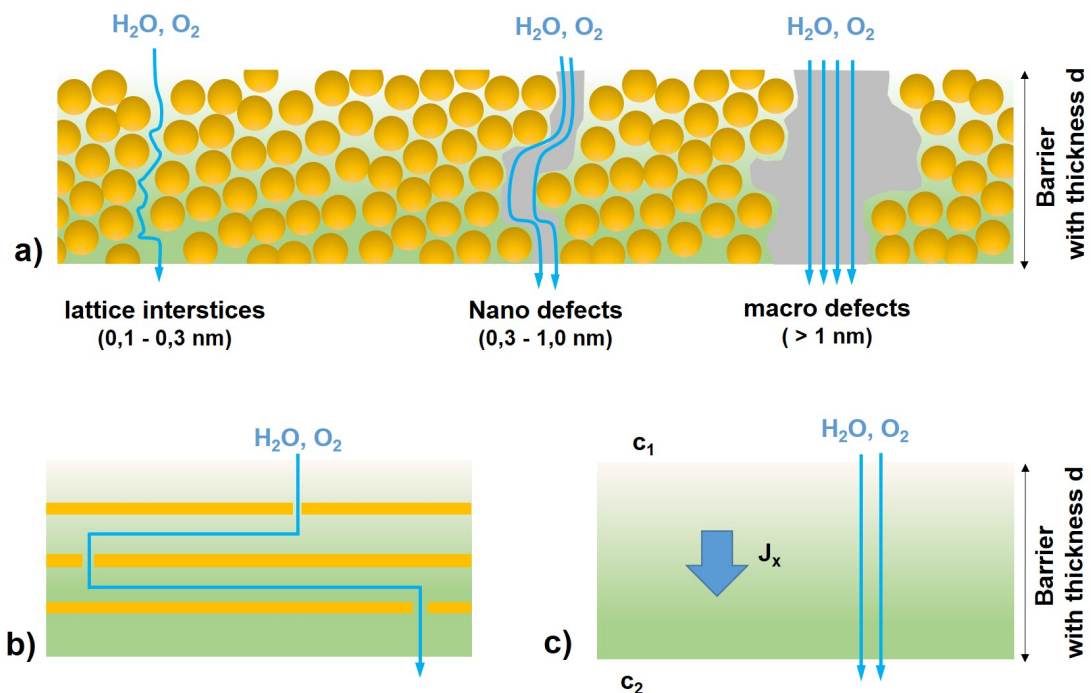
Figure 2.8.: (a) Oxford classification of the mechanism of permeation in thin films: lattice interstices, Permeation through nano and macro defects. (b) principle of multilayer encapsulation: Enlargement of the diffusion paths for water and oxygen molecules (c) Scheme of the permeation through an ideal barrier with thickness d. Adapted from[100].[78]

In this classification, macro-defects are those defects where no interaction between gas molecules and the barrier material takes place. The macro-defect is typically three to four times larger than a typical permeate molecule (0.2 – 0.3 nm).[100] In this case, e.g.

water molecules diffuse unimpeded through the barrier. The respective activation energy for this kind of diffusion is the same order as the diffusion through a bare substrate without barrier.[84] Defects in the size of 0.1 - 0.3 nm are referred to the interstices in the (amorphous) grain boundaries. As both water and oxygen molecules are too large to pass these interstices, the activation energy for this kind of diffusion is very high and its contribution to an overall integral diffusion is negligible.[84,86] The common understanding is that the dominant part in diffusion is the permeation through nano-defects,[100] as the number of defects in a typical thin oxide barrier layer is up to four orders of magnitude higher than the number of the bigger macro-defects.[102] In addition, a chemical interaction of water vapor and the material itself (e.g. at a nano-defect) can lead to an enhanced diffusion at this defect.[86] Due to this model of permeation through defect states, multilayer encapsulation are proposed.[13,98,103] Here two different layers with different defect densities are stacked on top of each other. This bilayer is also called a dyad. Often, a multilayer encapsulation is based on a pair of one inorganic barrier layer and one polymer top coating.[86] Multilayer encapsulation provides several advantages: Tortuous diffusion paths by different defects densities (as depicted schematically in Figure 2.8b), mechanical and chemical protection of the barrier underneath (e.g. the inorganic barrier layer) or the improvement of mechanical flexibility in terms of flexible GDBs.[104] For more information about multilayer encapsulation see ref.[86]

2.3 Solar cells

The energy conversion in solar cells is based on the creation of electron-hole pairs in the active material, which is typically a semiconductor. Semiconductors are characterized by their forbidden band gap between valence band (VB) and conduction band (CB). In this gap, there are no energy levels that can be occupied by electrons. Nevertheless, electrical conductivity by carrier generation can take place when an electron is excited from the valence into the conduction band. This excitation can be empowered by heat or, in the case of solar cells, by photons. The photon transfers its energy to an electron in the valence band, exciting it to the conduction band. The respective generated electrons and electron holes travel through the cell until they reach an electrode or recombine. As the number of generated electron-hole pairs are directly proportional to the number of photons exciting the respective electrons, i.e. the amount of incoming light, the resulting current is directly proportional to the light absorbed in the semiconductor. The light absorption in the band gap is dominated by its design, e.g. the electrical and structural properties of the active material.[105]

2.3.1 Perovskite solar cells

Originally, perovskites are minerals of calcium titanium oxide ($CaTiO_3$), named after Lev Perovski (1792–1856), a Russian mineralogist. In the late 1990s, materials with perovskite structure (i.e materials which crystalize in ABX_3-Structure) became of interest, showing promising optical and magnetic properties.[106,107] First reports on solar cells based on perovskite materials are from 2009, reporting solar cell efficiencies around 3.8%,[108] but even 6.5% in 2011.[109] Models even predict the efficiency limit of perovskite cells to 31%, reasoned by the Shockley-Queisser limit, which is known to be the upper limit for the efficiency of not-focused sunlight[110] and strongly dependent on the respective (perovskite) band gap. Actually, in 2013 the perovskite solar cell technology was selected as one of the biggest scientific breakthroughs by the editors of Science and Nature.[111] In 2017 perovskite solar cells (PSCs) are able to achieve efficiencies above 20% (22.1-22.7%[26,28]), competing with conventional silicon-based solar cells. In addition to these high PCEs reported, perovskite solar cells combine many of the advantages of organic solar cells or dye-sensitized solar cells compared to silicon based solar cells. As such, perovskite solar cells offer low material costs, low fabrication temperatures and the possibility for the deposition on flexible roll-to-roll compatible substrates.
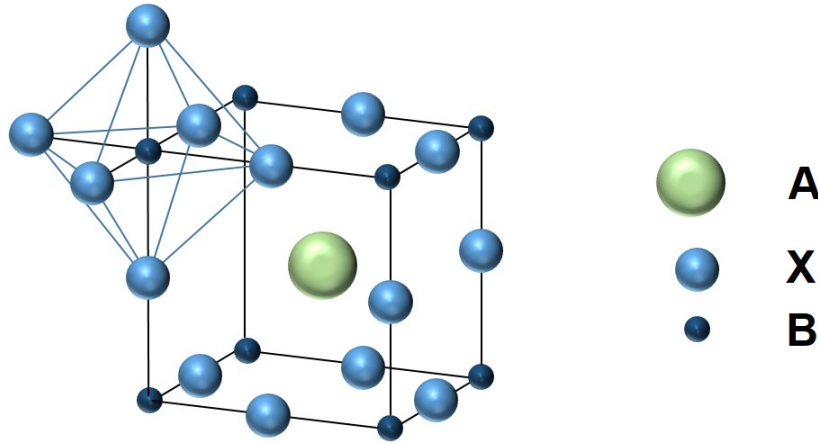
Figure 2.9.: ABX$_3$ perovskite structure: In the BX$_6$ octahedral structure the cubo-octahedral site is occupied by the larger A cation. Adapted from Ref.[111]

An conventional perovskite crystal structure is formed by an ABX$_3$-structure, where B represents the cation from a metal e.g lead (Pb) and X is the respective anion, see Figure 2.9. In the BX$_6$ octahedra B is located at the center of the octahedra and X lies in the corner, typically consisting of halides like chlorine, bromine or iodine. The BX$_6$ octahedra form an extended three-dimensional lattice all-corner-connected type.

For the use of perovskites in photovoltaics, CH$_3$NH$_3$PbI$_3$ is the most common one.[106,112] In those solar cells, the methyl ammonium ion (CH$_3$NH$_3$) is used as the organic part of the perovskite. In contrast to e.g. organic semiconductors, perovskites form a homogeneous lattice which enables carrier transport. The band gap of e.g. CH$_3$NH$_3$PbI$_3$ can be determined to be 1.55 eV.[113]

2.3.2 Solar cell characteristics

Generally, the Shockley diode equation is used to describe the electronic behavior of a diode,[114] i.e. the dependency of the current on the voltage utilized. In principle, the solar cell functions as a diode including an additional photo current J_{ph} caused by the light absorption. In addition, a series (R_s) and a parallel (R_p) resistance account for parasitic effects in a realistic device. Thus, the current density through the solar cell J (in the area A) can be written as:[115]

$$J = \frac{1}{1 + R_s/R_p} \left(J_S \left(exp \left(\frac{V - JR_sA}{n_{pn}k_BT/e} \right) - 1 \right) - \left(I_{Ph} - \frac{V}{R_pA} \right) \right) \qquad . \qquad (2.31)$$

Here, J_S represents the reverse (bias) dark saturation current density, while V is the voltage across the solar cell. n_{pn} depicts the ideality factor describing the deviation from an ideal diode. The ideal JV curve of a non-illuminated and an illuminated solar cell as well as the characteristic parameters are shown in Figure 2.10. As depicted, a characteristic curve of the non-illuminated solar cell equals that of a simple p-n-junction. In forward direction after the depletion zone becomes thin enough that the built-in electric field cannot counteract charge carrier motion across the p–n junction, resulting in a substantial electric current. In reverse direction, the barrier potential between the p side and the n side is increased. Here, a very little current will flow, also called the reverse leakage current, until the diode break down.

The characteristic curve of a solar cell differs from the one of a normal p-n-junction in the additional photo current density J_{ph} when the solar cell is illuminated. This illumination leads to an current offset in the Shockley equation, depicted in Figure 2.10. Obviously the maximum power achieved in a solar cell is the product of the current density J and the voltage V. As of this, maximizing the power output equals maximizing the area confined in the third quadrant by the Shockley equation.
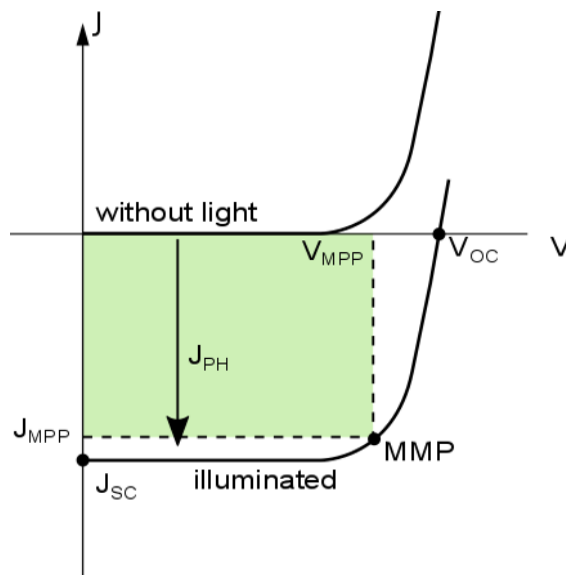
Figure 2.10.: Depicted is the characteristic JV-Curve of an illuminated solar cell. The maximum power $P = - J \cdot V$ is defined by the area stretched underneath the curve. The intersections with x- and y-axis represent the short circuit current density J_{SC} and the open circuit voltage V_{OC}.

To evaluate the solar cell characteristics, the short circuit current density J_{SC} and the open circuit voltage V_{OC} are denoted. The short circuit current is the current density through the solar cell when the voltage across the solar cell is equal to zero (i.e., $V = 0$,

when the solar cell is short circuited). Analogously, the open circuit voltage represents the difference in electrical potential when the solar cell is disconnected i.e. connected as an open circuit ($J = 0$). Furthermore, the decive fill factor (FF) is a measurement of the solar cell design quality, as the voltage and current density at the device maximum power is taken into account:[84]

$$FF = \frac{J_{MMP} \cdot V_{MMP}}{V_{OC} \cdot J_{SC}} \qquad . \tag{2.32}$$

The fill factor describes the interplay of the effects introduced by device resistances (i.e. R_s and R_p), associated with underlying physical processes in the device.[116] Most importantly, the power conversion efficiency (PCE) of the solar cell is defined as the ratio of the extracted power at the maximum power point (MMP) and the incoming light power P_{in}:

$$PCE = \frac{P_{out}}{P_{in}} = \frac{J_{MMP} \cdot V_{MMP}}{P_{in}} = \frac{FF \cdot J_{SC} \cdot V_{OC}}{P_{in}} \qquad . \tag{2.33}$$

3

Atomic layer deposition systems and barrier characterization methods

In the following, the home-built batch and spatial atmospheric pressure ALD systems will be described and compared to other spatial ALD concepts. In addition, different versions of the dielectric barrier discharge (DBD) plasma source and their ozone generation are introduced. Furthermore, since the reports on the optical Ca test are still limited, its measuring principle determining the amount of water permeating through a gas diffusion barrier is introduced. At the end, the measuring principle of RBS and NRA is explained in short.

3.1 State of the Art: Atmospheric pressure spatial ALD systems

Spatial ALD was first reported in 2008 by Levy at al.[18,19] Since then, the annual number of reports on spatial ALD has been continuously increasing. Linked with this fact, there were several different concepts, realizing a spatially separated ALD.[117] Most of the spatial ALD setups were used for the deposition of metal oxides in thin film transistors (TFTs),[18,118,119] but SALD is also used in the field of photovoltaics, mostly for solar cell passivation,[120–122] and as a deposition tool for charge extraction layers[123,124]

and barrier layers[125] in solar cells. The (original) design by Levy et al. is based on an
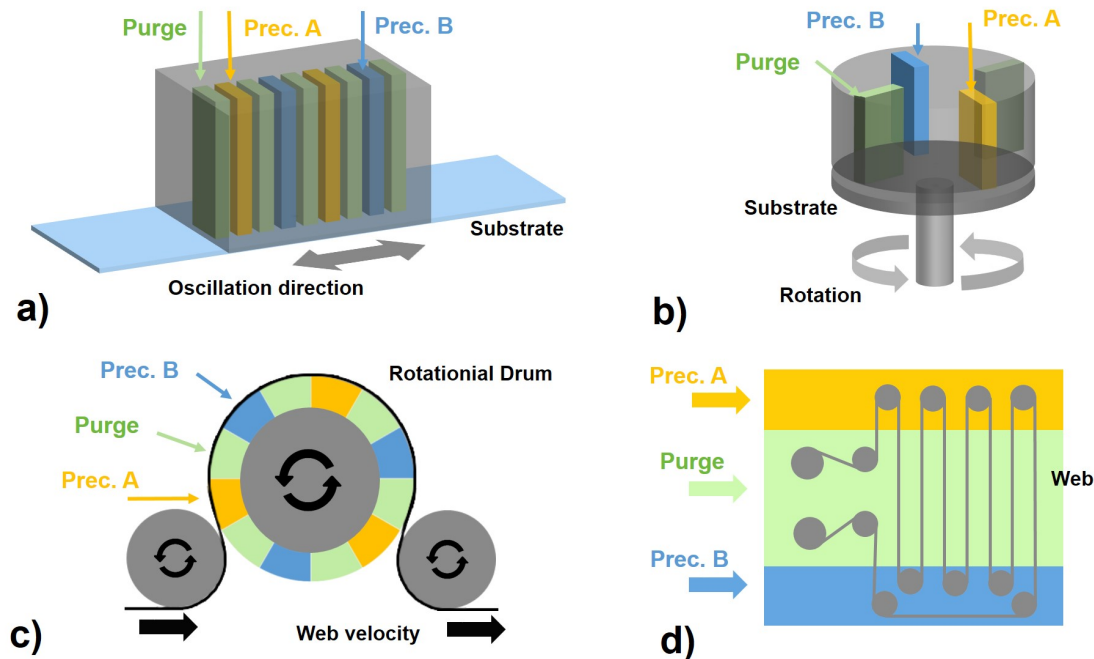
Figure 3.1.: Concepts of spatial ALD: While Levy at al. introduced spatial ALD with a oscial-
liting substrate under a fixed ALD head,[18] other groups expands this concept to
contrary spinning roles,[126][21] or even roll-to-roll processes with bigger precursor
gas regimes in a serpentine chamber presented by Dickey at al.[127,128]

oscillating substrate underneath a fixed ALD head (depicted in Figure 3.1a), also called
an in-line (SALD) process. Basically, this setup is sheet-to-sheet, and also roll-to-roll
compatible, enabling the thin film deposition on single rigid substrates or flexible foils.
Their alternate precursor A-B scheme is interrupted by an inert gas purge, respectively.
The original setup is working at 177°C and in a relative small coating area (width =
50 mm).[18] Another concept provides the roll-to-roll deposition, (e.g. Poodt et al.,[126][21])
using spinning circular substrates, partially even with a ALD precursor delivery sys-
tem rotating in an opposite direction, compare Figure 3.1b and Figure 3.1c. The latter
concepts take advantage from the continuous deposition process avoiding acceleration
and braking times, but suffers from the limited choice of substrates. Another roll-to-roll
concept is presented by *Lotus Applied Technology* (USA), see Figure 3.1d. Here, a roll-
to-roll serpentine configuration is placed inside a chamber, which is divided into three
parts: The precursor A zone and the precursor B zone are separated by the purge zone.
This concept enables several coating steps in the same precursor zone, but is based on
large volumes and high amounts of precursors, which require especially at atmospheric
pressure high amounts of purge gas to afford ALD characteristics. Similar concepts are

taken into account in the topic of powder ALD coating,[129,130] where the powder is transported on a fluidized bed through the different (large scale) gas regimes.[131] In principle, in sharp contrast to the design of Levy et al., the rotary design as well as the roll-to-roll design could work at low pressure (typically 1 mbar) as well as atmospheric pressure. For low pressure-based spatial ALD, a closed reactor zone is required, which even could be realized for roll-to-roll deposition by special floodgate techniques.

In addition, the use of plasma as oxidizing but also as reducing agent (e.g. with a H_2 plasma[132]) can also be realized in spatial ALD setups.[132,133] Parallel to those developments in spatial ALD, several batch ALD processes in a flow-tube reactor at atmospheric pressure have been presented.[134–136] As those concepts resemble the setups of conventional low pressure ALD, they will not addressed in more detail, here. Basically, those concepts provide the insight that ALD at atmospheric pressure could be realized, but also needs special adaption of process parameters. Here, Mousa et al. for example found similar film properties in aluminum oxide films deposited at atmospheric pressure compared to their low pressure analogues, but put special emphasis on the amount of purge gas needed to reduce the physisorbed water that remains on the oxide surface after the water precursor pulse.[137]

In general, a variety of material systems could be realized in spatial ALD. The most common one is Al_2O_3,[20,53,122,125,138–142] but among others, ZnO,[18,123,124,143,144] SiO_2,[133,145] TiO_2,[146–148] ZrO_2[149] or even Ag thin films were also deposited by SALD.[132] Thereby, the substrate velocities used to deposit the thin films vary between 1 mm/s and few hundred mm/s (or up to 100-600 rpm in a rotary setup[20,150]) which results in deposition rates of 1.2 nm/s.[20] Note that the overall growth rate per minute strongly depends on the precursor supply. As most of the setups shown above are just for scientific research, their design is probably not pushed to its limits of fabrication speed.

3.2 Atmospheric pressure plasma batch ALD system

The so-called batch-based ALD system is determined by an inline batch ALD setup with a clear conventional inlet-reactor-outlet structure. A photographic image as well as a schematic of the of the related home-built ALD reactor (with a volume of approx. 100 cm^3) used for the deposition of the Al_2O_3 thin films is shown in Figure 3.2a and in Figure 3.2b. As the ALD setup works at atmospheric pressure as well as with an Ar/O_2 plasma as oxidant, the term APP ALD (*atmospheric pressure plasma* ALD) is used to specify the process parameters. Four separate pipes are used to introduce the working gas into the reactor, controlled via mass flow controllers (MFCs) and separate valves,

respectively. Afterwards, the four lines merge into a single gas inlet pipe. This gas pipe, where the mixture of gases (e.g. the TMA carrier gas and the O_2) takes place, is heated up slightly below the reactor temperature. The reactor is heated by a temperature controlled heat plate. The substrate temperature is set to 80°C for all experiments. Pure argon with a residual water level of less than 20 ppb is used as purge gas as well as carrier gas for TMA. The gas purity is guaranteed by the use of an external purification systems (*Hydrosorb* by *Spectromol*). The argon flow through the TMA bubbler is kept at 100 sccm with an overall gas flow through the reactor of 2 slm (thus 1900 sccm purge). Note even when there is no TMA pulse, 100 sccm are delivered through the so-called bypass to keep the overall gas flow constant. The Ar/O_2 plasma operates with 2 slm total flow and an oxygen content of 1%. The plasma is ignited 5 s after starting the O_2 gas flow (100 sccm) in order to completely fill the reactor with the Ar/O_2 mixture before plasma ignition, compare Figure 3.2c. Here, a typical ALD cycle is shown, consisting out
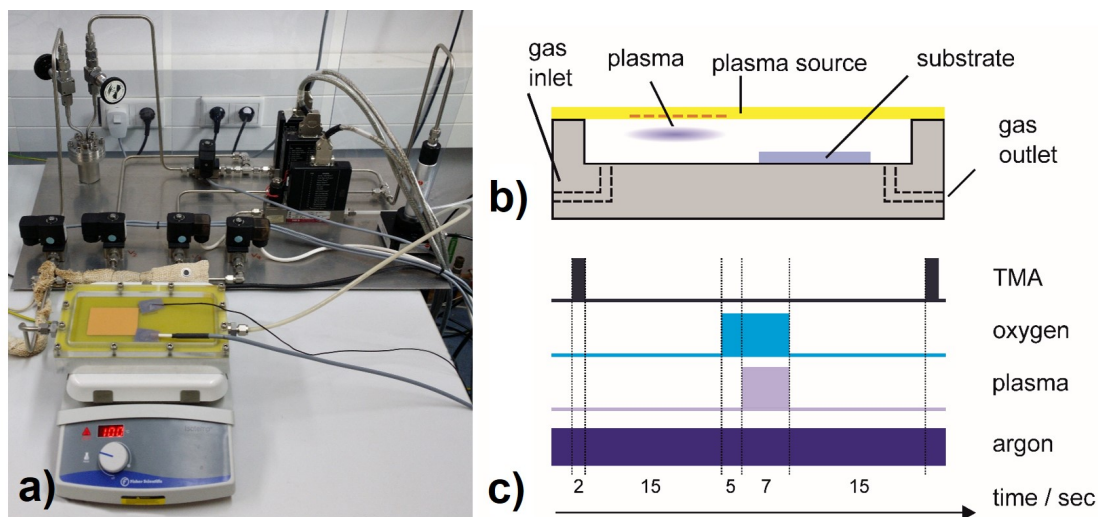
Figure 3.2.: Batch-based APP ALD system: Picture (a) and schematic (b) of the batch-based APP ALD reactor. The setup mirrors the conventional low-pressure ALD setup with a clear inlet-reactor-outlet structure. The substrate position directly below the plasma source is called the direct position. Here, the substrate is displayed in the remote position. (c) Typical ALD cycle times used the deposit Al_2O_2 thin films in the batch-based ALD.

of a 2 s TMA/ 15 s purge/5 s O_2/7 s O_2/plasma/15 s purge sequence. The TMA bubbler was kept at room temperature, since the vapor pressure of TMA is sufficient for ALD deposition (approx. 16 mbar at 20°C[151]). The dependency of the TMA vapor pressure on temperature as well as a schematic of the precursor bubbler used in this work are shown in Figure 3.3. The inlet line purges the amount of N_2 gas inside the bubbler. The gas flux streams above the liquid precursor, leaving the bubbler afterwards through the outline
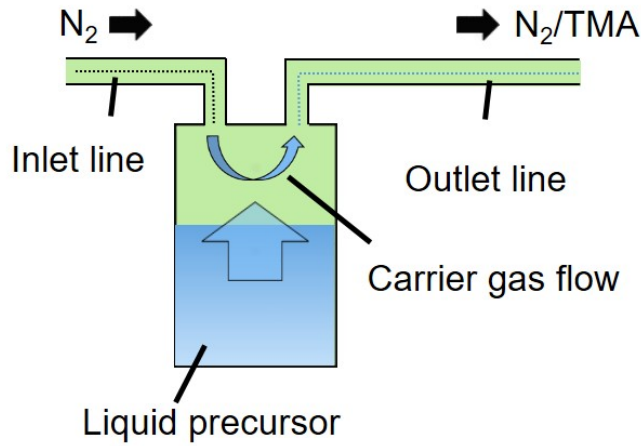
Figure 3.3.: Schematic of the precursor bubbler. Inside the precursor bubbler a liquid precursor (e.g. TMA) is stored. Argon or nitrogen is chosen as carrier gas.

line. The saturation of precursor in the carrier gas takes place strongly depending on the vapor pressure of the respective precursor used (e.g TMA). Assuming a fully precursor saturated N_2 flow, the actual yield of the precursor amount could be calculated via:

$$Y = \frac{vapor\ pressure\ (TMA)}{process\ pressure} = \frac{12\,torr}{760\,torr} = 1.6\% \quad . \tag{3.1}$$

Note that the actual yield could vary depending on the time scale, in which the precursor molecules achieving its vapor phase and could saturate the carrier gas. Therefore 1.6% could be estimated as a maximum yield of precursor. For 100 sccm N_2 through the TMA bubbler, this value corresponds to 1.6 sccm of pure TMA gas.

As second precursor a mixture of Ar/O_2 is used to generate the oxidizing species for the deposition of Al_2O_3 thin films. Therefore a dielectric surface barrier discharge plasma source with two copper electrodes separated by a 0.2 mm thin epoxy-glass fiber (FR-4) is used to generate an Ar/O_2 plasma. The required electric signals for the plasma pulses are generated by a plasma generator and transformed into HV-signals with a transformer. The pulses created by the generator can be controlled by the voltage of the intermediate circuit. Through the inductance of the transformer and the capacity of the cables as well as of the plasma source an oscillating circuit gets stimulated. Further details on the plasma sources are given in section 3.4.

For the ALD process, the substrate position inside the reactor could be divided roughly into two regimes. The direct position is located directly below the plasma source, while the remote position is the one, when the substrate is laterally offset to the right side. This regime is also called the downstream position (see ref.[60]). The plasma ignition was

monitored with a CCD camera. Note that in the case of this batch-based ALD setup the plasma source gets coated during the ALD process. Therefore its ignition characteristics could slightly vary throughout one ALD run, shifting its point of operation. Less voltage can lead to no further ignition after several coating cycles, to high voltages could destroy the thin epoxy-glass fiber thermally.

3.3 Atmospheric pressure spatial ALD system

In principle, the home-built spatial ALD system used in this work is based on the original design by Levy et. al. but expanded by a plasma source, whose design is described in more detail in section 3.4. The system is based on a substrate table oscillating back and forth with respect to the ALD coating head. A schematic as well as a photograph are shown in Figure 3.4. The setup is placed in a glove box which is filled with N_2 ($H_2O < 1\,ppm$, $O_2 < 1\,ppm$). As in the batch-based ALD setup, the gas flows are controlled by external (solenoid) valves combined with mass flow controllers to guarantee fixed precursor and purge flow rates. Precursor bubbler as already described in the batch-based ALD setup are utilized to provide the precursor gas. In the ALD setup, three precursor slots are supplied, divided by purge slots. Once more, a gas outlet is provided between every purge and precursor zone. External heating for the precursor bubbler as well as its pipes (towards the ALD head) is included to avoid precursor condensation inside the pipes. For precursors (like TMA or TDMASn) kept at ambient temperature (i.e. the glove box conditions), no heating is necessary. Especially, in the central precursor slot a plasma source can be mounted. The plasma inlet is made from transparent plexi glas, mounting the plasma source in a remote position roughly 2 cm above the substrate table and enabling the direct visual control of the plasma. Obviously, the ALD head serves as a gas distribution unit and transports the respective gases through its respective slits to the substrate. It could be externally heated up to moderate temperatures (60-80°C) and is composed of three different parts: The upper part, including the gas pipe connection, the middle part, which is basically a spacer, and the lower part, including the gas purge slits and the distribution of the gas outlet. Each slit is 2 mm wide and provides a 20 mm wide regime to the next (5 mm wide) gas exhaust in direction of substrate movement. In contrast, the plasma gas slit is surrounded by a 45 mm wide regime due to the enlarged geometry of the plasma inlet. In total the width of the ALD head is 335 mm. The gas exhausts are located at the outer walls of the ALD head (see black hoses in Figure 3.4a), transporting the process gas out of the reactive zone. The latter is mounted (roughly) 200-300 μm above the substrate table.
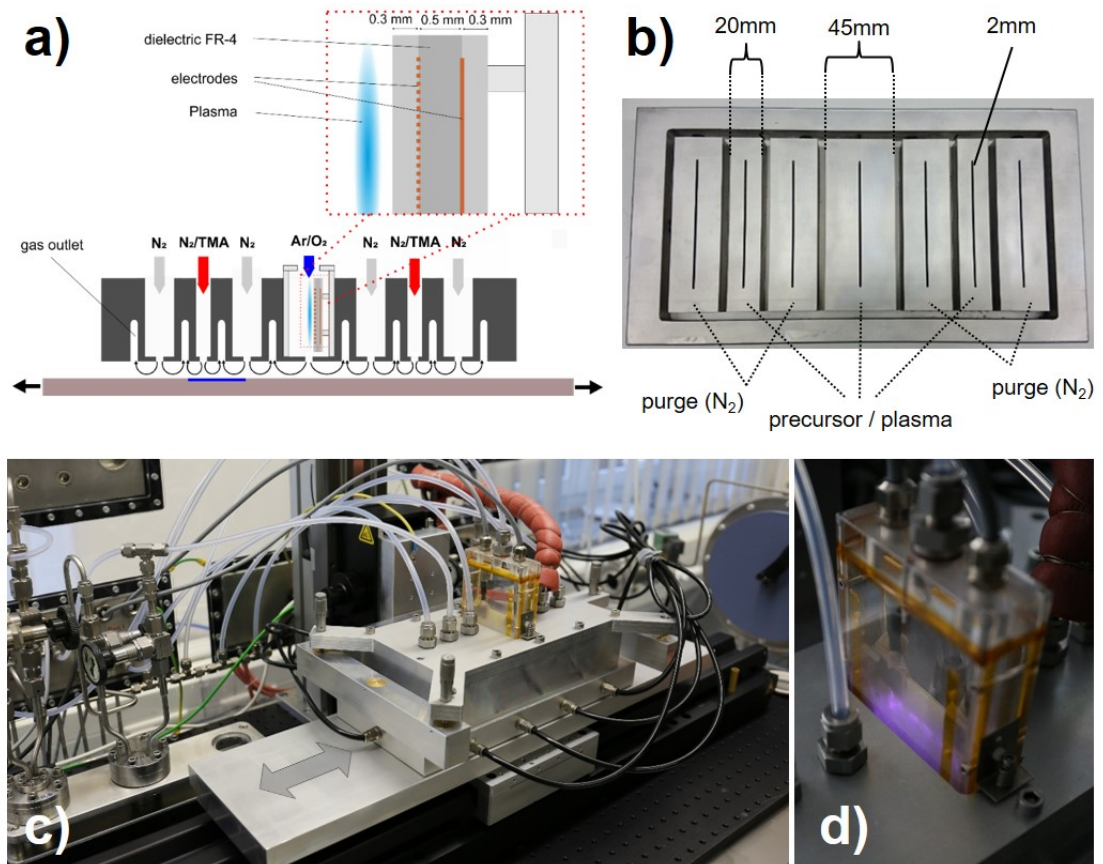
Figure 3.4.: Setup of the home-made spatial ALD. The ALD head is mounted roughly 200-300 μm above the oscillating substrate and and supplies precursor and purges gases alternately. a) Schematic of the spatial APP-ALD with close up of the DBD-plasma source slot. b) Geometry of the lower part which serves as a gas distribution unit showing precursor and purge regimes. The gas outlet is shifted and orthogonal to the flow direction of the streaming gas. c) Photography of the complete system and the Plasma source (d)

Its tilt is aligned with three micrometer screws, while its distance to the substrate is regulated by a fine tuning heavy duty tripod. The substrate is placed in a special substrate holder, which could be heated up to 160 - 170°C and is recessed in the oscillating substrate table, so that the substrate surface is on the same level as the table surface. All working gases (N_2, Ar, O_2) were purified to lower the H_2O concentration to less than 20 ppb to avoid its parasitic chemical reaction with the precursors. In addition all materials made out of plastic (e.g. precursor lines) were pre-baked to evaporate residual water inside the material. The velocity of the substrate table is controlled via PC and could be varied between 1 and 255 mm/s (0.06 to 15 m/min). Before each deposition process, the ALD system is purged with N_2 for at least 2 min followed by 10 s of process-like

precursor delivery without any substrate movement to guarantee an deposition process in steady state (in terms of the surface coverage of the reactor walls etc.).

3.3.1 Simulation of the temperature distribution

Since the setup does not provide external heating of the gas lines, the injected gas temperature may influence the substrate and vice versa. Figure 3.5 shows the evolution of the temperature distribution as a function of the volumentric flow through the gas inlets. The data is based on simulation using *OpenFoam*, solving the differential equations of the mass transport. Further information of the implementation are shown in section A.4 and in ref.[152] Note that the substrate temperature was fixed to 80°C (by a zero gradient boundary condition) and could not be influenced by the injected gas by definition.
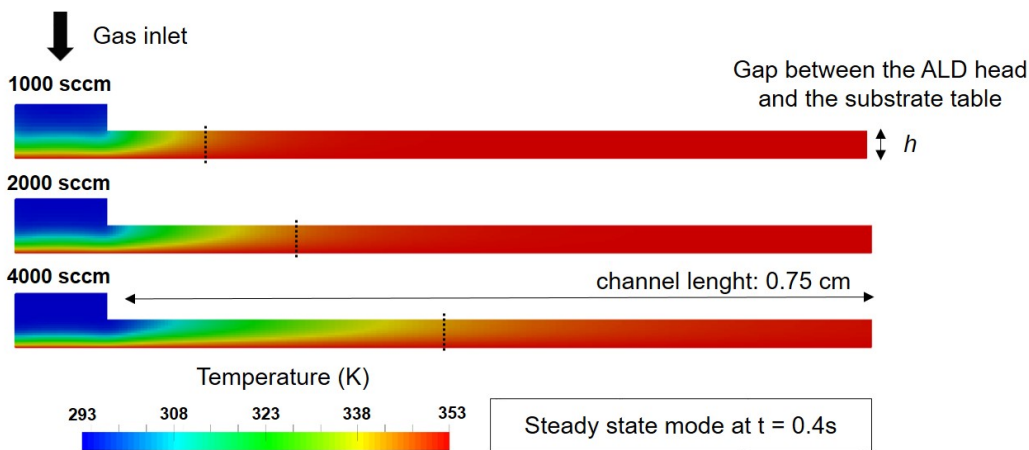
Figure 3.5.: Simulation of the temperature distribution for different purge flow rates. The temperature fields represent the equilibrium temperature distribution. Parameters were set to: substrate velocity v = 30 mm/s, gap height h = 300 μm , substrate temperature = 353 K, temperature of the injected gas = 293 K. Note that the steady state of the temperature distribution is achieved after 0.4 s.

Generally speaking, higher flow rates lead to wider regime of gas colder than the actual process temperature, depicted visually by the dotted lines in Figure 3.5. This situation is less favorable as a homogeneous process is preferred. At high carrier gas flows the nitrogen travels a greater distance before it is heated up to the substrate temperature. For further evaluation, the distance in which the precursor gas reaches 98% of the substrate temperature is calculated, see Figure 3.6. Here, the distance is normalized to the

one centimeter channel length (from one gas inlet to another). It is obvious that the relation between this considered distance and the gas flow rate is linear. Furthermore, even for high flow rates (4000 sccm) the temperature is nearly achieved (98%) in half the distance to the next gas inlet. This is most likely strongly influenced by the small gap between the ALD head and substrate table (300 μm) as the latter is the source of heat in this domain. Note that the ALD head temperature was set to room temperature in the computational simulations.
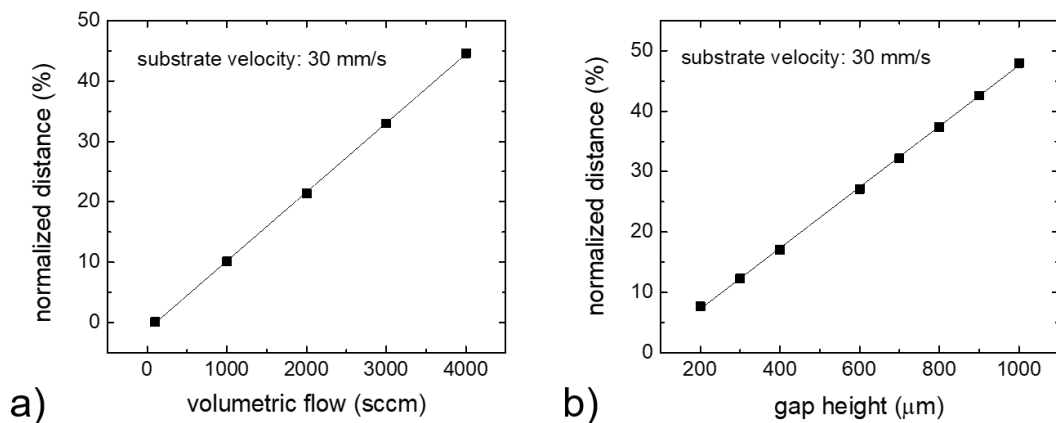
Figure 3.6.: Simulation of the temperature distribution of the carrier gas in dependence of the flow rates (a) (gap height h = 300 μm)and the gap height (flow rate = 1200 sccm (b). Maximum distance in which the carrier gas reaches 98% of the substrate temperature normalized to the channel length. For both cases parameters were set to: Substrate velocity v = 30 mm/s, substrate temperature = 353 K and the temperature of the injected gas = 293 K.

Similar evalution is done for the dependence of the temperature distribution on the gap height. A fixed flow rate of 1200 sccm was chosen, but the gap height varied. The observed normalized distance is linearly proportional to the gap height, but even gap heights of 1 mm result in temperature distribution exhibiting the substrate temperature after 50% of the channel length. All in all, low flow rates and low gap heights are desirable to afford the most homogeneous temperature distribution. Due to these findings, the gap height was adjusted to its minimal possible value (approx. 200-300 μm). For further experiments, it has to be taken into account that the amount of flow gas is strongly linked to a sufficient amount of ALD purge gas. As of that, the choice of the amount of purge gas can be seen as trade-off between a sufficient amount of ALD purge gas to purge all precursor residuals from the surface and a narrow regime of a different gas temperature.

3.3.2 Simulation of the spatial precursor separation

A crucial parameter for the characteristics of ALD growth is the spatial precursor distribution and in particular the precursor separation. Avoiding the cross-talk of the precursors is the prerequisite to avoid parasitic CVD growth and to afford ALD-like layer deposition. To this end, a series of simulations have been conducted in dependence of the substrate velocity, the gap height and the purge gas flow. Factors as precursor con-
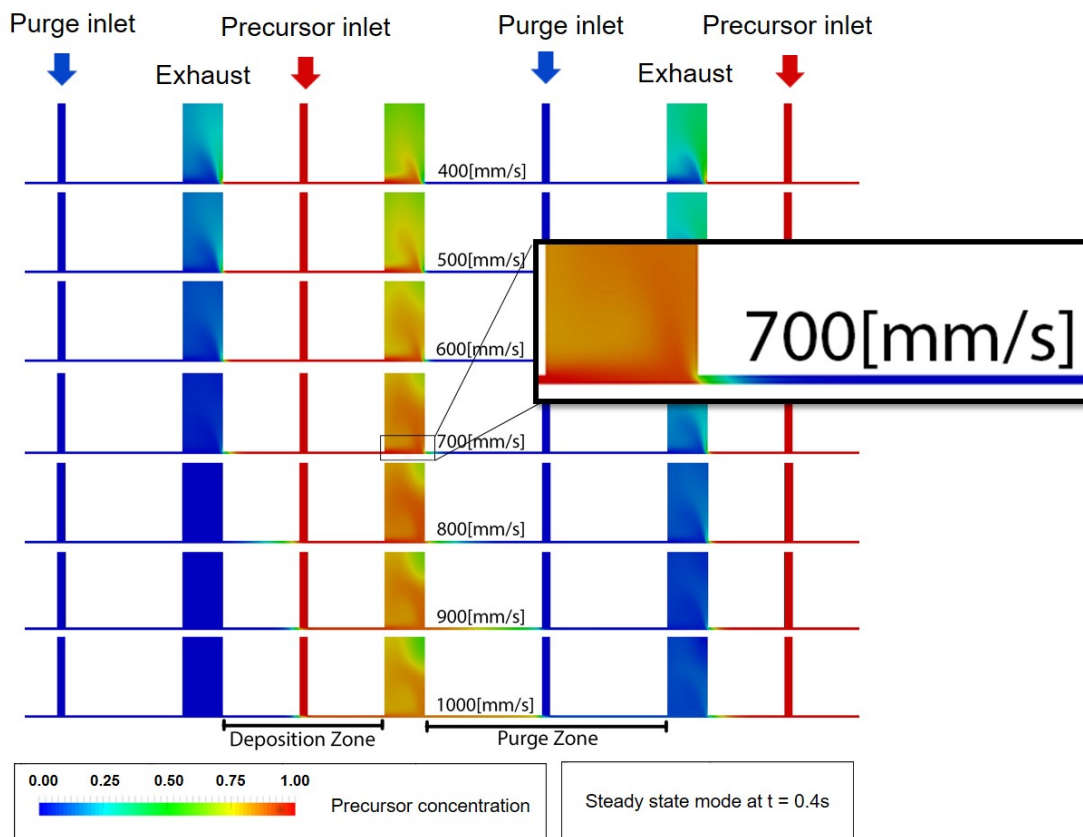
Figure 3.7.: Precursor concentration in dependence of the substrate velocity. Depicted are two precursor inlet, two purge inlets and two gas exhausts. Simulation results are taken in the steady mode (after 0.4 s). Further parameters were set to: Gap height 300 μm, injected gas flow = 1000 sccm, substrate temperature 350 K. Note that only the left-to-right-movement is simulated. The carrier gas is transported towards purge zone at a substrate speed of 700 mm/s, shown in more detail in the magnified view.

centration and carrier gas flow rate seem to have a negligible impact on the precursor distribution. This can be concluded from simulation results, in which the purge gas flow and the substrate velocity were set to zero (not shown here). In this case, there is no precursor transport into the purge gas zone (by convection), independent of the

precursor concentration and gas carrier gas flow rate. Figure 3.7 shows the results for the precursor distribution for different substrate velocities, up to 1000 mm/s. Note that only the one cycle of the ALD is simulated corresponding to the left-to-right movement of the substrate table. Purge and precursor gas inlets are supplied with 1000 sccm, respectively. It could be observed that the precursor gas is distributed asymmetrically due to movement of the substrate (left to right). The precursor gas gets carried to the gas outlet. This procedure of the complete exhaust of the precursor gas is valid to substrate velocities of 700 mm/s. By further increasing the substrate velocity, the injected precursor does not reach the left side of the deposition zone. Simultaneously, the carrier gas is transported beyond the gas outlet region towards the purge zone at the right side. At this point, intermixing with the other precursor species could not be ruled out in the other half cycle of the ALD process (as the substrate table moves to the left). Here, CVD like gas phase reactions become inevitable as soon as the precursor A, which is transported into the purge zone, reacts with precursor B, which is diffused into this region in the previous ALD cycle. The critical substrate velocity (for the shown domain) is reached at approximately 700 mm/s. Here, increasing the purge flow shifts the critical point towards higher substrate velocities linearly (not shown here). Decreasing the gap height also leads to an greater distance between the gas inlet and the intermixing point. All in all, these 2-D simulation results indicate that the precursor separation is practically guaranteed for the velocities used in this thesis (between 10-200 mm/s) and gas flow rates between 1000 sccm and 2000 sccm (with gap height of roughly 300 μm).

3.4 Dielectric barrier discharge plasma sources

The so-called dielectric barrier discharge (DBD) is the electric discharge between two electrodes, where at least one is separated from the outer gaseous atmosphere by a dielectric. The discharge takes place due to high field intensities in the process gas triggered by an AC voltage. This theory of operation could be realized in different arrangements, strongly dependent on the interplay between dielectric and discharge region. In principle, the discharge could take place in different arrangements: Started from a design similar to a capacitor, with a dielectric-gas-space between the electrodes, to embedded electrodes in a dielectric, leading to a surface dielectric barrier discharge (S-DBD).
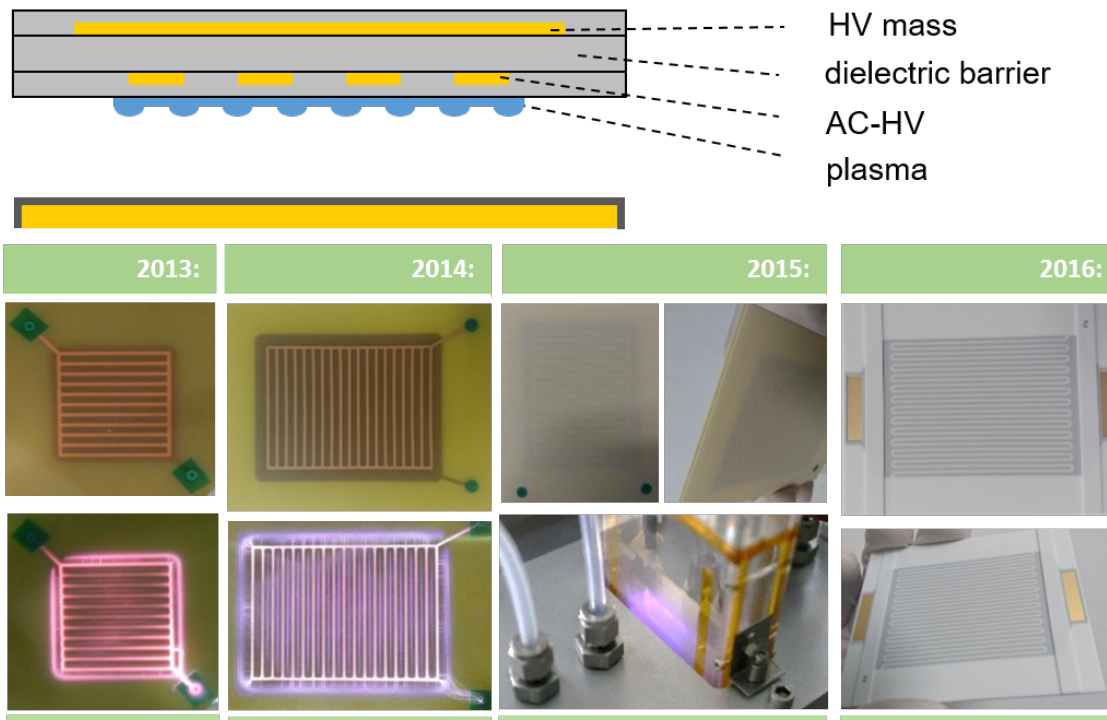
Figure 3.8.: Theory of operation of the DBD plasma source (schematic on top) the and different generation of DBD plasma sources used in the APP ALD sytems during this work made out of FR-4 (2013 and 2014) and ceramic material (2015 and 2016).

For the discharge operation of a DBD plasma source the presence of one or more dielectric layers (typically glass, quartz or ceramics) in the current path through the discharge gap is essential.[153] At atmospheric pressure the discharge takes place in very thin filaments with very short lifetimes, the so-called micro discharges.[154] By supplying an external voltage, the electrons are accelerated towards the anode while the respective ions remains fixed due to their high mass (compared to that of the electron). Because the electrons can not be transported through the dielectric, the charges are collected at its surface, forming an electric field in opposite direction compared to the one created by the external voltage. As of that, the microdischarges are rapidly quenched by a growing counter-field and the resulting attenuation of the electric field limits the overall discharge. The electric field strength breaks down to a value lower than needed for retention of the ionization, but leaves a low ionized plasma channel which favors the next plasma streamer.

The plasma sources used in this thesis are based on the surface dielectric discharge. All generations of plasma sources used are based on a two copper electrodes, separated by a dielectric material. While one of the electrodes is textured (as shown in Figure 3.8) its

counterpart is a continuous copper plate. The dielectric material used in this thesis was made out of FR-4 in the original design in 2013. FR-4 is a based on epoxy resin and fiber glass reinforcement. In 2013, these plasma sources were used to deposit TiO_x electron-extraction interlayers in inverted organic solar cells from titanium isopropoxide and an Ar/O_2 plasma.[136] Further designs of plasma sources were based on different ceramic materials to improve its stability and also the generation of plasma species. Compared to its design in 2013 (see Figure 3.8), the size of the plasma source (more precisely the design of the copper electrodes) was enlarged in the second generation in 2014 to enable bigger substrates. This plasma source with FR-4 dielectrics was basically used in the pulsed batch-based APP ALD. In continuous operation those plasma sources break down thermally due to surface erosion phenomena (triggered by accelerated oxygen radicals). On account of this, the next generation of DBD plasma sources were fabricated by thermally stable ceramic plates which were sintered together with the FR-4 dielectric (Generation 2015). These plasma sources enable the continuous operation in the spatial ALD setup. Note that the thickness of the outer ceramic layer had a strong influence on the plasma yield and therefore also on the thin film deposition. Here, a tradeoff between plasma yield and thermal stability had to be accepted. Since the outer ceramic could be too thin and (the thermally instable) FR-4 is still used as dielectric, the long-term stability of those plasma sources could be estimated to two to three months. For further improvement, full-ceramic plasma sources were sintered in a one-step process, guaranteeing massive thermal stability with lifetimes beyond one year and a sufficient plasma yield with a wide range in plasma power (Generation 2016).

3.4.1 Ozone concentration generated by the Ar/O_2 plasma

To quantify the number of oxidizing species generated per unit time by the Ar/O_2 plasma, the ozone concentration was measured directly behind the plasma inlet. Therefore an *OZONE ANALYZER BMT 964* by *BMT MESSTECHNIK GMBH* was used, which was mounted with gas tube to a single plasma inlet. It is important to note that the absolute quantity in ozone concentration is strongly dependent on the distance between plasma source and measuring sensor, since the maximum lifetime of ozone and other oxidizing species are limited to a few μm due to a limited lifetime. In addition, all ozone concentrations were measured in the equilibrium mode (after 20-30 s) and with a plasma source based on the 2015 generation. Figure 3.9a shows the dependency of the ozone concentration on the O_2 flow through the plasma source.
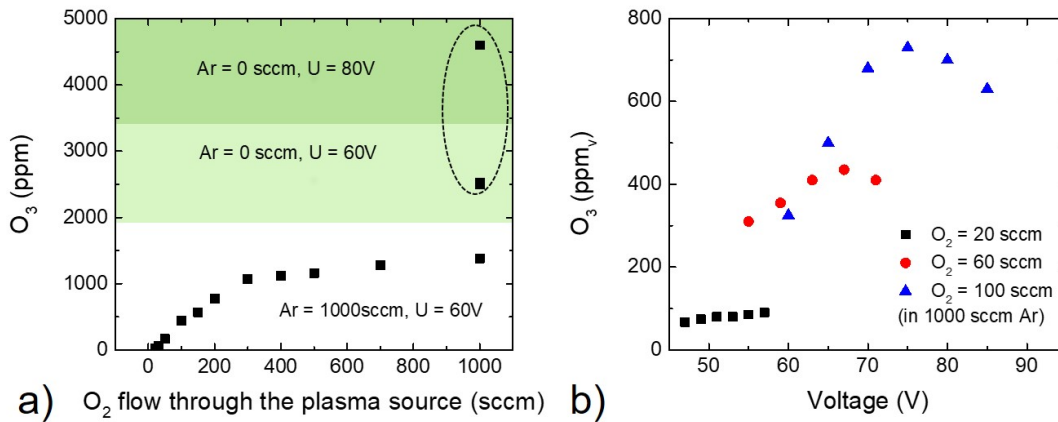
Figure 3.9.: Ozone concentration generated by the Ar/O_2 plasma in dependency on the O_2 flow through the plasma source (additonal to 1000 sccm argon). The mark represents a pure O_2-plasma (without additional argon purge). Additionally, the supplied voltage was increased from 60 V to 80 V. All plasmas were ignited with a external supply voltage with f = 13.4 kHz

The concentration increases rapidly for an O_2 flow smaller than 400 sccm at simultaneously constant plasma voltage and argon flow. 23 pmm of ozone are generated at an O_2 flow through the plasma source of 20 sccm, and up to ozone concentrations of 1120 pmm at 400 sccm. For higher oxygen flows a plateau of constant concentration forms. It can be assumed that at this point no more ozone could be generated by the plasma source due to its finite dimensions. By the operating a pure O_2 plasma, the ozone concentrations gets doubled. The ozone concentration generated by this pure oxygen plasma can be also enhanced by increasing the plasma voltage. As Figure 3.9b reveals, there is an maximum in the voltage, strongly dependent on the argon-to-oxygen-ratio used to ignite the plasma. While the flow of 20 sccm O_2 does not reveal a clear maximum in ozone concentration, higher oxygen flow rates (60 sccm and 100 sccm in 1000 sccm argon) reveal that the ozone yield peaked at voltages of 67 V and 75 V, respectively. As higher voltages can lead so single local plasma streams with high plasma intensities, the overall ozone formation could be lower. In addition, the continuous long-term operation with higher voltages (60 - 70 V) can not be guaranteed due to the development of heat, which either leads to thermal instabilities inside the plasma source material (especially in FR-4 based plasma sources) or the melting of the soldering.

3.5 Optical Ca test

The optical Ca test is a well-established method for determining the permeation rate of water (WVTR) through a barrier layer.[15,155,156] In practice, the optical Ca test is used to measure ultra-low WVTRs in the range of 10^{-6} gm^{-2}d^{-1} due to its higher sensitivity than commercially available instruments.[97] A WVTR of 10^{-6} gm^{-2}d^{-1} corresponds to the diffusion of 5 drops of water per day through an area as big as an american football field. To detect these small amounts of water, a highly accurate measuring method is necessary. The measuring principle of the Ca test is based on the degradation of calcium with water and oxygen, forming calcium oxide or calcium hydroxide. Despite the fact that the reaction of calcium with water is energetically preferred,[157] the reactions can be described roughly by the following three reaction equations:[158]

$$Ca + H_2O \longrightarrow CaO + H_2 \tag{3.2}$$

$$2\,Ca + O_2 \longrightarrow 2\,CaO \tag{3.3}$$

$$CaO + 2\,H_2O \longrightarrow Ca(OH)_2 + H_2 \tag{3.4}$$
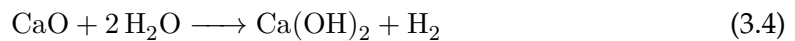
The optical Ca test is based on the fact that calcium is opaque as metal while calcium hydroxide is transparent. Thus, the optical transmission can be used to determine the amount of oxidized calcium and thus the water permeated through the barrier layer. Alternatively, the electrical calcium test exploits the fact that with increasing oxidation (or hydroxylation) the electrical conductivity of calcium decreases.[158–161] Further measurement methods are, for example, the Cavity ring-down spectroscopy[162] and the laser absorption spectroscopy. Both techniques are based on the principle that the quantity of water permeated through the barrier is detectable by laser absorption. Alternatively, permeated water molecules can also be detected with a mass spectrometer or with electrical sensors made of phosphorus pentoxide (also called the MOCON test[163]). Nisato et al. compare the different measurement methods and show the comparability of these tests, justifying the measuring principle of the optical Ca test.[155]

In addition, a distinction must be made between an *intrinsic* and an *integral* WVTR for all measurement methods of the water permeation. All measuring techniques mentioned above, except for the optical calcium test (without gas volume), measure an integral WVTR. The *integral* WVTR represents the amount of water permeation through the entire surface of the barrier (for example, a sensor). This measurement area includes macro defects due to dust particles etc. which, as described in subsection 2.2.1, lead to a significantly higher WVTR than the *intrinsic* WVTR, i.e. the minimum possible WVTR for this barrier in absence of macro defects.[84] The latter can be studied by minimizing the

measurement area, i.e. the sensor size.
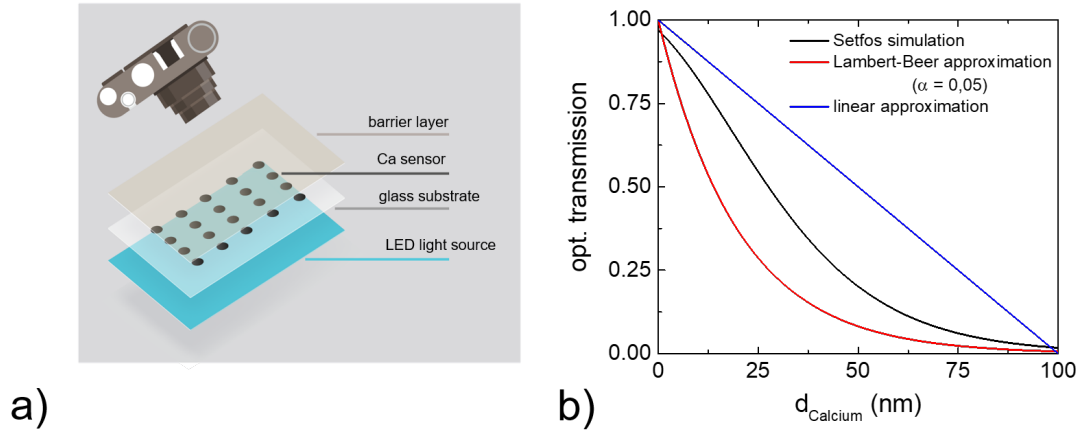
Figure 3.10.: a) Principle of the optical calcium test to determine the WVTR. A CCD kamera detects the optical transmission of (blue) light through the substrate/calcium/barrier stack. b) Optical Transmission vs. thickness of the calcium sensor: Ca thickness could be determined using optical simulation based on a transfer-matrix algorithm (Setfos). Other approaches are the exponential decay based on Lambert-Beer (absorption coefficient α = 0.05 by ref.[84]) or linear approximation.

Figure 3.10 shows the optical Ca test. 50-100 nm thick Ca sensors (2 mm diameter) are evaporated on a substrate and are encapsulated by the barrier film to be tested. A LED-Panel serves as a spectral (polychromic) light source with a main peak at 464 nm wavelenght. The optical simulation (via transfer-matrix algorithm) for the glass-Ca-Ca(OH)$_2$-Al$_2$O$_3$ stack was conducted for this wavelength. The barrier film as well as the thickness of the Ca-Ca(OH)$_2$-stack were simulated to be 100 nm, respectively. The change in the optical transmission in dependence on the calcium sensor thickness is shown in Figure 3.10b. In addition, the exponential trend according to the law of Lambert-Beer and the linear approach was taken into account as an upper and lower limit to approach the WVTR. The light transmittance through a calcium layer of homogeneous thickness d is described by the Lambert-Beer law as follows:[84]

$$I_L = I_{L,0} \cdot exp(-\alpha \cdot d) \tag{3.5}$$

Here, $I_{L,0}$ is the light intensity of the light panel and I_L represents the light intensity passing the barrier layer. Note, that the optical transmission based on Lambert-Beer (as shown in Figure 3.10) neglects optical reflection. In contrast, the optical simulation considers optical reflection. A CCD-Kamera serves as a optical detector, measuring the

incoming light with high spatial resolution. The light intensity is digitally decoded into a grey value. Here '0' represents no incoming light. '255' is the maximum intensity. The change in the grey value is transferred to the according change in transmission ΔT, which could be directly assigned to a change in the thickness of the calcium sensor Δd. The latter is used to determine the WVTR, via Equation 2.29.

In addition, the WVTR at different storage temperatures can be used to obtain the activation energy, as already discussed in subsection 2.2.2, and to extrapolate the theoretical barrier properties at room temperature. In parallel to the different methods of measuring the WVTR, storage conditions as reported in literature differ dramatically. Testing of barriers at 25°C / 60% r.H. (*room temperature conditions*) and 38°C / 90% r.H. (*tropical conditions*) seem to be quite dominant in literature, but even the highly performing gas diffusion barrier are measured under *damp heat conditions* (85°C / 85% r.H.).
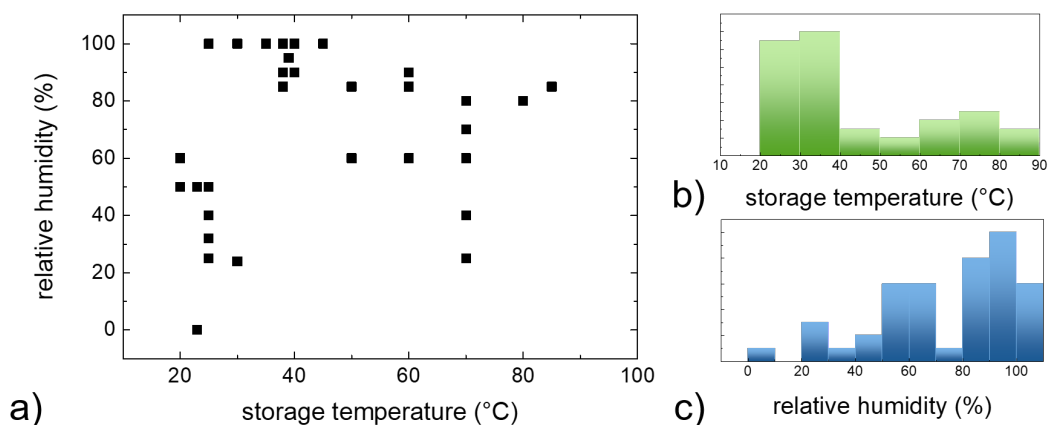
Figure 3.11.: Storage conditions for barrier performance tests: a) Climate conditions for barrier performance tests in literature b,c) Histograms on the frequency of the respective temperature or relative humidity.

Figure 3.11 depicts the storage conditions for barrier performance tests in literature. Clearly, there is no common consensus in the field of barrier tests, as emphasized by Nisato et al.[155] Despite the two standards for barrier tests as mentioned above, in this work, storage conditions of 60°C and 60% r.H. were chosen. Note that the measuring signal of the barrier measuring technique correlates strongly with the storage conditions of the sample. The choice of the storage conditions are a trade-off between sufficient measuring signal (i.e. sufficient calcium degradation), measuring time and a sufficient lifetime of the respective calcium sensor. On the one hand, high storage temperatures can lead to the short-term destruction of the calcium sensors due to the exponential activation of permeation, as already discussed in subsection 2.2.1). On the other hand,

at low storage temperatures permeation is slowed down, leading to minor amounts of calcium corroding to calcium hydroxide and an (apparent) negligible change in optical transmission in the optical Ca-test. For a sufficient signal-to-noise ratio, measurement times could exceed several weeks. To compare barrier quality at different storage conditions, it is necessary to determine the activation energy and to calculate the WVTR at RT.

3.6 Rutherford Backscattering Spectrometry / Nuclear reaction analysis

Rutherford Backscattering Spectrometry (RBS) is an non-destructive analysis technique using the scattering characteristics of high-energy ions to determine the thin film structure (e.g. the depth distribution) and its composition. Even if its idea goes back to Ernest Rutherford, who investigated the scattering patterns of ^{4}He$^+$-ions with gold foil in 1911[164](and proved the existence of the proton), its use as analysis tool has been first reported by Rubin et al. in 1957.[165]
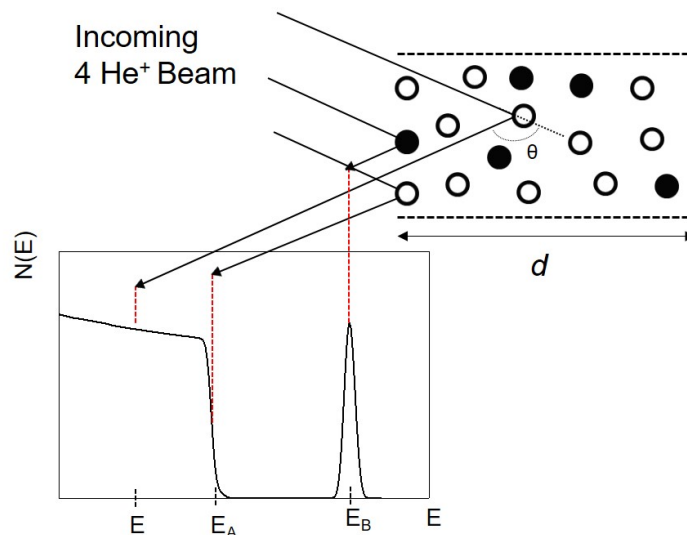
Figure 3.12.: Basic principles of Rutherford backscattering analysis. The RBS spectra of two different elements (e.g. Sn and O) are depicted in different depth. The incoming beam is scattered by different atoms in different depth, leading to different signals in the energy spectra. Inspired by ref.[166]

The heavy ionized particles with short range in solid matter (approximately 100 nm to several micrometer), typically helium or hydrogen ions, are accelerated towards the sample. A variety of the nuclear interactions can be used for evaluation of elemental composition and depth profiling of individual elements. In Figure 3.12 the basic principle of RBS as well as a typical spectra is shown. The incoming beam (e.g. ^{4}He$^+$ ions) is accelerated towards the substrate. While some ions are scattered elastically by surface atoms, others lose energy and are backscattered at various depths. As of that, the number of backscattered particles as a function their energy is measured revealing the information on the nature of the various elements present in the target sample and their depth distribution.[166] A narrow shape of the respective peak (e.g. E_B in Figure 3.12) reveals a clear depth distribution, while a wider shaped peak represents the measuring signal of target atoms in various depths (e.g. in the target film as well as in the substrate). In practice, the measuring signal for $E < E_A$ is reasoned by the scattering of the substrate, e.g. of silicon atoms of a SiO_2 substrate. For RBS the energy of the elastically scattered ion is measured with a detector in a certain angle, depending on the energy of the incoming beam (E), the mass of the scattered atom (represented by the atomic numbers Z_1 or Z_2) and the angle (e.g. θ).[167] Taking this into account, the general cross section for elastic scattering of ions can be calculated as follows:[165, 167]

$$\frac{d\sigma}{d\Omega} = \left(\frac{Z_1 Z_2 e^2}{4E sin^2(\frac{\theta}{2})} \right)^2 \tag{3.6}$$

As of that, the Rutherford scattering cross-section represents the probabilty of a scattering event to occur. Note that this general cross section (and therefore the sensitivity of RBS) increases with increasing Z_1 and Z_2 and decreases with the energy E. That is why, RBS is sensitive for heavy elements, but less sensitive for light elements. For light elements such as lithium, carbon, nitrogen or oxygen NRA (nuclear reaction analysis) provides an opportunity. Commonly the target is irradiated with a deuteron beam (D-NRA) to induce nuclear reactions. These nuclear reactions generate alpha- and gamma radiation, which can be measured. Depending on the respective nuclear reaction, this radiation has a sharp energy peak, following the cross section for the non-elastic scattering. Analogous to RBS, the energies of detected particles are characteristic of the target element specific nuclear reaction and therefore of the element in the sample.

For the measurements in this work, Rutherford backscattering (RBS) and nuclear reaction analysis (NRA) were performed at a 4 MV tandem accelerator of the RUBION facility at University of Bochum (Germany). For RBS a 2 MeV ^{4}He$^+$ ion beam in com-

bination with a silicon surface barrier detector at an angle of 160° was used. The beam current was set to 20-40 nA. For a higher sensitivity (as mentioned above) to atoms with low atomic numbers, i.e. C, N and O, the complementary NRA measurements were performed with (a lower energy) 1 MeV ^{2}H$^+$ beam with a beam current of 40-80 nA. A silicon surface barrier detector was placed at an angle of 135°. An additional 6 micrometer thin (nickel) foil was placed right in front of the detector to eliminate scattered (undesired) particles.

4

Al$_2$O$_3$-based gas diffusion barriers by atmospheric pressure ALD

In this chapter, the growth of Al$_2$O$_3$ thin films as transparent gas diffusion barriers at atmospheric pressure is investigated. Therefore, the metal oxide layers were deposited in a home-built batch based plasma enhanced ALD system. Moreover, barrier films were deposited in a spatial ALD with different oxidants (plasma, ozone, water). All Al$_2$O$_3$ films were fabricated with TMA as metal precursor. The respective ALD reactions are already described in subsection 2.1.1. The resulting Al$_2$O$_3$ films show ultralow WVTRs on the order of 10^{-6} gm^{-2}d^{-1} comparable to those prepared by conventional vacuum based ALD.

4.1 Batch-based plasma ALD at atmospheric pressure

In the following, the Al$_2$O$_3$ growth in the batch-based APP ALD reactor at a substrate temperature of 80°C will be discussed. The setup as well as the typical pulse sequence and the gas flows are described in section 3.2. Trimethylaluminium (TMA) was chosen as the metal precursor. As co-reactant, an Ar/O$_2$ plasma was used for all processes.

Unless otherwise noted, the Al$_2$O$_3$ growth is analyzed in a remote, downstream position of the substrate.

4.1.1 Direct and remote position

First experiments in the batch-based ALD system reveal two different regimes of thin film deposition, depicted in Figure 4.1a and Figure 4.1b. Here, 400 cycles of an alternat-
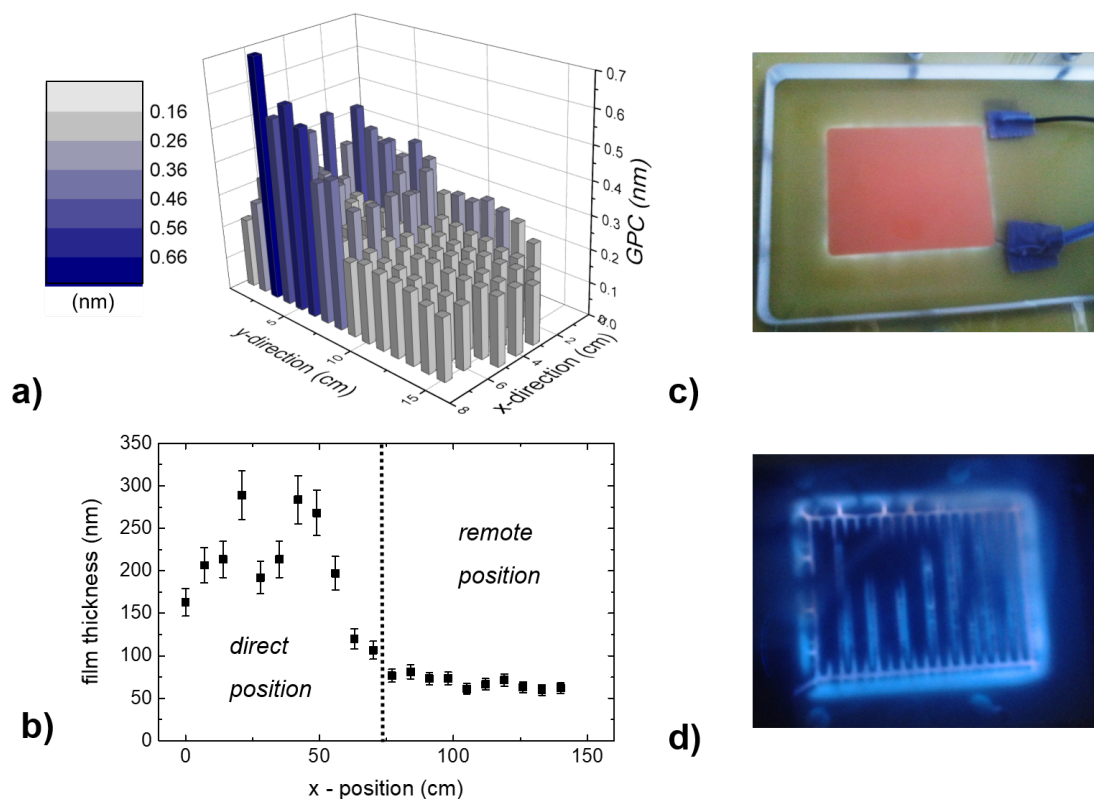
Figure 4.1.: Direct and remote position in the batch-based APP ALD reactor: (a) Distribution of the film growth is measured on silicon substrate. (b) 400 cycles of TMA/plasma reveal a homogeneous downstream film growth, the so-called remote position (in y-direction) starts at 75 mm. Picture of the enlighted plasma source from top (c) as well as from underneath (d).

ing TMA/purge/Ar/O$_2$-plasma/purge-sequence were performed on silicon substrates, revealing inhomogeneous growth in the regime located directly underneath the plasma source at the gas inlet of the reactor. This regime with a high GPC is strongly affected by the electrode structure of the plasma source, basically the outer edges of the copper electrode. In Figure 4.1c and Figure 4.1d the light emission of the plasma is shown. These

pictures reveal that the strongest plasma luminescence is found at these outer edges of the structure. Due to the inhomogeneous high field strengths of the surface dielectric barrier discharge, nonuniform film growth (comparable to CVD kind of growth) is observed in the direct position. Here, CVD growth defines not self saturated growth, which has to be clearly distinguish from ALD kind of growth. It can be assumed that the plasma and the resulting high temperatures lead to decomposition of the precursor species and to an additional CVD reaction inside the gas phase, comparable to the critical high temperature regime in the ALD window compare Figure 2.4. In addition to this inhomogeneous film growth, occasional arcing from the plasma source to the samples is observed. For ITO coated PET substrates, the latter even leads to the destruction of the substrates. In the ($70 \times 70 \, \text{mm}^2$ wide) remote position, (roughly $75 \, \text{mm}$ away from the gas inlet) homogeneous film growth is observed with a GPC between $0.16 \, \text{nm}$ and $0.18 \, \text{nm}$. In addition, slightly higher GPCs are observed near the border of the reactor, probably due to not ideal fluid dynamics inside the reactor. Additionally, colder reactor walls also could lead to higher GPCs, as growth of metal oxides has a strong temperature dependency. For most metal oxides (like Al_2O_3, TiO_2 or SnO_x) film growth per cycle is increasing with towards lower deposition temperatures (in this temperature regime). Due to the inhomogeneity and the destruction of the foil substrates in the direct position, all following experiments in the batch-based ALD setup are carried out in the remote position.

4.1.2 ALD film growth

To verify the ALD characteristics of the thin film growth, it is required to depict the self-limitation of the precursor adsorption resulting in a saturated GPC. The self-limitation of the ALD process is verified by varying the precursor doses, i.e. the pulse length of TMA and the plasma sequence. Saturation is reached when increasing the amount of precursor does no longer lead to higher FPC. The results of the corresponding study are shown in Figure 4.2. The error bars result from the standard deviation of more than three measurements. The dotted lines are fits to the data, expressing a Langmuir-isotherme behavior for the coverage of the sorption sites, as already discussed in subsection 2.1.1. Here, the precursor partial pressure p is substituted with the precursor dose time. The surface coverage in the langmuir-isotherm model is expressed by the GPC. To distinguish between the unsaturated and the saturated part in the chemical reaction, the following experiments are carried out with one precursor in saturated dose, respectively. For the variation in the amount of TMA a plasma time of $10 \, \text{s}$ is chosen (with 150 ALD

cycles). For the variation in plasma time a TMA pulse length of 2 s is chosen (with 150 ALD cycles). Under these saturated conditions, a GPC of (0.18 ± 0.02) nm on silicon is observed.
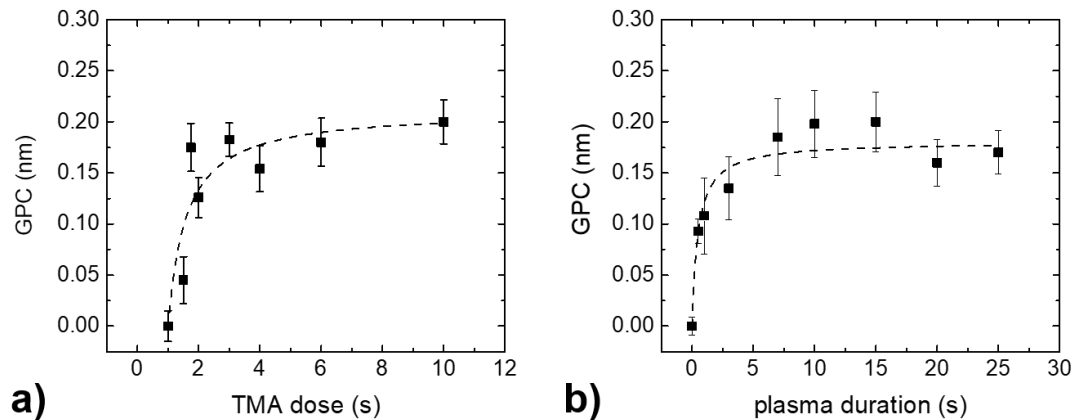
Figure 4.2.: Self-limitation of Al$_2$O$_3$ in the batch-based APP ALD: GPC vs. TMA pulse time (a) and plasma pulse time (b). All films were deposited at 80°C substrate temperature. Based on ref.[1]

The effect of parasitic CVD due to residual moisture in the reactor has been determined by a reference run without plasma, leading to a GPC of less than 0.03 nm/cycle. Obviously, saturation is reached after enhancing the TMA pulse times to more than 2 s and the plasma time to more than 7 s. Note that extending the purge time from 15 to 90 s does not change the GPC (see Figure 4.3b). The observed GPC values are roughly the same as those reported for low-pressure plasma enhanced ALD of Al$_2$O$_3$ at low temperatures (0.18 nm at 70°C,[168] 0.178 nm at 25°C[24] and 0.16 nm at 50°C[56]). The GPC values reported for plasma-based ALD are generally higher than the GPC values of thermal ALD with TMA/water at comparable temperatures, which is around 0.12nm (our own measurements at 80°C and Groner et al.[163, 169]). Aside from a potentially lower mass density, other explanations for this phenomenon have been presented by Heil et al.[168] Surface reactions of the plasma with the methyl groups of the adsorbed TMA on the substrate surface could lead to secondary thermal reactions of TMA with H$_2$O molecules. Additionally, it is reported that the plasma can create a larger number of active surface sites for TMA adsorption than the thermal oxidation by water at the same temperature.[168] This underlines the general argument of a not fully saturated oxidation by using H$_2$O as oxidant at low temperature (80°C). For atmospheric pressure thermal ALD from TMA/water a GPC of 0.20 nm at 100°C has been reported.[134] The higher GPC for atmospheric pressure thermal ALD compared to low pressure thermal ALD

has been explained by an excess of adsorbed water, leading to an additional CVD type of growth. For spatial ALD of TMA/water at atmospheric pressure, GPC values roughly between 0.1 and 0.2 nm have been reported depending strongly on water partial pressure, substrate temperature, and substrate speed, where the latter is corresponding to the precursor exposure times[21].[170]

Taking a 2/15/5/10/15 s ALD sequence into account (compare Figure 3.2), this growth results in 0.2 nm/min, obviously strongly dependent on the choice of purge time which is of crucial importance for ALD processes at atmospheric pressure.[135] Compared to a typical 0.3/10/2/10 s sequence in a TMA/plasma-based process in a commercial setup at 1 mbar process pressure, which lead to approximately 0.5 nm/min, the batch based atmospheric pressure process needs twice as long as the low pressure analogue. In principle, those cycle times, especially the purge times, are strongly dependent on the reactor volume and the dose of metal precursor (i.e. TMA). An increase in the dose of metal precursor would require higher purge times.
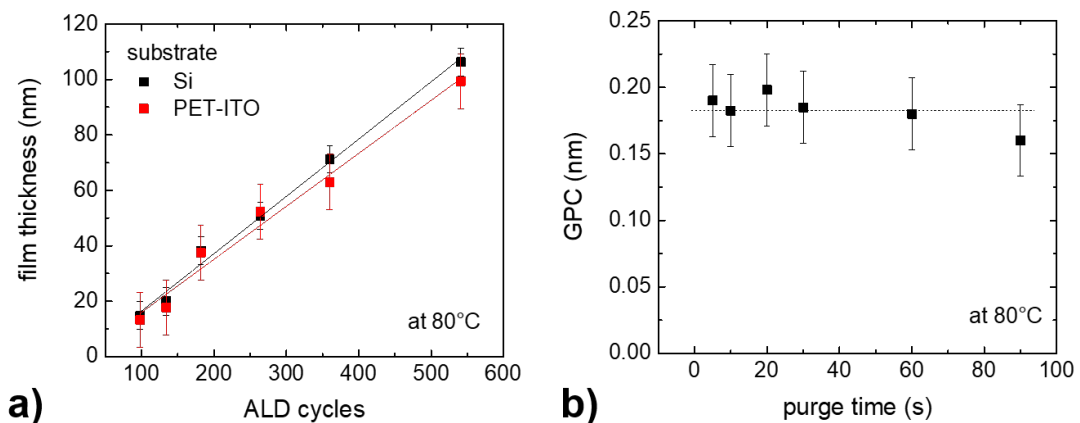
Figure 4.3.: a) Linearity of ALD growth of Al_2O_3 in the batch-based APP ALD on silicon and (pre-heated) flexible ITO coated PET substrate. All films were deposited at 80°C in remote position. b) GPC vs. ALD purge time (measured on silicon). Based on ref.[1]

In addition to the precursor saturation, a linear film growth can be observed with a growth per cycle (GPC) of (0.19 ±0.02) nm on silicon and (0.18±0.02) nm on the PET-ITO foil (130 nm ITO on 125 μm thick PET), see Figure 4.3a. No significant difference concerning the growth behavior could be observed for the different substrates. Especially, no delay in film growth is observed on the foil substrate due to its ITO top-coating. In general, the growth behavior of ALD on polymers is strongly depend on the precursor being used as well as the detailed process conditions, observing either clean surface

growth or substantial sub-surface diffusion of the precursor molecules inside the polymer surface.[171] Note that all polymer substrates used in this work are pre-baked before the deposition process in an oven at 80°C for at least 12 h to reduce the amount of residual water in the foils. For all shown deposition processes, both precursors doses are set to the respective saturation regime ($t_{TMA} = 2$ s, $t_{Plasma} = 10$ s).

4.1.3 Barrier properties

Barrier properties of the Al$_2$O$_3$ thin films are investigated via the optical Ca test, introduced in section 3.5. The encapsulation of the evaporated calcium sensors require continuous inert gas atmosphere due to the oxidation of the Ca in presence of water (and oxygen). This inert atmosphere could not be guaranteed after the deposition in the batch-based ALD system as the system is not placed inside a glove box. This is why an inverse optical Ca test is performed. Therefore, Al$_2$O$_3$ is deposited on a highly water-diffusive substrate like PET-ITO foil in a first step.
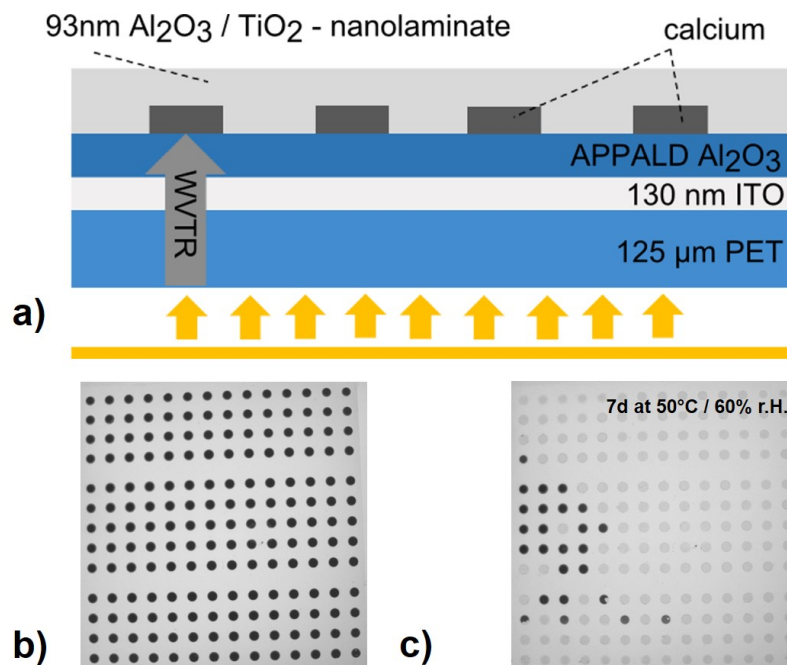
Figure 4.4.: Stack used for optical Ca test of Al$_2$O$_3$ deposited via batch-based APP-ALD. The top encapsulation is based on an low pressure ALD Al$_2$O$_3$/TiO$_2$ nanolaminate (a), exemplary picture of the Ca-sensors directly after depositon as well as after seven days at enhanced climate conditions (50°C/60% rH) (b).

Afterwards, calcium is evaporated and transferred in inert atmospheric conditions to the low-pressure ALD which is equipped with a load lock, enabling the encapsulation with a top encapsulation layer directly on the calcium sensors. For the top encapsulation layer it has to be assumed that it functions as 'perfect' barrier with a permeation rate substantially smaller than that of the layer under investigation. Actually, barriers similar to those used as of the top-encapsulation have shown a WVTR orders of magnitude lower than the WVTR expected for the investigated thin film e.g. 5×10^{-7} gm^{-2}d^{-1} even under damp heat conditions (70°C/70% rH).[172–174] On the other hand, the WVTR of the PET foil is almost negligible if the WTVR is significantly higher than those of the investigated barrier film (in the orders of magnitude). PET shows a WVTR of 2×10^{-1} gm^{-2}d^{-1}, the ITO coated PET (as used typically in this work) a WVTR of 4×10^{-2} gm^{-2}d^{-1} as well as the PEN a WVTR of 6×10^{-2} gm^{-2}d^{-1} at RT. The actual WVTR of the Al_2O_3 could be calculated using the Equation 2.30. The overall deposition sequence, necessary for the inverse optical Ca test is shown in Figure 4.4a. PET-ITO foil is used as substrate. 100 nm of Al_2O_3 were deposited via APP-ALD. Calcium sensors (typically 15x15) are evaporated (see Figure 4.4b) and encapsulated with a low-pressure ALD based Al_2O_3/TiO_2 nanolaminate without exposure to ambient air. Figure 4.5a shows the optical transmission of a (representative) array of calcium sensors depending on the storage time (stored at 50°C and 60% rH). The optical transmission rises from 14.1% up to 14.8% in the first 150 hours. This change in optical transmission corresponds to a decrease in calcium thickness from 58.1 to 57.2 nm. Thus, 0.9 nm of the calcium layer is corroded to calcium hydroxide due to the water vapor transfer through the thin film. From this data, the WVTR can be calculated to 1.9×10^{-4} gm^{-2}d^{-1} (at 50°C/60% rH). Since the water permeation is a thermally activated process (activation energy E_A = 58 kJ/mole[15689]), the corresponding WVTR at room temperature can be estimated to 3.1×10^{-5} gm^{-2}d^{-1}.

Figure 4.5d reveals that the WVTR is roughly constant for the deposited Al_2O_3 layers with a thickness in the range of 30–100 nm. The average WVTR is 5×10^{-5} gm^{-2}d^{-1}. These values for the WVTR are typically averaged for five calcium sensors and could be understood as a representative intrinsic WVTR. As some sensors degrade already within the first few hours, the overall (integral) WVTR is higher, but also strongly dependent on the fabrication process and the presence of dust particles. The (inverse) optical Ca tests on polymer substrates show remarkable more statistical sensor failure, than those performed on rigid glass substrates. However, for comparison, 100 nm Al_2O_3 deposited at 80°C by thermal (low pressure) ALD show a WVTR of 1.1×10^{-5} gm^{-2}d^{-1}. Carcia et al. reported 6×10^{-6} gm^{-2}d^{-1} for 25 nm thick films deposited by low pressure thermal ALD at 125°C.[156] On the other hand, a WVTR of 5×10^{-3} gm^{-2}d^{-1} is reported for 20 nm thick films deposited by low pressure plasma ALD at room temperature.[175] The
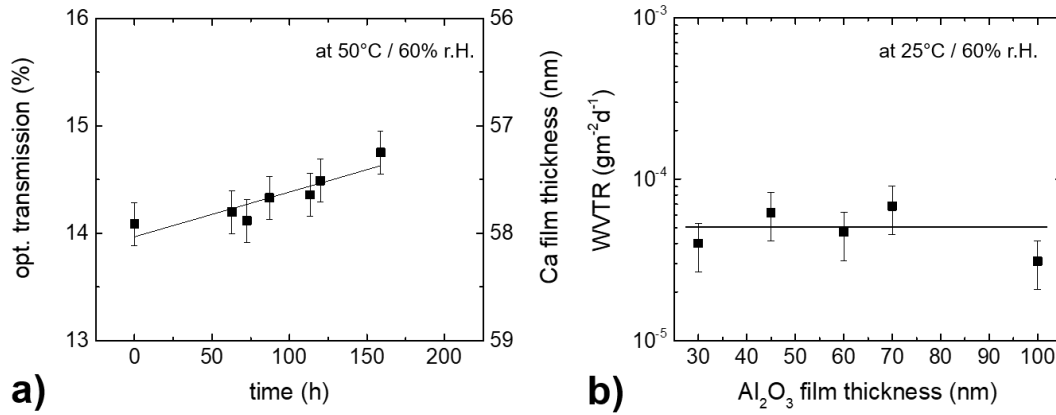
Figure 4.5.: Optical Ca test of Al$_2$O$_3$ deposited via batch-based APP-ALD: a) Linear approximation of the optical transmission (λ = 464nm) through a 100nm Al$_2$O$_3$ film as a function of time (stored in a climate cabinet at 50°C/60% relative humidity). b) Dependence of the WVTR on the Al$_2$O$_3$ layer thickness. The WVTR values were extrapolated to RT conditions as described above. The mean WVTR (represented by the black line) is 5 $\times$ 10^{-5} gm^{-2}d^{-1}(d). Based on ref.[1]

somewhat higher WVTR for thin films deposited at atmospheric pressure (plasma enhanced) and low pressure ALD could be explained by different film properties, shown in Table 4.1.

Table 4.1.: Film properties of APP ALD and low pressure thermal ALD: GPC, refractive index n (at 632 nm), density (measurend by XRR) and WVTR

100 nm Al$_2$O$_3$	APP ALD	LP ALD
GPC (nm)	0.18	0.12
n	1.56	1.61
density (ρcm^{-3})	2.3	2.6
WVTR (gm^{-2}d^{-1}) (at 60°C/60% rH)	4.1 $\times$ 10^{-4}	1.0 $\times$ 10^{-4}
WVTR (gm^{-2}d^{-1}) extrapolated to RT	4.2 $\times$ 10^{-5}	1.1 $\times$ 10^{-5}

The refractive index n, which for otherwise similar materials is known to be indicative for the mass density, has been measured for Al$_2$O$_3$ layers with a thickness of 100 nm. APP ALD-based Al$_2$O$_3$ shows a refractive index (n=1.56) lower than that of the low pressure analogues, but slightly higher than those reported by Poodt et al. for Al$_2$O$_3$ layers deposited by thermal ALD at atmospheric pressures.[176] Low pressure ALD leads to refractive indices of n = 1.61, which is an agreement with literature[177].[178] The dif-

ference in film density can be confirmed by XRR. Here, APP ALD-based Al_2O_3 has a density of $2.3\,gcm^{-3}$ whereas the low pressure analogues films show film densities of $2.6\,gcm^{-3}$. On the grounds of that, the WVTR varies between the low pressure thermal and the atmospheric pressure plasma-based Al_2O_3 thin films.

4.1.4 Optical and mechanical properties

As long as the Al_2O_3 barrier is not directly deposited on an opaque electrode of the organic or perovskite solar cells, it has to show high optical transmission. In addition, roll-to-roll production as well as the demand for flexible devices require a high mechanical flexibility.
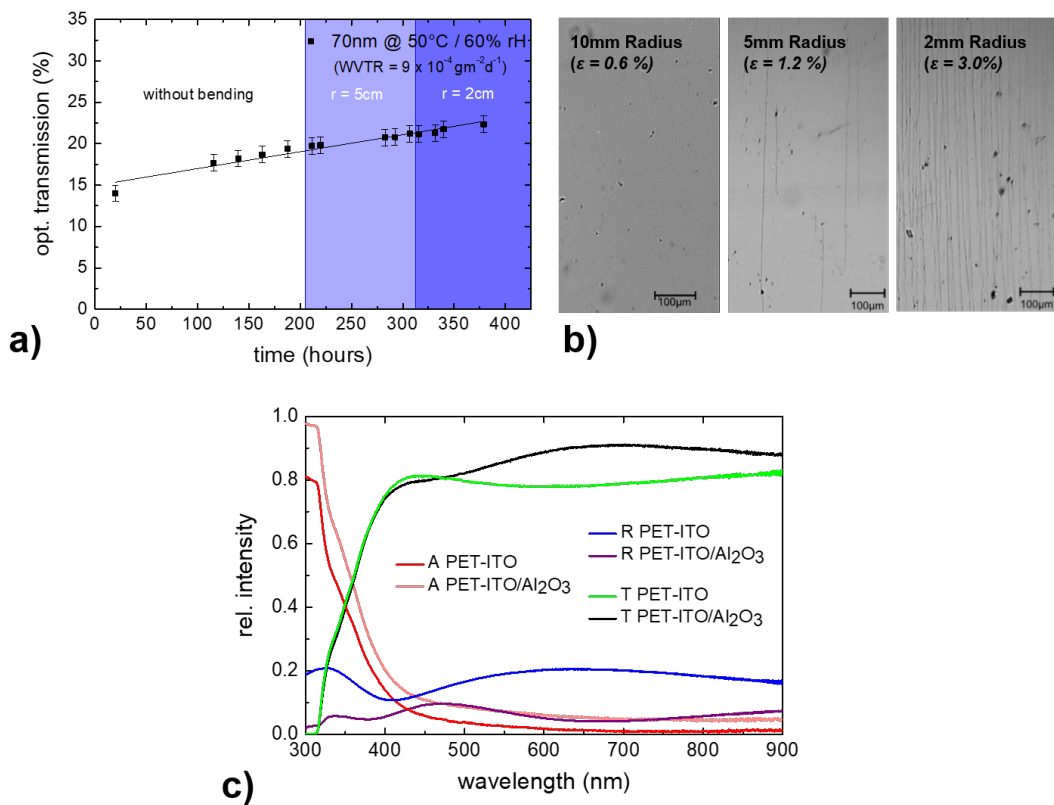
Figure 4.6.: Mechanical properties of Al_2O_3-based on Batch APP ALD: a) Optical Ca-test under mechanical stress. A 70 nm thick Al_2O_3 encapsulation (stored at 50°C/60% rH) were bended with a bending radius of 5 cm and 2 cm, respectively. b) Cracking of Al_2O_3 on PET-ITO substrate at different mechanical stress investigated by optical microscopy. c) Optical properties (absorption, transmission, reflection) of 100 nm thick Al_2O_3 on PET-ITO substrate.

Therefore, the optical Ca-test were performed under mechanical stress at moderate bending radii, shown in Figure 4.6a. Obviously, the slope in the optical transmission vs. time stays unchanged even under higher mechanical stress, linked with a constant WVTR of 9×10^{-4} gm^{-2}d^{-1} at (stored at 50°C/60% rH). Therefore, the intrinsic barrier properties remain unchanged. The crack formation is examined in Figure 4.6b. No crack formation could be observed for bending radii larger than 10 mm. Cracks starts to form at 5 mm bending radius, corresponding to a mechanical strain $\epsilon = 1.2\%$. At this point, it can be assumed that the barrier properties will be severely deteriorated. Note that the crack formation could not be unambiguously attributed to the Al$_2$O$_3$ layer because of crack formation in the ITO layers at increasing strain levels, respectively. Here, fluorescent tags are needed to visualize defects in Al$_2$O$_3$ thin films.[179]

Nevertheless, these findings are in good agreement with the mechanical properties of other metal-oxide thin films for which critical strain levels for the onset of crack formation in the order of 1.3% have been reported.[180,181] In addition, optical properties of 50 nm and 100 nm thick Al$_2$O$_3$ coated PET-ITO is investigated and shown Figure 4.6c. The combined Al$_2$O$_3$/PET-ITO stack show an optical transmission above 80% in the visible spectral region and low absorption below 10%. A slight Fabry-Perot effect could be observed for wavelengths larger than 450 nm.

All in all, mechanical and optical properties verify batch-based APP ALD Al$_2$O$_3$ to be the use for high performance barrier layers in flexible electrical devices.

4.2 Spatial atmospheric pressure ALD

In section 4.1, plasma enhanced atomic layer deposition at atmospheric pressure has been presented in a batch-based APP ALD system. With the experience from atmospheric DBD plasmas taken from the batch APP ALD system, the concept is transfered to a spatial ALD setup. Here again, the self-limiting ALD growth of the process has to be provided. The resulting film quality of the deposited thin films (in terms of density, barrier properties etc.) only could be accomplished by the self-limiting surface reactions as basis for the ALD process. In addition, the spatial separation of precursors has to be ascertained to avoid uncontrolled CVD.

In this chapter, all barrier thin films were deposited by trimethyaluminium and an Ar/O_2 plasma, water or ozone as oxidant, respectively. First, the influence of the precursor flows and the process temperature on the film growth is studied. Furthermore, film properties as WVTR or density are assessed. The discussion of substrate speed is excluded and is given seperate attention chapter 6. All samples are grown with a with a substrate speed v = 17 mm/s, which guaranties saturated growth with the respective gas flows.

4.2.1 ALD film growth

The saturation of the GPC of the ALD process is shown in Figure 4.7 for TMA/plasma and TMA/H_2O processes. Therefore, the amount of the carrier gas through one of the ALD precursor bubblers was varied while the flow of its counterpart is kept constant. The deposition temperature was set to 75°C. The amount of precursor is controlled by the amount of N_2 flowing through the respective precursor bubbler. The dose of oxidizing species generated by the Ar/O_2 plasma is represented by the amount of O_2 flow through the plasma source. The suitability of this kind of assumption is discussed in more detail in subsection 3.4.1. The saturation in the GPC could be found with a N_2 flow bigger than 5 sccm through the TMA bubbler and 10 sccm O_2 flow through the plasma source (in 2000 sccm argon). The GPC saturates at (0.16±0.02) nm. In both experiments the respective other precursor was chosen in an over-saturated level, so that the lower GPC in the none-saturated regime can clearly be attributed to the respective precursor under study.

In contrast to the plasma-based analogues water-based processes do not show saturation at 75°C deposition temperature. Here, increasing the amount of N_2 flow through the water bubbler lead to a linear increase in GPC. Saturation could be observed for

water-based processes deposited at a temperature above 100°C with a saturated GPC of (0.12 ± 0.02) nm. Note, the saturation in GPC in Figure 4.7c is achieved by choosing 4 sccm N$_2$ through the water bubbler. The not self-limiting growth in Figure 4.7d can be explained by multilayer adsorption of water at the surface of the substrate due to its high sticking coefficient at low temperatures[53].[150] This water adsorption contradicts the ALD characteristics in the respective process. Generally speaking, the observed values for the GPC are comparable to those of Al$_2$O$_3$ films grown by atmospheric pressure batch ALD (GPC = 0.18 nm, see section 4.1) and to those grown by low-pressure plasma ALD (GPC = 0.16 nm at 70°C,[182] 0.17 nm at 25°C[62]).
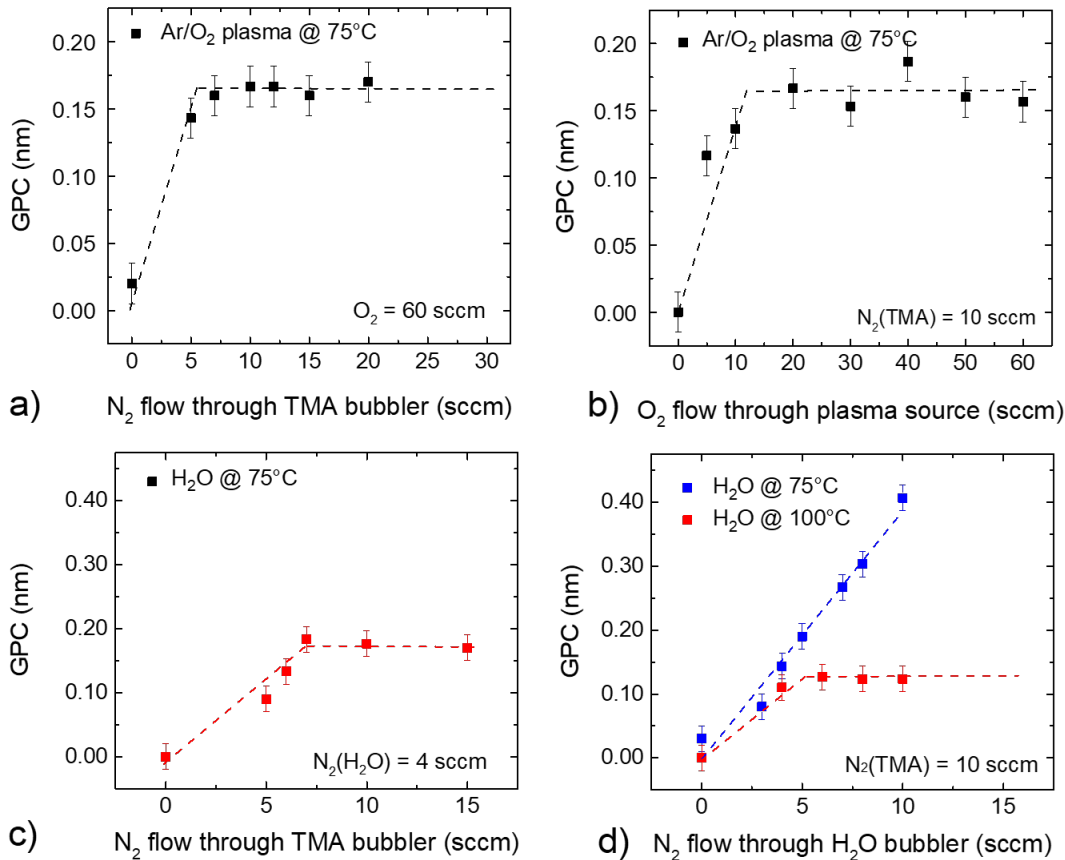
Figure 4.7.: Saturation of spatial ALD of TMA/plasma (a,b) and TMA/H$_2$O (c,d) processes und at 75°C und 100°C deposition temperature. O$_2$ was chosen as dimension representing the amount of oxidizing species generated by the plasma. All processes were deposited at a substrate speed of v = 17 mm/s. Based on ref.[2]

With saturated precursors flows, the distribution of the film growth within the spatial ALD reactor could be estimated. Therefore, a TMA/plasma process is performed at

75°C on a $70\times70\,\text{mm}^2$ glas substrate. Figure 4.8 shows the distribution of the Al_2O_3 film thickness. Here, the x-direction represents the direction of movement. The average GPC can be estimated to $(0.16\pm0.01)\,\text{nm}$.
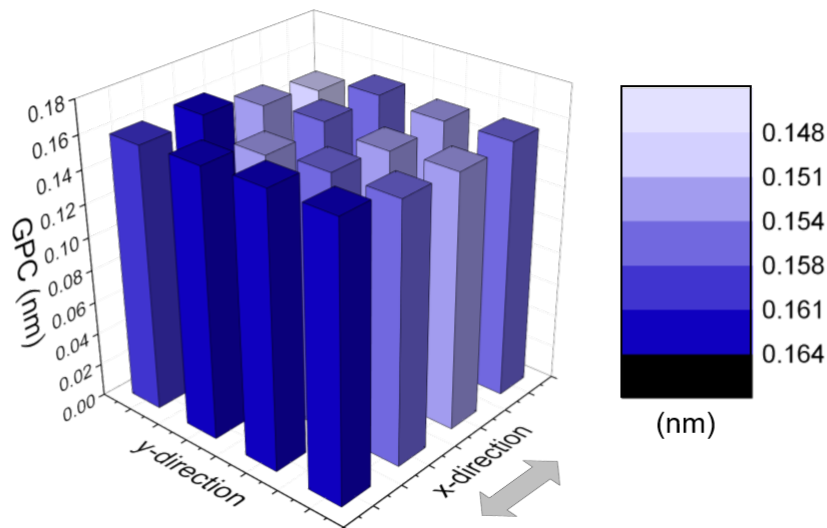
Figure 4.8.: Distribution of the Al_2O_3 film thickness in the $70\times70\,\text{mm}^2$ substrate inlet spatial ALD. Depicted is a TMA/plasma process deposited at 75°C at a substrate speed of v = $17\,\text{mm/s}$ on glas.

Actually, the root mean square deviation is smaller than $0.01\,\text{nm}$. Indeed, a slight decrease in film thickness could be observed in x-direction, but the deviation still fall below the error of measurement in a mechanical profilometer. Higher GPCs also could be explained by the proximity to waiter-containing environment of the glovebox since the substrate inlet gets close to left edge of the ALD head in the right-to-left movement in the ALD cycle. Here, experiments have shown that the glove box atmosphere even with a water content of less than $1\,\text{ppm}$ provides enough residual water to lead to full surface coverage in an (secondary) parasitic TMA/H_2O reaction, shown in Figure 4.9. Here the regime of substrate movement is chosen to be between the TMA inlet and the glove box environment, schematically depicted in Figure 4.9b. Thus a TMA/water reaction takes place when the substrate is leaving the inner part of the ALD head. Note, this is not a fundamental limitation of spatial ALD, but it rather is a specific limitation of the spatial ALD system used in this work, that needs to be taken into account. Assuming an Al_2O_3 density of $2.6\,\text{gcm}^{-3}$ (see Table 4.2) and a cubic volume, there is $140\,\text{ng}$ in one cubicnanometer of Al_2O_3. Taken the reaction equation for $1\,\text{mol}$ Al_2O_3 ($72\,\text{g}$ TMA + $54\,\text{g}$ H_2O = $102\,\text{g}$ Al_2O_3), it could be assumed that $0.7\,\text{g}$ is necessary to deposit one nanometer of Al_2O_3 on a area of $1\,\text{cm}^3$. This corresponds to $3.9\,\text{nmol}$ and $87\,\text{nl}$ H_2O, considering the ideal gas volume ($1\,\text{mol}$ = $22.4\,\text{l}$). These values can be present in the gas

Figure 4.9.: Secondary (parasitic) TMA/H$_2$O reaction caused by the glove box atmosphere: Depicted is the (linear) dependency of ALD cycles and Al$_2$O$_3$ film thickness. The process is operated with TMA and a extended substrate regime, moving the substrate (speed v= 17 mm/s) between TMA and the glove box environment. The water-containing atmoshphere lead to a H$_2$O caused oxidation step of the TMA saturated surface.

volume above the substrate table even if the water concentration is below 1 ppm, which is the lower detection limit of the water sensor, monitoring the environment of the glove box. Therefore, the contact between the glove box environment and the substrate has to be ruled out to avoid this (secondary) parasitic TMA/H$_2$O reaction. Due to this, in all further investigation the substrate movement was limited to the region underneath the substrate head. To this end the bottom side of the ALD head has been redesigned and the left/right side of the head has been extended appropriately.

The linearity of the ALD process as well as its dependency on temperature is shown in Figure 4.10. The plasma-based process shows a linear increase of the film thickness vs. number of cycles with a constant GPC of (0.17±0.02) nm at 75°C deposition temperature. For water-based processes a similar dependence could be found with the choice of 4 sccm N$_2$ through the water bubbler. In addition, temperature dependence is shown in Figure 4.10b. Here, it could be shown that the higher the deposition temperature, the lower the (saturated) GPC. At 150°C substrate temperature the film growth saturates at a GPC of (0.11±0.02) nm. A similar trend could be observed for the low pressure plasma (batch-based) ALD process. Here, the GPC decreases from 0.18 nm at 75°C to 0.10 nm at 150°C. The general decrease of the GPC towards higher depositon temperatures can be explained by the increase in film density with higher deposition temperature. The density of APP ALD-based Al$_2$O$_3$ increase from 2.5 gcm^{-3} at 75°C to 2.8 gcm^{-3} at 150°C. In

Figure 4.10.: Al$_2$O$_3$ growth in the spatial AP-ALD: Linearity of the film thickness in dependency of the numbers of cycles for plasma (v = 17 mm/s) and water-based (v = 34 mm/s, N$_2$(H$_2$O) = 4 sccm) processes (a) and the temperature dependency of the TMA/-plasma process, also compared to the low pressure ALD process (LP)(b). Based on ref.[2]

the same manner, the amount amount of impurities as carbon decrease towards higher deposition temperatures, as also reported for low pressure processes.[62] Both phenomena also could be seen in Table 4.2 and are discussed in more detail in the following paragraph.

4.2.2 Barrier properties

In Figure 4.11 Al$_2$O$_3$ barrier properties are presented. Figure 4.11a and Figure 4.11b shows the optical transmission and the WVTR vs. storage temperature of 100 nm Al$_2$O$_3$ deposited in a TMA/plasma process at 75°C deposition temperature. The relative humidity was kept constant at 60%r.H. during the experiment. The time-dependent optical transmission reveals that enhancing the storage temperature leads to an elevated diffusion of water molecules, resulting in an increase of the reaction speed of calcium to calcium hydroxide and therefore to an increase change in optical transmission as already discussed in subsection 2.2.2. Nevertheless, at 60°C/60% rH, a WVTR of 7×10^{-4} gm^{-2}d^{-1} is determined. By re-plotting the resulting WVTR in dependency on the storage temperature, the exponential (Arrhenius) behaviour becomes obvious (represented by the linear increase on the logarithmic scale). From the data shown in Figure 4.11b an activation energy $E_A = (62 \pm 10)$ kJ/mol could be derived.
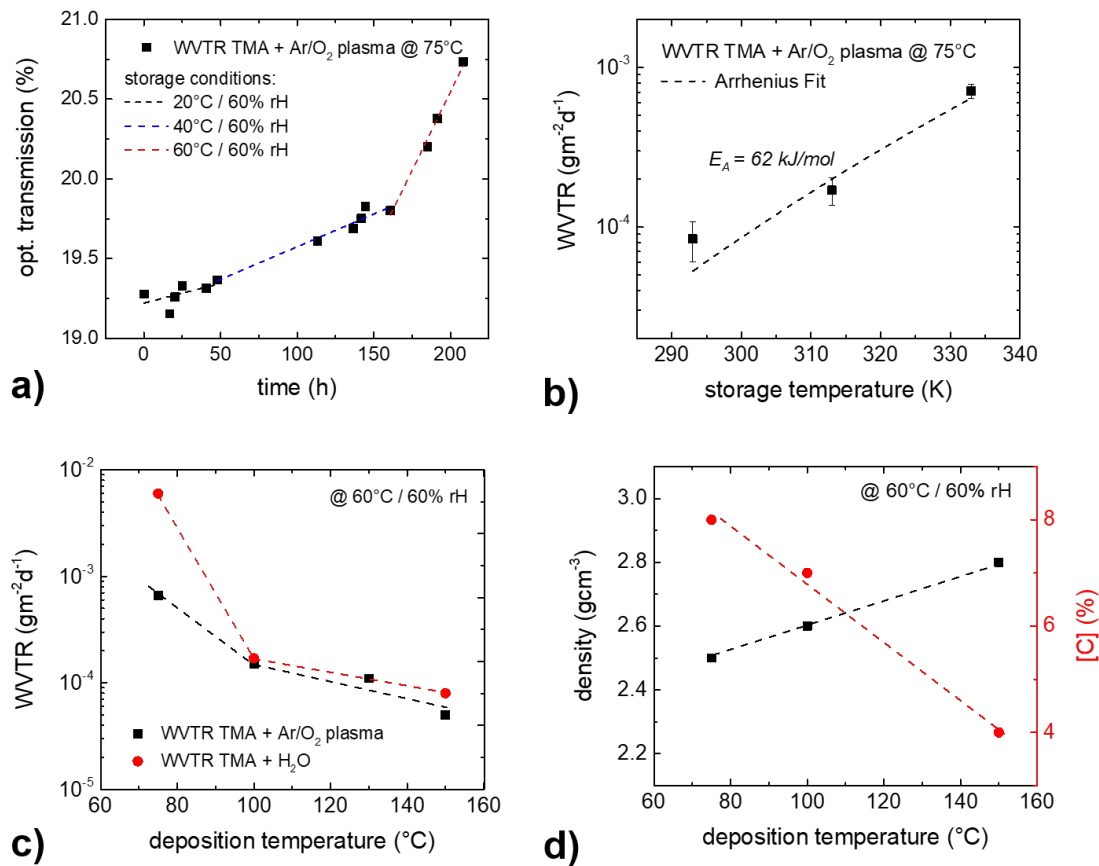
Figure 4.11.: Barrier properties of plasma-based Al$_2$O$_3$ deposited via SALD (grown at 75°C deposition temperature): a) Optical transmission vs. time. b) WVTR of in dependency of its storage conditions. WVTR (c) and film density as well as the concentration of carbon impurities (d) vs. ALD deposition temperature. Based on ref.[2]

Similiar values are found for the water-based analogues, which are on the same order as typically reported for alumina barrier layers deposited by low pressure ALD.[14,156] Since there is strong correlation of WVTR and layer density,[53] the WVTR was measured for layers grown at different substrate temperatures in a water- and plasma-based process (see Figure 4.11c). The WVTR is dominated by the intrinsic diffusion of water molecules through the material and the diffusion via defect states or impurities.

Table 4.2 summarizes the film properties for plasma- and water-based Al$_2$O$_3$. With increasing the deposition temperature film density and refractive index increase from n = 1.56-1.57 (75°C) to 1.64 (150°C), for both oxidants used. In the temperature regime APP ALD-based Al$_2$O$_3$ show densities between 2.5 - 2.8 gcm^{-3}. Note that the mass density of pure sapphire is reported to be 3.9 gcm^{-3}.[183] The increase of the mass density towards

higher deposition temperatures could also be found for low pressure analogues (2.7 - 3.1 gcm^{-3} between RT and 200°C[184,185]). In the same way, a similar amount of carbon impurities could be found in Al$_2$O$_3$ based on APP ALD and low pressure processes (e.g. [C] 1-6%[184]).

Table 4.2.: Film properties of Al$_2$O$_3$ deposited via spatial AP ALD: Oxygen-to-aluminium-ratio, carbon impurities, film density ρ (all measured by RBS), refractive index n (at 632 nm) and WVTR (measured at 60°C/60%r.H.)

	T (°C)	[O]/[Al]	[C] (%)	n	ρ (gcm^{-3}))	WVTR (gm^{-2}d^{-1})
Ar/O$_2$-Plasma	75	1.4	8	1.57	2.5 ± 0.3	7×10^{-4}
	100	1.7	7	1.58	2.6 ± 0.3	2×10^{-4}
	150	1.6	4	1.64	2.8 ± 0.3	5×10^{-5}
H$_2$O	75	1.5	1	1.56	2.5 ± 0.3	6×10^{-3}
	150	1.6	1	1.64	2.9 ± 0.3	8×10^{-5}

The stochiometry of [O]/[Al] indentifies the deposited aluminium oxide as Al$_2$O$_3$, with slighly higher amount of oxygen at higher deposition temperatures. Concluding all film properties, a strong correlation between the WVTR and the intrinsic density as well as the concentration of carbon impurities can be found. Due to carbonates and -HCOO groups along with the -OH groups as dominating reactive surface species in plasma-based ALD processes,[182,186] there is still 4% of carbon in the Al$_2$O$_3$ thin films even at 150 °C deposition temperature. Even with this amount of carbon and a density of 2.8 gcm^{-3} for plasma-based Al$_2$O$_3$ a WVTR of 5×10^{-5} gm^{-2}d^{-1} could be observed at 60°C and 60% r.H. Similar WVTR could be found for the water-based analogues at high deposition temperature (8×10^{-5} gm^{-2}d^{-1} at 150°). As the H$_2$O + TMA process is based on -OH surface groups this process is known to lead to almost carbon-free alumina films (1%),[186,187] indicating that the amount of carbon impurities has negligible influence on the barrier properties of those films. Low temperature water-based Al$_2$O$_3$ only show 6×10^{-3} gm^{-2}d^{-1}. This can be explained by the fact that the water-based TMA process at 75°C did not fulfill ALD characteristics. Even when the density in water-based alumina films is similar to their plasma equivalents (compare Table 4.2), it could be assumed that not-saturated film growth results in the formation of a increasing number of diffusion paths.

These values measured for spatial ALD based Al$_2$O$_3$ are comparable to those, deposited in the batch ALD system as discussed in section 4.1 as well as to those, reported in literature.[175] Using the activation energy of E_A = (62 $\pm$ 10) kJ/mol (as determined above), the WVTR for plasma-based high temperature Al$_2$O$_3$ could be calculated to be

4×10^{-6} gm^{-2}d^{-1} at room temperature. Furthermore, spatial ALD based Al$_2$O$_3$ is used in polymer/metal oxide multilayer encapsulations, heavily improving the integral WVTR, see section A.2.

Summary: In this chapter, batch-based and spatial plasma ALD of Al$_2$O$_3$ thin films at atmospheric pressure is achieved, leading to gas diffusion barriers with WVTRs in the range of 10^{-5}-10^{-6} gm^{-2}d^{-1} similar to layers deposited by vacuum based ALD. In addition, the high sticking coefficient of water as oxidant in atmospheric pressure low temperature ALD processes could be highlighted. In sharp contrast, plasma as oxidant enables the continuous deposition of GBDs at atmospheric pressure and low temperatures

5

SnO$_x$-based gas diffusion barriers by spatial atmospheric pressure ALD

In general, SnO$_x$ thin films could be deposited using different systems of precursors. Most common Sn-precursors are tin chloride (SnCl$_4$)[188][189] or tin iodide (SnI$_4$),[190] but also Tetrakis(dimethylamino)tin (TDMASn), Acetylacetonate tin (Sn(acac)$_2$) or Dibutyl-tindiacetate (DBTA) are frequently used to deposited tin oxide[191] via ALD. In this work, tin oxide thin films were fabricated using Tetrakis(dimethylamino)tin (99.99%, *Strem Chemicals*) and different oxidants (water, Ar/O$_2$ plasma and ozone). In the Tetrakis-(dimethylamino)tin molecule the central tin atom is coordinated by four dimethylamine groups.

In this chapter, the growth of tin oxide as transparent electrically conductive gas diffusion barrier is investigated and the resulting film properties are compared to those of low-pressure ALD based SnO$_x$. The dependence of GPC and layer properties on growth temperature are analyzed. Afterwards the electrical conductivity as well as its barrier properties are presented in more detail. Finally, its use in perovskite solar cells as conductive gas diffusion barrier is demonstrated. Once again, it has to be mentioned, that the discussion on substrate speed is excluded and presented individually in chapter 6. Unless otherwise stated, all SnO$_x$ thin films presented in this chapter were grown with a with a moderate substrate speed v = 20 mm/s.

5.1 SnO$_x$ growth

In order to confirm ALD growth, the self-limiting nature of the process has to be verified. Figure 5.1 shows the saturation of each precursor for different TDMASn ALD processes. The TDMASn precursor was kept in a precursor bubbler in the glove box without external heating. Note that precursor temperature is influenced by the ambient conditions e.g. the glove box temperature which is strongly dependent on the heat loss of the ALD system (at higher deposition temperatures). The bubbler temperature could be estimated between 25°C and 40°C.

Figure 5.1a and Figure 5.1b demonstrate the plasma-based process, while Figure 5.1c and Figure 5.1d depict the water-based and the ozone-based ALD saturation behavior for 100°C and 150°C deposition temperature, respectively.
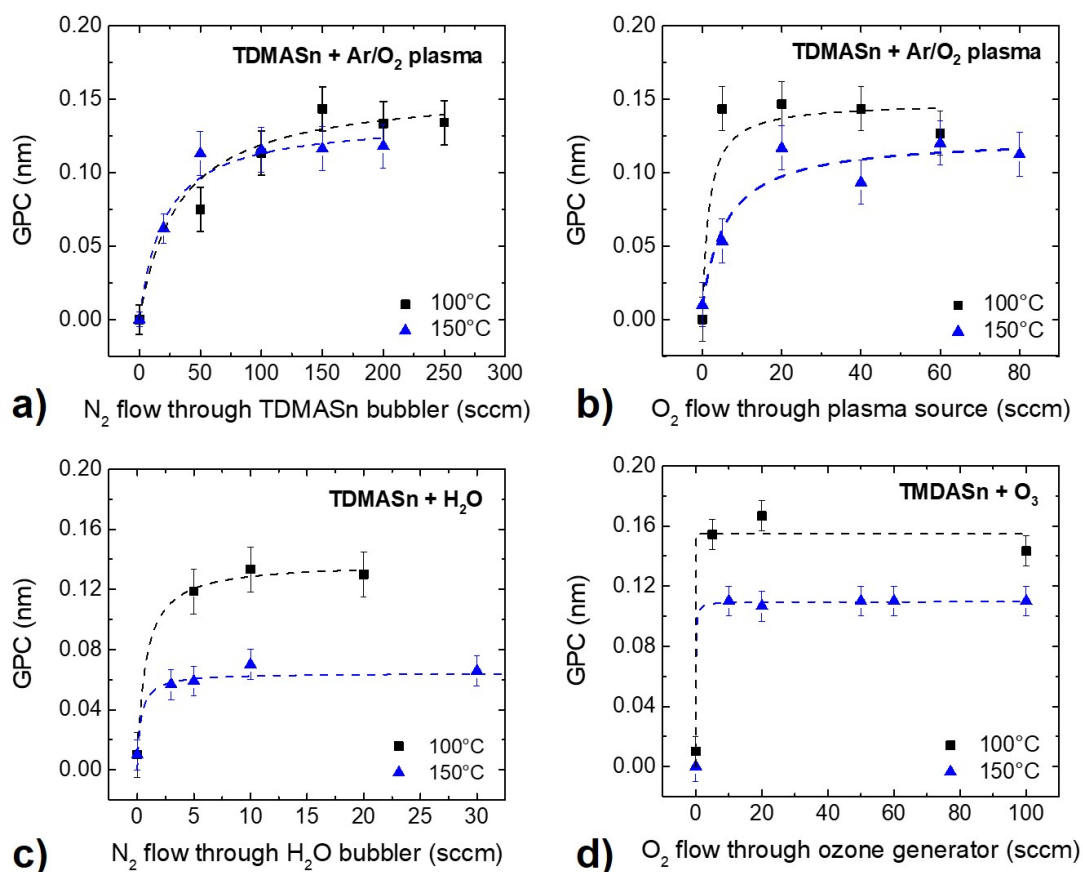
Figure 5.1.: Saturation behaviour of the TDMASn-based ALD processes for different oxidants: Plasma (a,b), H$_2$O (c) and ozone (d) at 100°C and 150°C deposition temperature. Plasma and ozone dose are represented by the amount of O$_2$ used in the process. The respective other precursor is chosen in its saturation regime. Based on ref.[3]

Self-limiting characteristics for all oxidants are found for both 100°C and 150°C deposition temperature. In the plasma- and ozone-based process an average GPC of (0.15 ± 0.02) nm at 100°C and (0.11 ± 0.02) nm at 150°C could be found. Here, a flow of 150 sccm of N$_2$ through the TDMASn bubbler provides full surface coverage leading to a saturated GPC. On the other hand, a flow of 20 sccm of O$_2$ in the Ar plasma is sufficient for the saturated GPC. Note that the amount of ozone generated in Figure 5.1d relates to an ozone concentration between 10^2-10^3 ppm. For more details on the generated ozone concentration see subsection 3.4.1.

Water-based ALD shows similar GPC at 100°C, but lower GPC at 150°C (0.07 ± 0.02) nm. As already seen for Al$_2$O$_3$ thin films, even a tiny flow of N$_2$ through the water bubbler is already sufficient to afford full surface coverage (5 sccm of N$_2$ for both deposition temperatures). The substantially smaller GPC of the water-based process at higher deposition temperature can be attributed to the lower reactivity of H$_2$O compared to oxidants like ozone etc. at higher temperatures, already reported in literature.[51,192] For example, a GPC of 0.06 nm at 175°C is reported for TDMASn/water ALD.[193] In addition higher GPCs of tin oxide for H$_2$O$_2$ as oxidant are demonstrated, attributed to e.g. a higher concentration of surface hydroxyl groups for H$_2$O$_2$ as oxidant.[193]
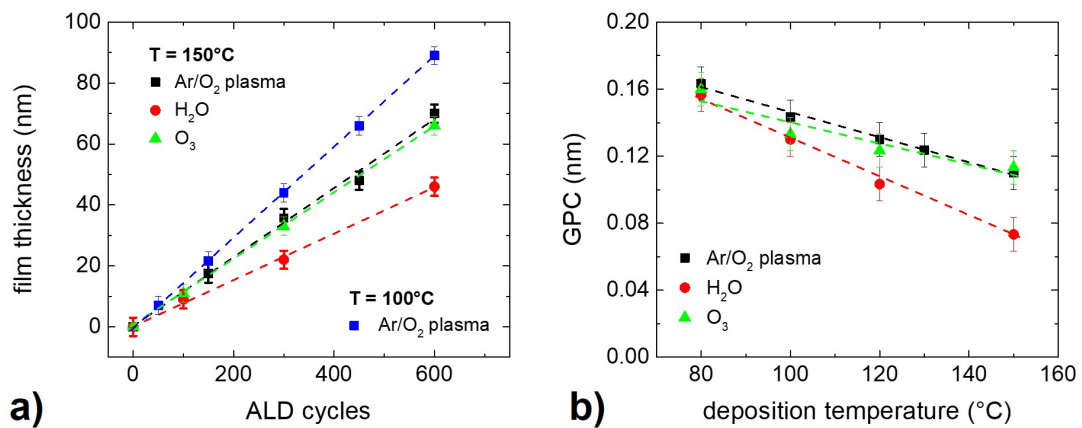
Figure 5.2.: Dependency on ALD cylces (a) and deposition temperature (b) of TDMASn-based S-ALD processes for plasma, H$_2$O and ozone as oxidants (at v = 20mm/s).Based on ref.[3]

In general, the observed GPCs for plasma-, ozone- and water-based processes are in the same range as those reported for low pressure ALD, e.g. for low-pressure plasma based ALD SnO$_x$ at 100°C (GPC = 0.17 nm[194]) and for ozone-based SnO$_x$ at 150°C (GPC = 0.08 nm[195]). As already seen for the TMA/water process at atmospheric pressure, there is also a difference in GPC for the water-based process e.g. for 80°C a GPC 0.15 nm at

atmoshperic pressure vs. 0.11 nm at low-pressure (approx. 1 mbar). The higher GPCs of atmospheric pressure ALD at low temperature vs. classical vacuum based ALD have been found before for other precursor systems, e.g. Al$_2$O$_3$[134] (see section 4.1[1] and section 4.2[2]). The phenomenon of higher GPCs has been attributed, on the one hand, to a lower mass density of metal oxides deposited at atmospheric pressure ALD and, on the other hand, to the excess of adsorbed water, leading to an additional CVD type of growth.[134] Linear dependency of SnO$_x$ film thickness on the number of ALD cycles is demonstrated in Figure 5.2a with the GPC values already mentioned above for plasma, ozone and water as precursor. Linked with the saturation shown above, all ALD characteristics for the TMDASn precursor system are given. The temperature dependency of the GPC is shown in Figure 5.2b. In general, a linear decrease in GPC could be observed for all oxidants used in the temperature regime between 80°C and 150°C deposition temperature. Nevertheless, while plasma- and ozone-based SnO$_x$ have similiar GPCs at all investigated temperatures, water-based GPC dramatically decrease towards higher deposition temperature due to the reasons already mentioned above. This difference in growth behavior also has huge effects on its thin film properties, addressed in the following paragraph.

5.2 SnO$_x$ film properties

Tin oxide deposited by S-ALD at atmospheric pressure shows remarkably similar film properties as its low-pressure analogues. Here, tin oxide from TDMASn and water at 80°C deposition temperature is taken as an example, see Table 5.1. The low-pressure equivalents are deposited in a commercial batch-based ALD system at 1 mbar process pressure (*Beneq TFS 200*).

Table 5.1.: Film properties of SnO$_x$ from TDMASn + H$_2$O processes by spatial atmospheric pressure ALD compared to the low-pressure (batch-based) counterparts deposited in a commercial batch-based reactor. Deposition temperature 80°C (v = 20 mm/s)

	S-AP-ALD	B-LP-ALD
GPC (nm)	0.15	0.11
n	1.88	1.89
Optical bandgap (eV)	3.8	3.8
Electrical conductivity (Scm^{-1})	10^{-4}	10^{-4}
WVTR (gm^{-2}d^{-1})	2×10^{-4}	4×10^{-4}

As already discussed above, spatial ALD (at atmospheric pressure) yields a somewhat higher GPC compared to conventional batch ALD. From RBS measurements a mass density for S-ALD based SnO$_x$ could be estimated to (4.9 ± 0.3) gcm^{-3} (at 100°C deposition temperature), while its low-pressure counterparts show a density of 5.4 gcm^{-3} (at 100°C deposition temperature). These findings underline the hypothesis that the slightly higher GPC resulting in atmospheric pressure processes are due to a to lower mass density. Surprisingly, this difference in mass density has only a slight impact on the refractive index (n = 1.88 vs. 1.89) and on the barrier properties $(2 \times 10^{-4}$ vs. 4×10^{-4} gm^{-2}d^{-1}), which will be discussed in more details in subsection 5.2.2. Both processes lead to similar electrical conductivity (10^{-4} Scm^{-1}) as well as optical band gap.
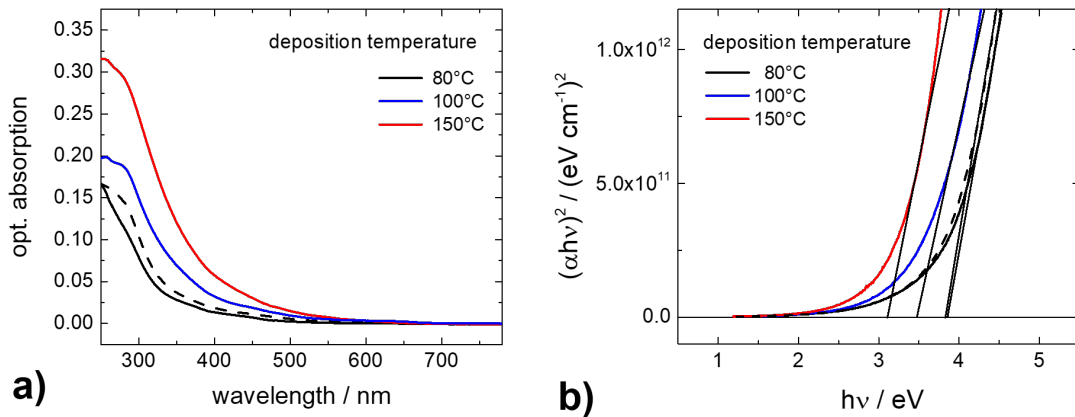
Figure 5.3.: Optical absorption spectra (a) and the respective tauc plots (b) of 20 nm thin films of SnO$_x$ deposited by spatial atmospheric pressure and ALD (solid lines) and batch-based low pressure ALD (dashed lines) at varied process temperature. Based on ref.[3]

The optical band-gap is determined from the respective Tauc-plots, assuming an direct optical transition for the determination of the band gap. The absorption coefficient was determined via $\alpha = 4 \pi k / \lambda$, with the extinction coefficient k (measured via MIR ellipsometry) and the wavelength λ.[51,201] A band gap of 3.8 eV was derived for SnO$_x$ deposited by both S-ALD and B-ALD at 80°C, see Figure 5.3. With increasing deposition temperature the band gap is decreasing to 3.5 eV, 3.3 eV and 3.2 eV and 100°C, 120°C and 150°C, respectively. In addition, a notable sub-band-gap absorption could be found. A similar trend has already been found for low pressure SnO$_x$ layers in batch-based ALD.[192] The decreasing bad-gap has been attributed to an increased density of subgap defects related to oxygen deficiency. In the same way, the density and the re-

fractive index of tin oxide thin films increase with increasing deposition temperature, shown in Figure 5.4 and compared to those values reported in literature ([192,193,195,196]).
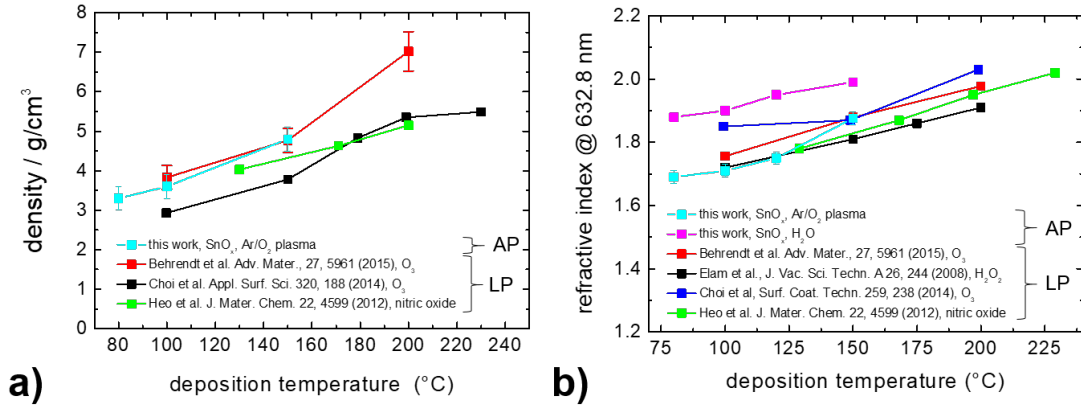
Figure 5.4.: Density (a) and refractive index (b) of SnO$_x$ thin films vs. ALD deposition temperature for different oxidants. Our data is compared to this reported in the literature which are all based on low pressure ALD processes. Data taken from ref.[4,192,193,195,196]

Good agreement can be found for plasma- and ozone based films for film density as well as refractive index, independently on the ALD process pressure. On the other hand water based spatial ALD based SnO$_x$ thin films tend to higher refractive indices as their low-pressure analogues (which even exceeds those of bulk SnO$_2$), attributed to the formation of tin monoxide (SnO).
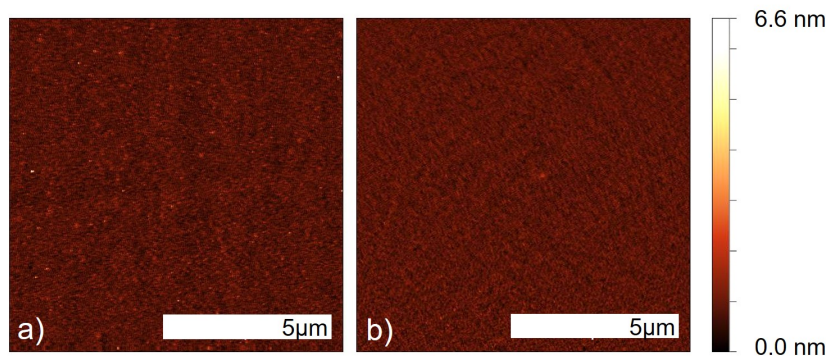
Figure 5.5.: AFM Measurement of 300 cycles of SnO$_x$ deposited by plasma enhanced spatial ALD at 100°C (thickness: 34nm) (a) , RMS = 0.35 nm and at 150°C (thickness: 42nm), RMS = 0.21 nm (b). Based on ref.[3]

In addition, atomic force microscopy reveals (Figure 5.5) a similar surface morphology for 100°C and 150°C deposition temperature, respectively.

5.2.1 Electrical conductivity

The electrical properties of SnO$_x$ deposited from TDMASn and different oxidants at a varied growth temperature are shown in Figure 5.6.
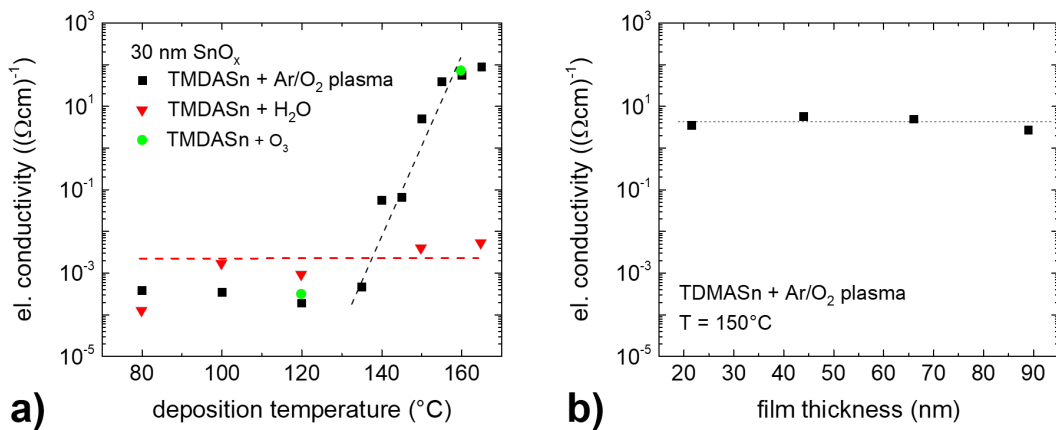
Figure 5.6.: Electrical conductivity of SnO$_x$ thin films in depedence of deposition temperature for different co-reactants (a) and different film thicknesses (b). Based on ref.[3]

Obviously, for the plasma-based films, the electrical conductivity starts to increase significantly from 10^{-1} $(\Omega\text{cm})^{-1}$ (at 135°C) up to 100 $(\Omega\text{cm})^{-1}$ at higher deposition temperatures (165°C). A similar trend could be found for ozone based SnO$_x$ (70 $(\Omega\text{cm})^{-1}$ for 160°C). For water-based processes an average conductivity of 2.3×10^{-3} $(\Omega\text{cm})^{-1}$ was found, that did not show a strong temperature dependence. Note that the error bars for the conductivity of water-based SnO$_x$ are on the order of 10^{-3} $(\Omega\,\text{cm})^{-1}$ due to low maximum currents at low electrical conductivities. These findings on the strong dependency on oxidants are in agreement with our earlier results of SnO$_x$ prepared by vacuum-based batch ALD.[195] The increased electrical conductivity of SnO$_x$ has been attributed to the incorporation of hydrogen in the tin oxide.[197,198] The interstitial hydrogen in the form of OH-species acts as a shallow donor and causes n-type conductivity[199] which is as direct result strongly dependent on this oxygen-hydrogen bond. However, a lower amount of oxygen inside the tin oxide film (e.g. [O]/[Sn] < 2) only leads to very low electrical conductivities represented by the missing O-H bond. Furthermore, the increase of the electron mobility towards higher deposition temperatures causes higher electrical conductivities.[78] However, the electron mobility of water-based SnO$_x$ could

not be determined due to the low electrical conductivity. The low [O]/[Sn] ratio for water-based SnO$_x$ also becomes evident in the optical properties of SnO$_x$, by evaluating the respective Tauc-plots (see inset in Figure 5.7).
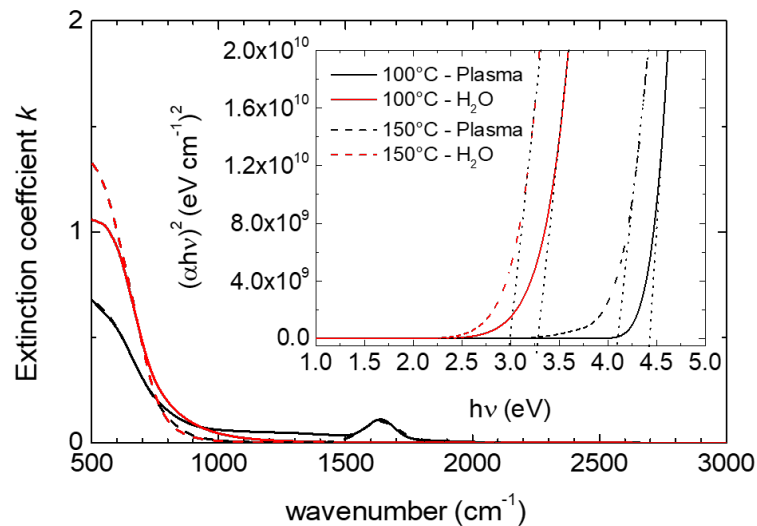
Figure 5.7.: Extinction coefficient k in the IR spectral range measured by MIR ellipsometry. Atmospheric pressure SnO$_x$ grown with plasma and water based processes at 100 and 150°C are depicted, respectively. The band-gap energy (E_g) has been determined from the respective Tauc plots (inset). A characteristic signal related to C-O stretch vibrations can be found (at 1650 cm^{-1}) for plasma based SnO$_x$. Based on ref.[3]

Here the sub-gap absorption and the relatively small band gap (3.0 - 3.3 eV) hints to the presence of SnO instead of SnO$_2$.[200] The energy gap for plasma-based SnO$_x$ could be estimated to 4.1 eV for thin films deposited at 150°C process temperature and 4.4 eV for 100°C. Therefore, the energy gap decreases with increasing deposition temperature for plasma- and H$_2$O-based spatial ALD, as found in literature for vacuum-based ALD of SnO$_x$ thin films.[51,195,201] Even if this phenomenon is not fully understood yet, it has been attributed to possible quantum confinement effects in SnO$_x$ grains with a size below 3 nm, depending on growth temperature.[51] However, these grain sizes (with lateral dimensions in this range) are too small to be detected in our x-ray diffraction setup (via XRD).

In addition to the low [O]/[Sn], impurities like carbon or nitrogen can hinder the electron transport by forming e.g. carbon-oxygen bonds.[202] While water-based ALD-SnO$_x$ show [O]/[Sn] < 2 at all deposition temperatures, plasma- and ozone-based SnO$_x$ (deposited at 100°C) reveal [O]/[Sn] ratios of 2.1 - 2.2. In addition, SnO$_x$ films deposited

by plasma- or ozone-based processes show high amounts of carbon and nitrogen (4-12%) (as residuals of the tin oxide precursor). The presence of carbon also gets depicted by the characteristic signal (at 1650 cm^{-1}) in the MIR absorption spectra shown in Figure 5.7, which could be related to a C-O stretch vibration. With increasing deposition temperature the concentration of impurities is reduced, enabling the formation of electrical charge transport, see Table 5.2.

Table 5.2.: Film properties of 100 nm thick SnO$_x$ deposited by Spatial ALD: Oxygen-to-tin-ratio, carbon and nitrogen , refractive index n (measured at 632 nm) and density ρ). *-marked sample thickness: 20 nm

	T (°C)	[O]/[Sn]	[C] (%)	[N] (%)	n	ρ (gcm^{-3}))
Ar/O$_2$-Plasma	75	2.1	12	12	1.65	3.3 ± 0.3
	100	2.2	8	11	1.70	3.6 ± 0.3
	150	2.2	6	6	1.88	4.8 ± 0.3
O$_3$	150	2.2	4	4	1.88	5.5 ± 0.3
H$_2$O*	80	2.0	20	5	1.89	4.6 ± 0.3
H$_2$O	150	1.7	2	0	2.09	4.5 ± 0.3

For plasma-based tin oxide the amount of carbon decreases from 12% to 6% by increasing the deposition temperature from 75°C to 150°C. A similar trend could be observed for the nitrogen impurities (12% to 6% in the respective temperature regime). Water-based SnO$_x$ contains comparable (or even more) number of carbon atoms at low deposition temperature. Its amounts decreases analogous with increasing ALD process temperature. Nevertheless, the formation of electrical charge transport can still not be accomplished reasoned by the missing incorporation of hydrogen, represented the low [O]/[Sn] at 150°C deposition temperature.

5.2.2 Barrier properties

In the following, the barrier properties of tin oxide by spatial ALD with different sources of oxygen are investigated. Therefore, optical Ca-tests were performed with 100 nm thick tin oxide, respectively. Exemplary, Figure 5.6a) shows the optical transmission vs. time measured during the optical Ca-test for a plasma-based tin oxide barrier. Due to the change in the optical transmission (from 9.2 to 10.2% in 90 hours), 100 nm SnO$_x$ based on Ar/O$_2$ plasma show a WVTR of 7×10^{-4} gm^{-2}d^{-1} at 60°C/60% rH. Compara-

ble tin oxide films were used to measure the electrical conductivity, see Figure 5.6b). The electrical conductivity remains essentially unaltered even after 8000 h under damp heat conditions (also at 60°C / 60% rH). Indeed, the carrier density increases slightly from 1.1 to 3.1 × 10^{20} cm^{-3} while the electron mobility decreases from 4.7 to 2.8 cm^{2}V^{-1}s^{-1}. It could be assumed that under elevated humidity OH-bonds are formed in the tin oxide layers, which act as shallow dopands and thereby increase the carrier density. The somewhat lower electron mobility could be explained by the slight degradation of material quality. However, plasma-based SnO$_x$ shows sufficient barrier properties (WVTR ≈ 10^{-4} gm^{-2}d^{-1}) as well as stable electrical conductivity, even at damp heat conditions. Furthermore, barrier properties of SnO$_x$ deposited with different oxidants will be discussed.
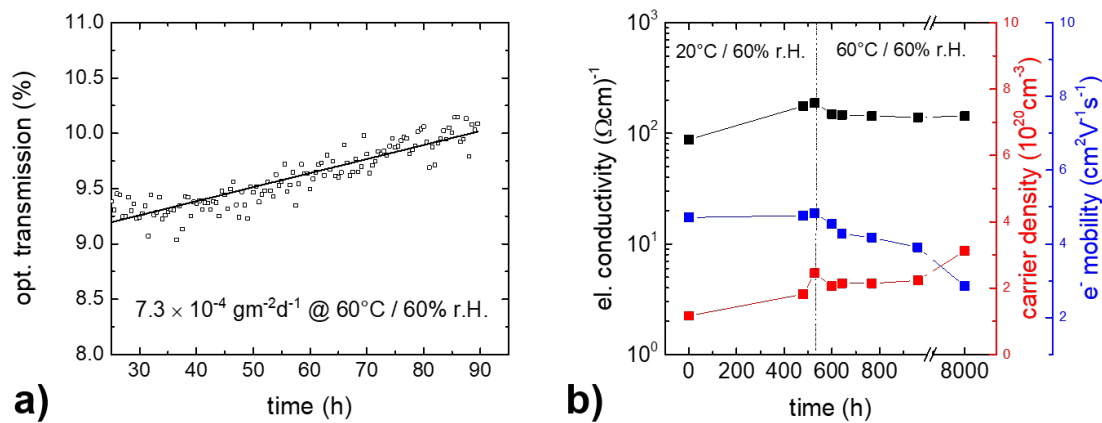
Figure 5.8.: (a) Optical transmission of a 100 nm thick calcium sensor encapsulated with 100 nm plasma-based SnO$_x$ over time (stored at 60°C/60% rH). (b) Dependency of the electrical properties of plasma-based tin oxide over time at 60°C/60% rH. Deposition temperature was set to 150°C for both measurements shown. Based on ref.[3]

While Figure 5.8 shows the stability of SnO$_x$ deposited by (spatial) plasma ALD, Figure 5.9 summarizes the barrier properties of SnO$_x$ deposited not only with plasma but also with water- and ozone-based spatial ALD. Obviously, like already seen for Al$_2$O$_3$ barriers, the WVTR decreases with increasing deposition temperatures due to an increasing film density and a lowered amount of residuals (compare Table 5.2).

Water-based SnO$_x$ deposited at 80°C (by spatial ALD) shows a WVTR of 2 × 10^{-4} gm^{-2}d^{-1} at 60°C/60% rH. A deposition temperature of 150°C leads to SnO$_x$ with a WVTR of 1 × 10^{-5} gm^{-2}d^{-1} at 60°C/60% rH, similar to those for SnO$_x$ deposited by low pressure ALD (3 × 10^{-5} gm^{-2}d^{-1} at 70°C/70% rH.[195]). In addition, water-based SnO$_x$ reveals significantly lower WVTR than their plasma- and ozone equivalents. The WVTR of
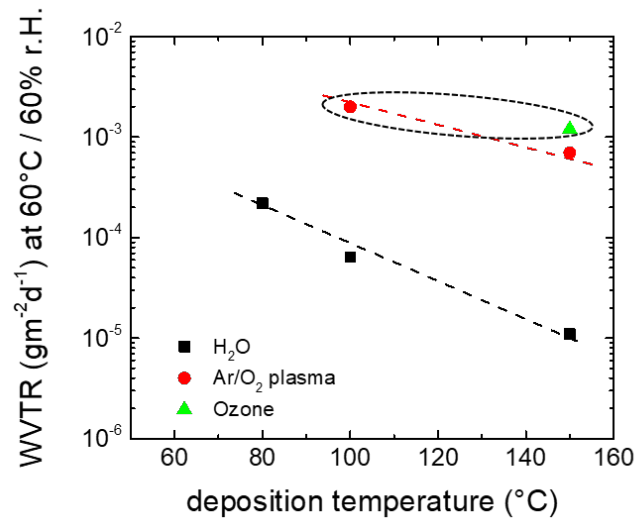
Figure 5.9.: Comparision of the WVTR (at 60°C/60% rH) of tin oxide based on plasma, water and ozone as co-reactant. All data were measured via the optical Ca-test. Data, marked with the dotted line, were measured at 40°C/60% rH.

plasma-based SnO$_x$ deposited at 150°C remains at 7×10^{-4} gm^{-2}d^{-1} (at 60°C/60% rH). 100°C deposition temperature for plasma-based thin films also leads to an increase of the WVTR (2×10^{-3} gm^{-2}d^{-1} (at 40°C/60% rH)). The ozone-based process lead to comparable WVTR (1×10^{-3} gm^{-2}d^{-1} at 40°C/60% rH) with 150°C deposition temperature. The different storage conditions were chosen due to the destruction of the calcium sensor at the standard testing conditions in this work (60°C/60% rH). Generally, the WVTRs of those films are even higher at standard testing conditions (60°C/60% rH) than at 40°C/60% rH.

All in all, these findings underline similar growth behaviour of plasma- and ozone-based SnO$_x$. Plasma- and ozone-based ALD lead to WVTRs which are roughly one order of magnitude higher than that of their water-based analogues. The difference in film stoichiometry and the residuals left in the films suggest that those are reasons for the higher WVTR values. On contrast, water-based low temperature SnO$_x$ show surprisingly good barrier properties despite a high amount of carbon impurities. Therefore, a higher oxygen-to-tin ratio seems to lead to inferior barriers, as the -OH groups could work as diffusion paths for water molecules. The WVTRs reported for water-based spatial ALD SnO$_x$ thin films are even comparable to those reported for ALD grown Al$_2$O$_3$.

5.3 Application of electrically conductive barriers in perovskite solar cells

In the following, the use of SnO$_x$ as electron extraction layer as well as gas diffusion barrier in perovskite solar cells will be discussed. Brinkmann et al. had already shown the principal functionality of ALD grown SnO$_x$ in perovskite solar cells, but were still restricted by the use of low pressure batch ALD.[74] Here, the use of tin oxide by spatial ALD at atmospheric pressure in perovskite solar cells will be shown, enabling the roll-to-roll fabrication of long-term (heat and moisture) stable perovskite solar cells. As water-based SnO$_x$ shows superior barrier properties along with sufficient electrical conductivity (in vertical direction through e.g. 20 nm SnO$_x$), it is used in all systems shown in this chapter. In addition, the functionality of tin oxide and its dependence on its precursor system in low-pressure ALD is already shown by Brinkmann et al. and Hu et al. (see Ref.[74,203]). Nevertheless, this work concentrates on single SnO$_x$-based diffusion barriers deposited by spatial ALD for inverted PSCs. The damage of plasma species on the perovskite material is strongly dependent on the perovskite stability, which is not studied in this thesis.

5.3.1 Fabrication of perovskite solar cells

The inverted perovskite solar cells (p-i-n PSCs) are based on a glass/ITO/PEDOT:PSS/CH$_3$NH$_3$PbI$_3$/PCBM/AZO/SnO$_x$/Ag sequence (see Figure 5.10a). Here, PEDOT:PSS serves as an hole transport material while CH$_3$NH$_3$PbI$_3$ is the active perovskite material. PCBM and a layer of AZO nano particles with a particle size of 12-18 nm function as electron extraction layer which is encapsulated by the SnO$_x$ layer. The AZO layer was spin coated at 60 s at 8000 rpm, 2.5 wt% in isopropanol (prod. no. 8045, Avantama AG, Switzerland)(layer thickness = 100 nm). ITO as well as the Ag serve as electrode, respectively. With the commercial CH$_3$NH$_3$PbI$_3$-Ink (Ossilla) solar cells with efficiencies around 11-13% are possible. Here, the efficiencies are not limited by use extraction layer. For example, LiF/Ag (as commonly used low workfunction extraction layer) on the commercial CH$_3$NH$_3$PbI$_3$ lead to similar (low) PCE, but its efficiencies degraded to <50% of the initial value within less than a day in ambient air.[74] The perovskite solar cells were encapsulated with 20 nm SnO$_x$ from TDMASn and water at 80°C with a moderate (standard) substrate speed of v = 20 mm/s. The saturation behavior of the spatial ALD growth process is shown in Figure 5.10b and Figure 5.10c.
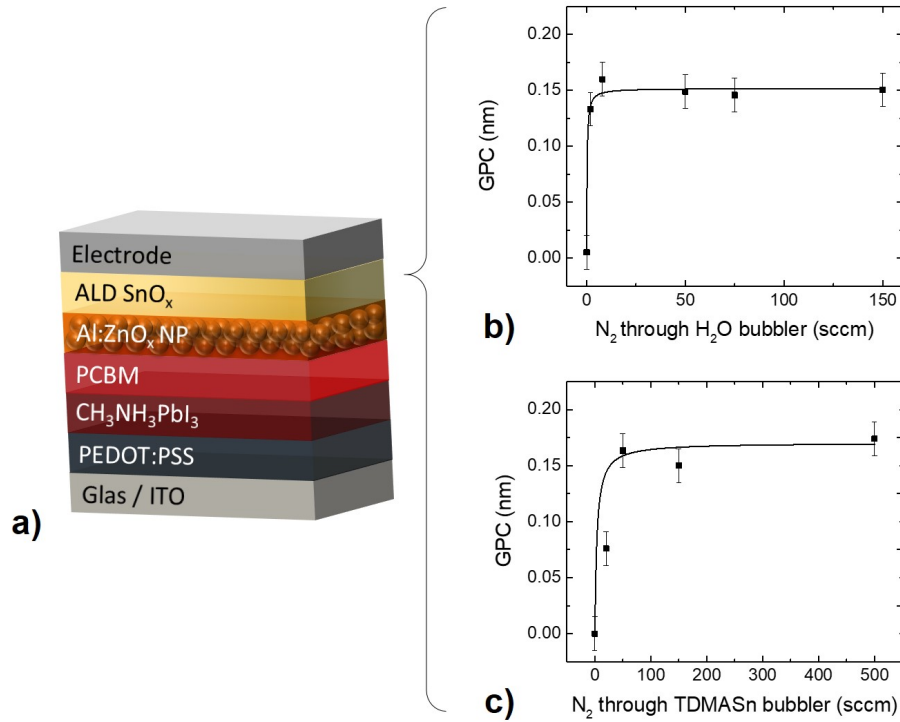
Figure 5.10.: Perovskite solar cell stack based on a glass/ITO/PEDOT:PSS/ $CH_3NH_3PbI_3$/PCBM/AZO/SnO$_x$/Ag sequence (a) and SnO$_x$ growth at 80°C for the encapsulation of perovskite solar cells: b) Variation of the N$_2$ flow trough the H$_2$O bubbler (N$_2$(TDMASn) = 150 sccm). c) GPC vs. N$_2$ flow trough the TDMASn bubbler (N$_2$(H$_2$O) = 8 sccm). Based on ref.[4]

5.3.2 Characterization of perovskite solar cells

Perovskite solar cells were fabricated as described above. Resulting J/V-characterization, the power conversion efficiency at the maximum power point and solar cell stability (air and heat) is shown in Figure 5.11. Here, solar cells based on the spatial (atmospheric pressure) ALD-SnO$_x$ are compared to those incorporating the batch-based (low-pressure) ALD-SnO$_x$ (Beneq TF 200). Both sets of samples show a remarkable similarity in their cell (J/V-) characteristics. The corresponding PCE, FF, V_{OC} and J_{SC} are listed in Table 5.3. Note that all shown solar cells values are averaged over 15-18 solar cells. The statistical data is shown in section A.3. Both tin oxides afford PSCs with efficiencies around 11.2 - 12.7%. All absolute PCEs shown in this section are corrected to their external quantum efficiency (EQE), shown in Figure 5.12. The EQE is the ratio of the amount of charge carriers collected by the solar cell to the number of incident photons.
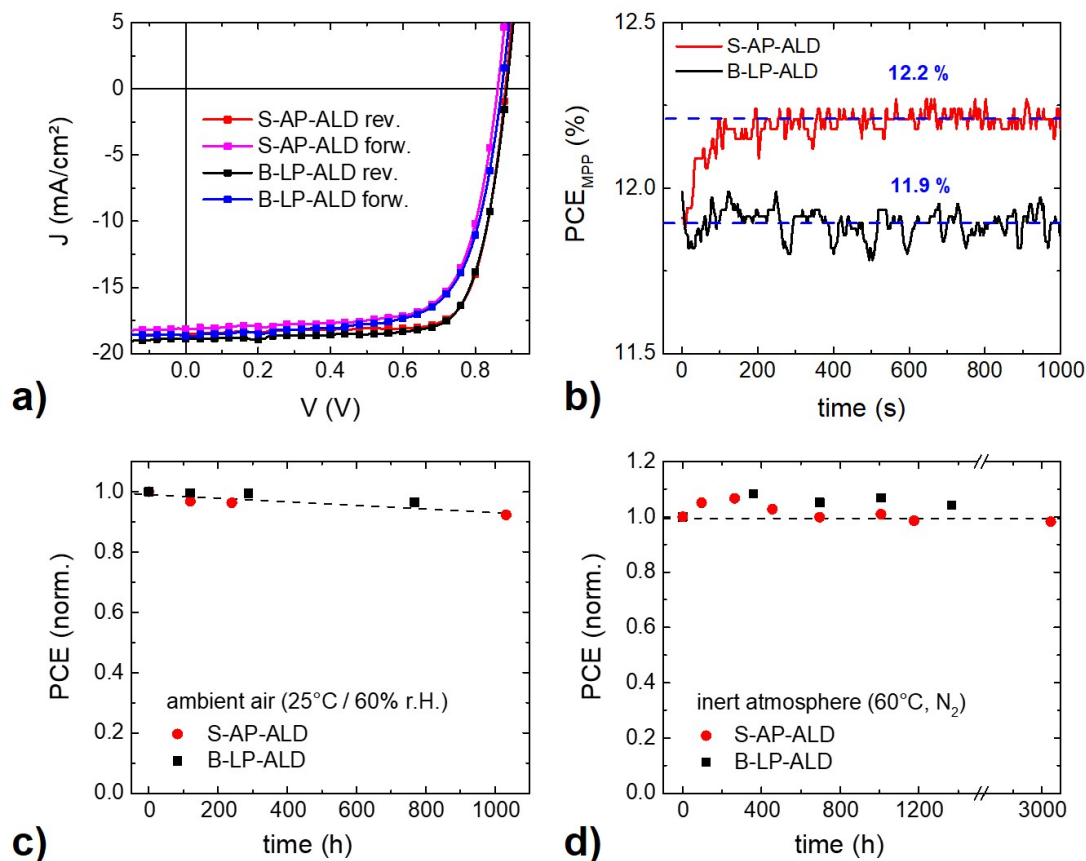
Figure 5.11.: Comparison of perovskite solar cells with SnO$_x$ barrier layer grown by S-ALD and B-ALD at 80°C deposition temperature. S-ALD SnO$_x$ was deposited at a moderate substrate velocity of 20 mm/s. J/V characteristics are depicted in Fig.(a) and stabilized power output in Fig. (b). All related current density data were derived from EQE measurements (see Figure 5.12). Mono stress tests are shown in (c) (PCE vs. time of storage in ambient air (25°C, 60% r.H.)) and (d) at elevated temperature (60°C, inert atmosphere). Based on ref.[4]

Remarkably, 20 nm of the ALD based SnO$_x$ encapsulation lead to a sufficient barrier against mono-stress conditions. While the efficiency of not-encapsulated perovskite solar cells would break down (<50% of the normalized PCE) in the first 100 h under ambient conditions (25°C / 60% r.H.) and within 200 h at elevated temperature (60°C, inert atmosphere) (see Ref.[74]), excellent long-term stability of PSCs based on SnO$_x$ grown by S-ALD is afforded under ambient air (25°C / 60% r.H.) and under elevated temperatures (60°C, inert atmosphere). The normalized PCEs show 92% of its initial value after more than 1000 h under ambient air, but remain unchanged for 3000 h at elevated temperature in inert atmosphere, see Figure 5.11b and Figure 5.11c.

Table 5.3.: Perovskite solar cell characteristics corresponding to the representative J/V curves shown in Figure 5.11a for PSCs with a SnO$_x$ barrier layer grown by B-LP-ALD and S-AP-ALD, respectively. The current density data has been derived from EQE measurements (see Figure 5.12).)

	forward			
	PCE (%)	FF (%)	V_{OC} (V)	J_{SC} (mAcm^{-2})
S-AP-ALD	12.7	77.7	0.88	18.6
B-LP-ALD	12.6	75.6	0.89	18.8
	backward			
	PCE (%)	FF (%)	V_{OC} (V)	J_{SC} (mAcm^{-2})
S-AP-ALD	11.2	71.6	0.86	18.2
B-LP-ALD	11.2	69.9	0.87	18.5

The degradation of not-encapsulated PSCs is based the thermally activated decomposition of the perovskite material upon heating.[29] Additionally, an additional barrier layer prevents the ingress of moisture (from outside the device) into the active material.[74] It could be shown that the SnO$_x$ barrier layer hinders the PbI$_2$-based decomposition products (as MAI, HI orI$_2$) to diffuse out of the stack (and destroys e.g. the metal top-electrode) and at the same time protects the perovskite material against moisture. As can be seen in Figure 5.12, the batch-based low-pressure ALD based and the spatial ALD based encapsulated solar cells show similar short circuit current. The variation in the shape of the EQE could be be directly referred to the difference in the perovskite absorption spectra in dependency on their perovskite thicknesses. Slight variations of the perovskite layer in the range of 40 nm (which could not be excluded during the spin coating process) result in a different optical absorbance for wavelengths between 500 and 750 nm. These thickness variations fall within the process fluctuation and only result in minor changes in the J_{sc}.
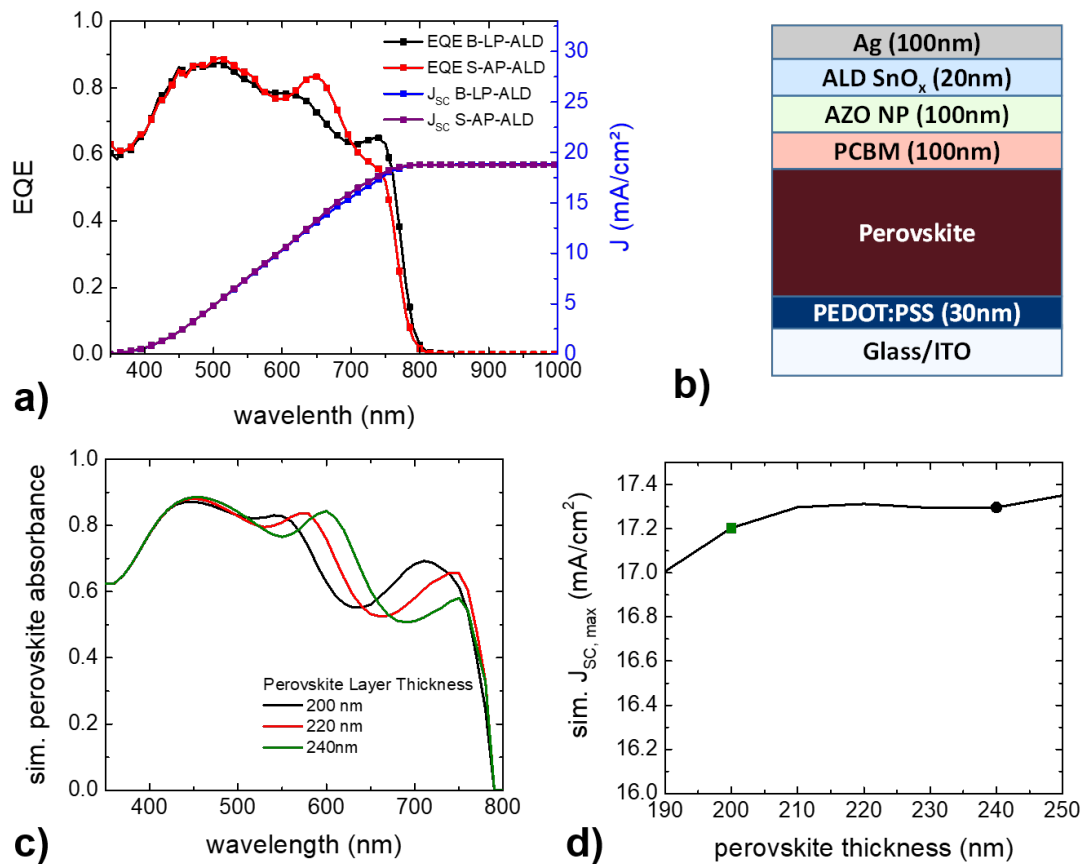
Figure 5.12.: EQE spectra and integrated photocurrent of perovskite solar cells based on spatial atmospheric pressure and batch low-pressure ALD (a). The optical absorbance of the perovskite layer in the shown PSC stack is simulated for tpyical layer thicknesses between (190 nm - 250 nm) (b). Due to the different perovskite layer thickness the resulting photocurrent of the solar cells could vary, simulated in Fig. (c). All optical simulations have been carried out using SETFOS. Based on ref.[4]

5.3.3 Dependence of deposition temperature on encapsulation

As mentioned above, the process temperature has a strong influence on the barrier properties, i.e. the WVTR. It already could be shown above that enhancing the ALD process temperature leads to thin films with higher film densities, higher electrical conductivities and generally a lower amount of precursor residues, not just in atmospheric pressure but also in the low-pressure processes.[193,195] An decreasing WVTR is observed towards higher deposition temperatures, depicted in Figure 5.13a. The WVTR decreases by about an order of magnitude from 1×10^{-4} gm^{-2}d^{-1} to 1×10^{-5} gm^{-2}d^{-1} at 60°C/60% rH. Concomitantly, RBS studies were performed, indicating that the amount of Sn atoms
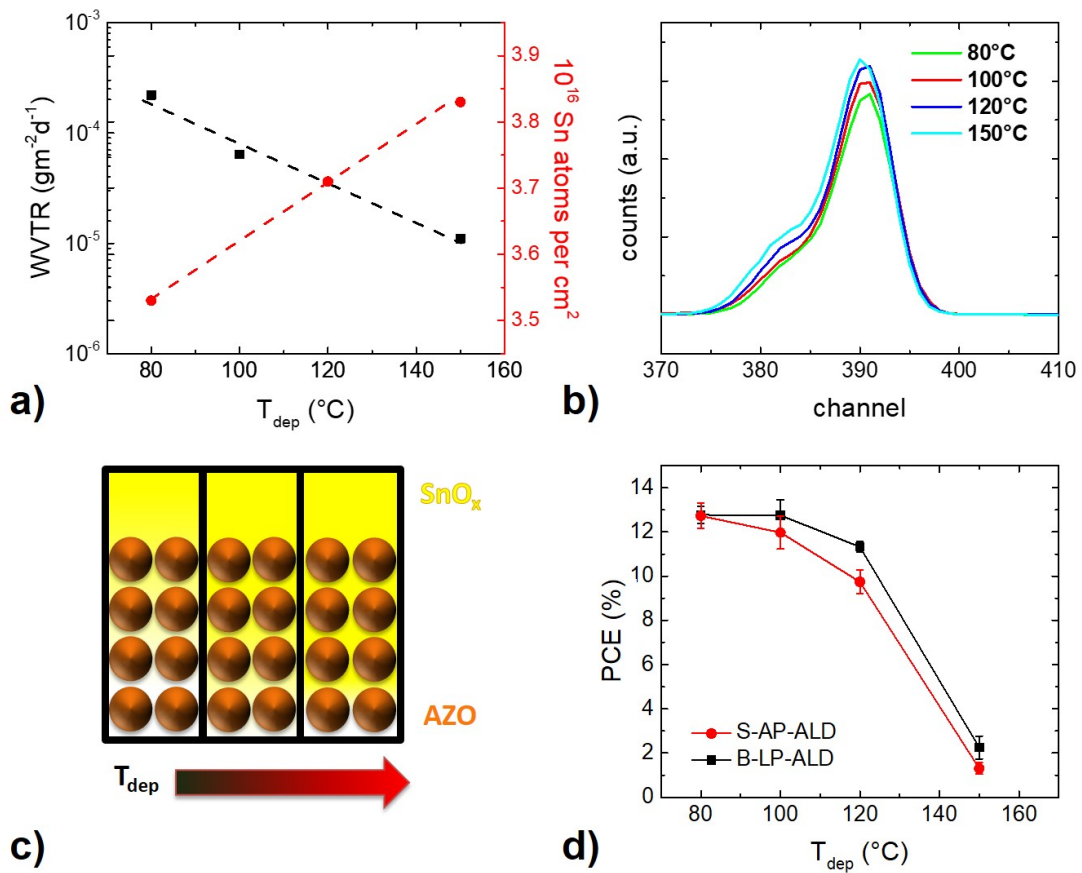
Figure 5.13.: Impact of deposition temperature on SnO_x as well as on SnO_x based PSCs. Water vapor transmission rate of SnO_x thin films (thickness 100 nm)) and tin atom density (measured by Rutherford Backscattering) for neat S-ALD SnO_x layers of each 20 nm thickness (a). RBS spectra of Sn measured on AZO (60 nm)/SnO_x hybrid layers with increasing deposition temperature (b). The corresponding partial growth of SnO_x inside the pores of the AZO layer is schematically shown in (c). PCE of the corresponding PSCs based on SnO_x grown at various temperatures (d). The substrate speed was 20 mm/s in this set of experiments. Based on ref.[4]

per area is increasing from 3.5×10^{16} to 3.8×10^{16} cm^{-1} in the temperature regime. Interestingly, the deposition temperature critically affects the depth of penetration of the SnO_x layer into the porous AZO layer, see Figure 5.13b. Performing RBS studies on AZO NP/SnO_x samples revealed the intermixing of those materials. The Sn-peak in the RBS spectra unravels that the higher the ALD process temperature is choosen the more Sn-atoms diffuse into the AZO pores, represented by the area underneath the characteristic shoulder in the RBS peak. For SnO_x grown on a flat, non-porous substrates (e.g. a Si-wafer) the Sn-related RBS spectrum is fully symmetric, regardless of substrate speed or precursor dose. For higher substrate temperatures, the Sn-atoms penetrate deeper

into the AZO pores, which is reflected by the shoulder in the RBS spectrum which extends further towards lower channel numbers. The filling of the AZO pores by the ALD grown SnO$_x$ is depicted schematically in Figure 5.13c. For further imrovement, higher deposition temperatures appear favorable, due to an increased mass density, lower WVTR, and better pore filling. Unfortunately, the PSCs encapsulated at 120°C and 150°C ALD deposition temperature show substantially deteriorated solar cell characteristics (Figure 5.13d). The dependency of fill factor, U_{OC} and I_{SC} is depicted in section A.3. It is important to note that the perovskite layers are post-annealed at 100°C. Therefore, the encapsulation with 100°C does not deteriorate the solar cells. For higher temperature, it has been shown, that the perovskite layer (MAPbI$_3$) degrades within minutes.[204, 205] As ALD always requires at least some exposure-time of the perovskite layer to the deposition temperature before barrier growth, the observed deterioration at ALD deposition temperature > 100°C is likely related to the thermal instability of those perovskite materials. Nevertheless, the use of high temperature ALD layers could be a promising approach for encapsulation layers underneath the perovskite (in an non-inverted solar cell) or in a setup, in which the encapsulation layer is laminated on top of the perovskite. Inverted perovskite solar cells, as used in this work, would require more temperature stable perovskite materials to benefit from the improved film properties at higher deposition temperatures in the ALD process.

Summary: The thin film growth of SnO$_x$ via spatial ALD has been demonstrated for the first time. SnO$_x$ based on atmospheric pressure processes show remarkable similarity in film quality (WVTR, density etc.) to their analogues grown by low pressure ALD. The introduction of SnO$_x$ as a diffusion barrier inside the perovskite solar cell stack affords devices with substantially improved long term stability upon exposure to moisture and elevated temperatures.

6

On the deposition speed of spatial ALD

The deposition speed is a major key parameter for the justification of spatial ALD. Assuming that high deposition velocities linked with extremely low process times would still allow for ALD-like deposition, spatial ALD would be acceptable for continuous high-throughput industrial applications. As a consequence, the growth properties vs. substrate velocity are investigated in the following chapter. Al_2O_3 as well as SnO_x deposition processes are performed with different oxidants and different substrate velocities. To evaluate the experimental data, fluid dynamics based computer simulations were carried out and compared to the experimentally determinded results.

6.1 Experimental Data

In case of spatial ALD, Poodt et al. propose the description of surface coverage for ALD growth by the following equation:[170]

$$GPC = GPC_{sat} \left(1 - \sum \alpha \cdot exp\left(-f(p,T,t)\right) \right) \tag{6.1}$$

As of that, the GPC can be described by a fixed GPC_{sat} and the deviation from this saturated GPC $f(p,T,t)$, which is a function depending on the growth temperature T,

the precursor partial pressure p and the residence time t. Furthermore it is proposed to simplify this equation to:

$$GPC = GPC_{sat} \cdot (1 - exp(a(T) \cdot t^q)) \qquad (6.2)$$

$a(T)$ is a temperature dependent prefactor, described by an Arrhenius relation,[170] and proportional to the diffusion coefficient and the inverse of the diffusion length. Regarding the t-dependency an exponential behavior is proposed, with $q = 1/2$ for ALD processes in which the GPC is either limited by the laminar boundary,[206] which thickness is proportional to $\sqrt{t}$, or by the time-dependent concentration gradient in the diffusion process.[170] If the process is not limited by these factors, q could differ from this $\sqrt{t}$-dependency. $q = 1$ equals the predicted t-dependency by the classical reaction equations, as $e^t = (1 + t)$ could be approximated for small t. Here, $GPC/GPC_{sat} \propto 1 - t$ applies. The longer the precursor is utilized (for $GPC < GPC_{sat}$), the thicker is the resulting film. Even if a $q > 1$-behavior is not fully understood yet, it can be hardly distinguished from GPCs limited by the boundary layer or diffusion.

6.1.1 Influence of the substrate velocity on the ALD growth of Al$_2$O$_3$

In the following GPC vs. substrate velocity is investigated for plasma- and ozone-based Al$_2$O$_3$ processes. First experiments were carried out with a 10 sccm N$_2$ flow through the TMA bubbler and 60 sccm of O$_2$ through the plasma source. Figure 6.1a and Figure 6.1b show the resulting data. The residence time t is calculated from the width of the precursor zone via:

$$t = \frac{2w}{v} \qquad (6.3)$$

In the setup used in this work w equals 2 mm. The prefactor '2' considers that the moving substrate is exposed to the TMA precursor twice during its back and forward oscillation in each cycle. Obviously, a saturated regime in which a constant GPC (= 0.17 nm) linked with a constant refractive index ($n = 1.60$) is obtained for substrate velocities up to 34 mm/s. This velocity corresponds to residence times of 0.1 s. For lower residence times e.g. higher deposition speeds, the GPC decreases to 0.05 nm at 120 mm/s (at 80°C). In parallel, the refractive index decreases towards higher substrate speeds to $n = 1.35$ at 100 mm/s, as also reported by Shin et al.[207]
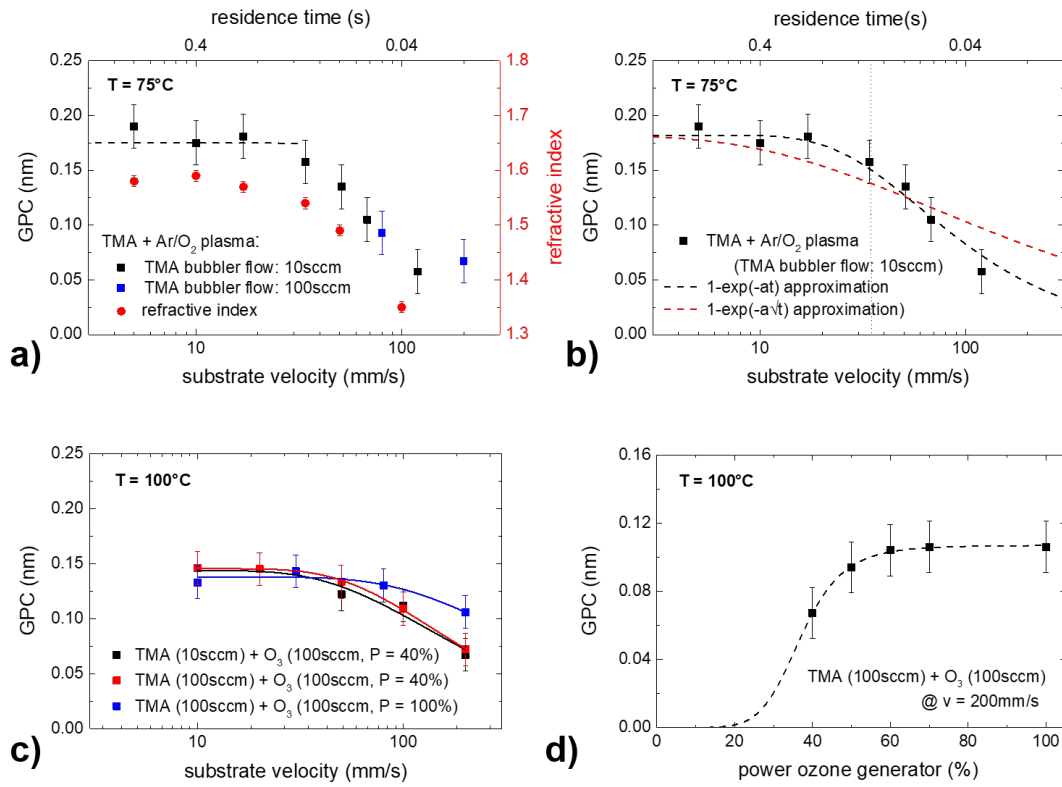
Figure 6.1.: Investigation on film growth vs. substrate velocity for Al_2O_3 by spatial ALD: a) Dependence of the GPC and the refractive index n on the velocity v for plasma based Al_2O_3 processes at 75°C and different precursor flows. b) Shown is the approximation of film growth by surface coverage theory with 1- exp(-at^q). The residence time is calculated based on a width of the precursor zone of 2 mm and the respective substrate velocity. c,d) Ozone based Al_2O_3 vs. substrate velocity and the power of the ozone generator. q = 0.86 (black), q = 0.96 (blue), q = 0.78 (red). The saturation of the GPC in d) is fitted with a Langmuir isotherm behavior.

Increasing the TMA dose (by enhancing the flow of N_2 through the TMA bubbler) does not extend the regime of constant GPC towards higher substrate velocities. This is very likely due to a lack of oxidizing species that limits the film growth at higher deposition velocities. A more unlikely reason can be that an increase of N_2 flow through the precursor bubbler does no longer increase the amount of TMA delivered to the substrate. However, Figure 6.1b shows that a fitting parameter q = 1 (based on classical reaction equations) achieve a better fit to the results compared to q = 1/2. Actually, best fit results are achieved with q = 1.36. This indicates that the reaction in this velocity regime is not limited by the diffusion or the boundary layer theory but by the amount of precursor. This precursor can be identified to be the oxidizing species created in the remote Ar/O_2 plasma, as higher amounts of ozone or water lead to higher GPCs at higher sub-

strate velocities, compare Figure 6.1c and Figure 6.1d. The growth studies with ozone show that in principle saturated GPCs at higher deposition velocities are achievable. At 100°C a GPC of 0.13 nm is obtained at 80 mm/s substrate velocity. As already depicted by the plasma based experiments, the GPC also slightly decreases with constant precursor flow towards higher speeds (GPC = 0.11 nm at 200 mm/s). The fitting parameters (q = 0.78 - 0.96) also indicate that the growth is not limited by a boundary layer, but by the precursor supply. A saturation curve for ozone based Al_2O_3 at 200 mm/s is depicted in Figure 6.1d. The GPC saturates at 0.11 nm at roughly 60% of the maximum ozone power of the ozone supplier. Note, the ozone concentration levels at approximatly 4.5×10^4 ppm with generator power of 60%. Increasing the power does not lead to a higher amounts of ozone molecules, available for the surface reaction (not shown here). Thus, the GPCs at 200 mm/s are still limited by the supply of oxidizing species. As shown in subsection 3.4.1 the ozone concentration generated by the DBD plasma sources in this work is in the range of 5×10^3 ppm, which is approximately one order of magnitude lower compared to the concentration generated with the commercial ozone generator. As the fitting factor q is becoming smaller with increasing precursor dose, i.e. the ozone supply, the hypothesis can be made that the alumina growth approaches the regime in which the growth is limited by the diffusion through the boundary layer ($\sqrt{t}$-type mode).

The GPCs of water-based Al_2O_3 films deposited at different substrate velocities are depicted in Figure 6.2. In principle, those layers show similar GPC for low precursor doses. 10 sccm of N_2 through the water- and through the TMA bubbler lead to ALD like growth up to substrates velocities of 34 mm/s. This upper limit of saturation was already found for the plasma- and ozone-based ones. In the water-based processes, $q = 1$ can be obtained for low H_2O doses (flow rates). With higher doses this regime extends towards higher substrate velocities but also leads to higher GPCs for low substrate velocities. Here, long residence times effect the substantial onset of parasitic CVD-like growth. Indeed, ALD is also a special type of CVD, here, CVD is synonym for not self-limited growth based on gas phase reactions of the precursors. This CVD onset can be reasoned, on the one hand, by the high sticking coefficient of water[21,24] or, on the other hand, by an intermixing below the ALD head. It even held true at higher substrate temperatures (100°C). Extending the purge flows to 4000 sccm N_2 per slot does not reduce this onset. As CVD is a time-dependent process, its presence gets more dominant for longer process times which are directly the result of low substrate velocities. As such, inhomogeneous growth rates for Al_2O_3 are obtained, see Figure 6.2c. ALD type of growth reveals homogeneous thin film growth (Figure 6.2d). Note that the marked stripes are

the result of a lift-off process for measuring the film thickness.
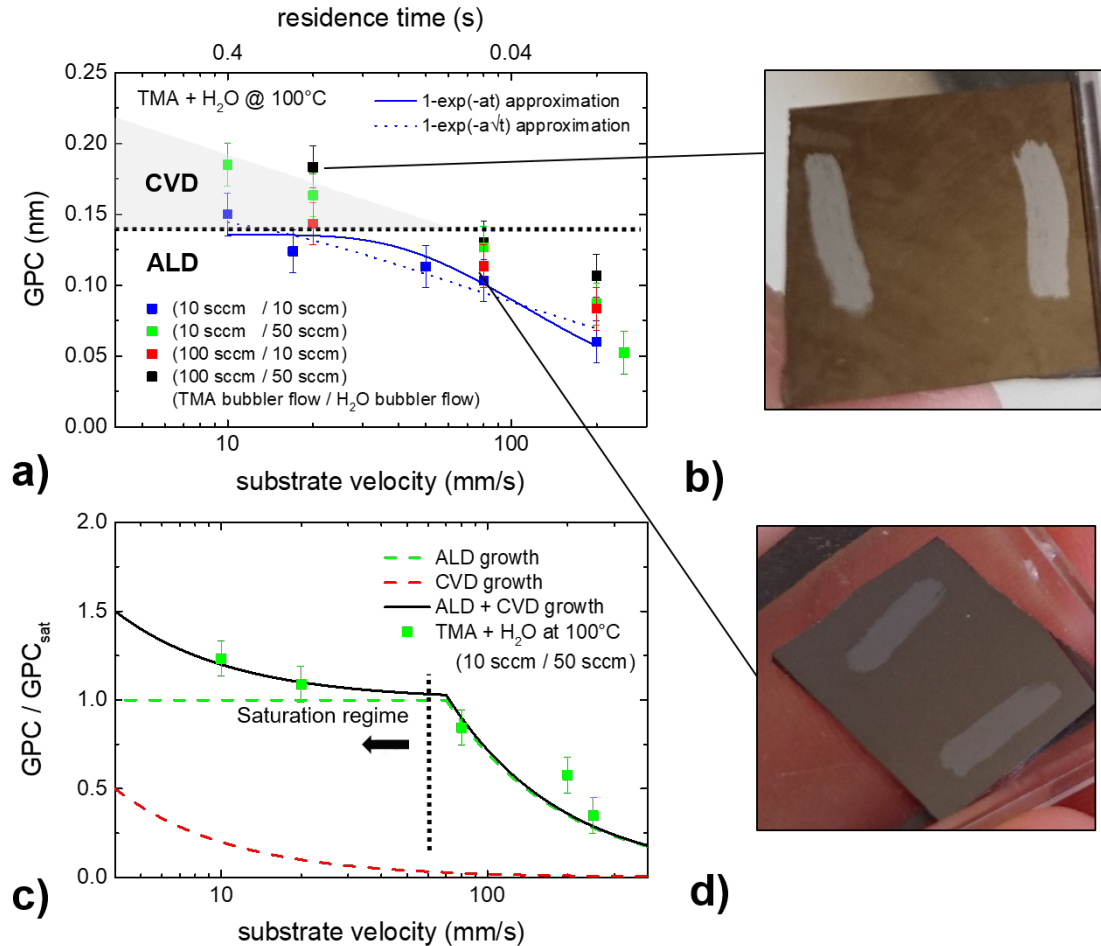
Figure 6.2.: Dependence of the GPC on substrate velocity in spatial ALD Al_2O_3 + H_2O processes revealing an CVD and an ALD regime, strongly dependent on the precursor doses. a) GPC vs. substrate velocity for different amounts of precursor dose. The resulting difference in film quality can be observed by eye (b,d). Figure c exemplified the CVD-onset on the ALD growth.

Generally, a $1/v$ - behavior can be assumed for the GPC of CVD kind of growth as the process is not self-saturated. In this kind of CVD growth, doubling the residence time of a precursor would lead to doubling the film thickness. More specifically, the CVD growth is direct proportional to the number of cycles (N) and the width of the precursor zone w as well as the the inverse of the substrate velocity v. Taking the saturated ALD growth rate into account the resulting film thickness d in a mixture of ALD and CVD

can be described with:

$$d = d_{ALD} + d_{CVD} \tag{6.4}$$

As ALD growth represents the self-saturated process, which is, when the substrate surface is once fully saturated, independent of time or any spatial length. Here the film thickness is linear dependent on the number of cycles N, as already verified for Al_2O_3 and SnO_x layers. Further on, the film thickness can be written as:

$$d = \frac{\Delta d}{\Delta N}|_{ALD} \cdot \Delta N + \frac{dd}{dt}|_{CVD} \cdot \frac{2N\Delta w}{v} \tag{6.5}$$

The term '2' is added due to the back- and forward moment of the ALD table, passing each precursor zone twice in one cycle. As the GPC is the film thickness d divided by the number of cycles N, it resulting overall GPC can be expressed as:

$$GPC = \frac{d}{N} = GPC_{ALD} + \frac{dd}{dt}|_{CVD} \cdot \frac{2\Delta w}{v} \tag{6.6}$$

Therefore, an additional growth of CVD has to be added to the ALD growth, illustrated in Figure 6.2c. The green dotted line represents the ALD type of growth which is saturated till a certain substrate velocity to its GPC_{sat} (e.g. 70 mm/s). Towards higher substrate velocities, the unsaturated regime is also represented with a v^{-q} with q = 1 behavior. This exponent q could vary due to the growth limiting factors as mentioned above. Additional CVD growth on the overall saturated ALD growth is represented by the red hyperbola. Taking both types of growth into account, the overall actual observed growth behavior in Figure 6.2a can be explained reasonable well. Exemplary the CVD growth of the TMA/H_2O process at 100°C deposition temperature (N_2(TMA) = 10 sccm, N_2(H_2O) = 50 sccm) is fitted as additional term to a saturated ALD-based GPC of 0.15 nm, resulting a additional CVD-related term of (0.33±0.03) nm/v. Considering the residence time t (compare Equation 6.3) and the 2 mm wide precursor zone, a CVD growth rate can be calculated to (0.08±0.01) nm/s. Note that this value is based on the assumption, that CVD growth only takes place inside the (2 mm wide) precursor zone. As it is more likely, that CVD takes place over the complete width of the substrate movement (approximatively 120 mm), a CVD growth rate of 2.8×10^{-3} nm/s is a more realistic estimate.

6.1.2 Influence of the substrate velocity on the ALD growth of SnO$_x$

The SnO$_x$ growth per cycle vs. substrate velocity is depicted in Figure 6.3. All experiments were performed with a N$_2$ flow of 150 sccm through the TDMASn-bubbler, which is kept at ambient conditions of the glove box without intentional heating. Similar growth behavior for water and the Ar/O$_2$-plasma-based processes is observed. For 100°C deposition temperature a decay in GPC for substrate velocities higher than 30 mm/s is found.
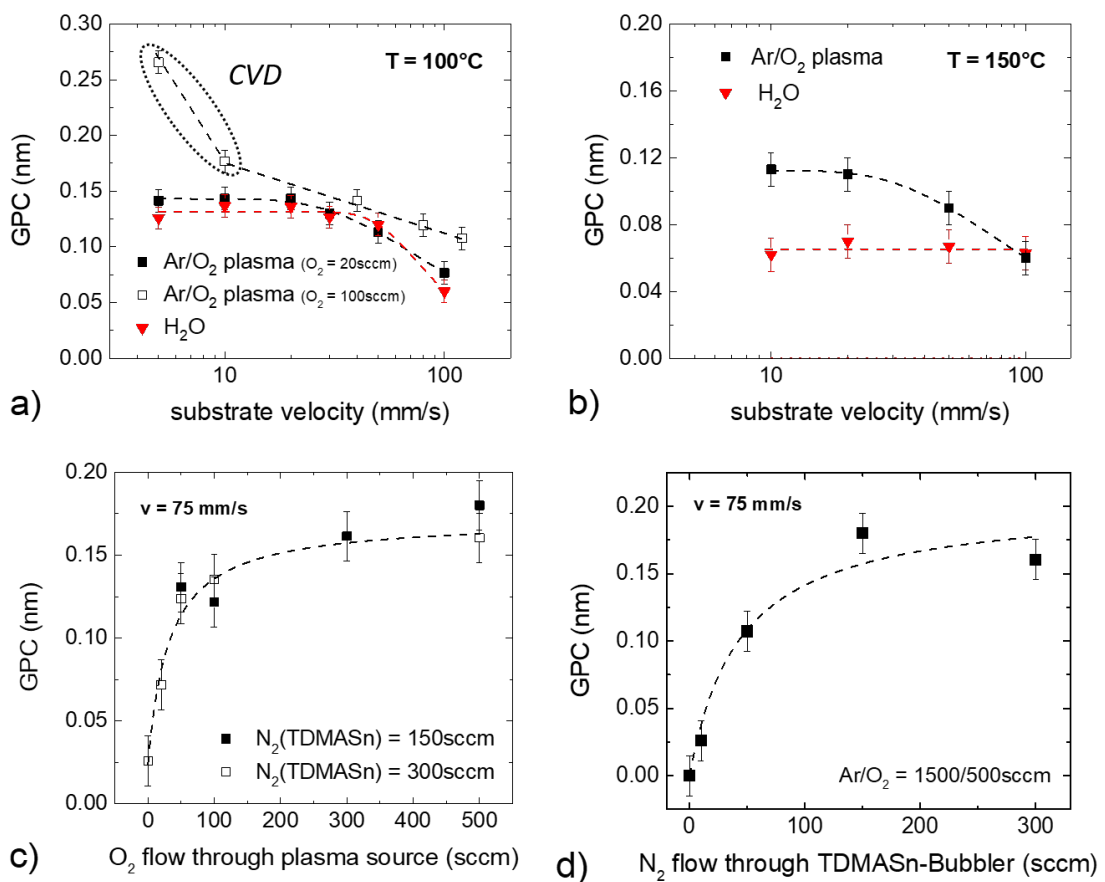
Figure 6.3.: GPC vs. substrate velocity for plasma- and water based SnO$_x$ processes at 100°C (a) and 150°C (b). The dashed lines are the result of fitting to the experimental data as mentioned above (with q ranging between 1 and 2). (c,d) show the dependency of the GPC on the precursor dose at a relatively high substrate velocity of v = 75 mm/s at T =100°C. Here, the dashed lines are guides to the eye.

As already seen for the influence of the substrate velocity on the ALD growth of Al$_2$O$_3$, the growth of the metal oxide (SnO$_x$) is not limited by the diffusion of the precursors

through the boundary layer, indicated by $q = 1$ for plasma-based and $q = 2$ for water-based ALD, but rather by the precursor supply. In parallel to the previous observation, the regime in which GPC equals GPC_{sat}, can be extended to higher v by an increased amount of the oxidizing precursor delivered to the precursor exposure zone. Here, increasing the amount of oxygen in the plasma increases the GPC at higher substrate velocities (e.g from 0.08 nm to 0.11 nm), but also leads to higher GPCs for substrate velocities < 10 mm/s. Again the increased GPC (of 0.27 nm) can be explained by parasitic CVD growth as discussed earlier (compare Figure 6.2c). The additional CVD growth rate can estimated to 4.5×10^{-3} nm/s in analogous way as already shown for the water-based Al_2O_3 layers.

Higher deposition temperatures (150°C) lead to a saturation behavior of the GPC as seen in the low temperature processes. Note that the GPC of water-based SnO_x dramatically decreases with increasing temperature, as already discussed earlier. For high velocities of 75 mm/s, saturation in the GPC can be achieved for a flow more than 100 sccm of oxygen used in the Ar/O_2 plasma (Figure 6.3c). The corresponding saturation in the tin precursor dose is shown for a the high oxygen-to-argon ratio of 1:3 with 500 sccm of O_2(Figure 6.3d).

6.1.3 Dependence of deposition speed on barrier properties

In the following the dependence of the deposition speed on the encapsulation layer of actual perovskite solar cells is investigated. Here, the perovskite solar cell setup is used as already presented in section 5.3. Therefore, the typical GPC vs. substrate velocity behavior is observed for a TDMASn/H_2O process at 80°C deposition temperature.
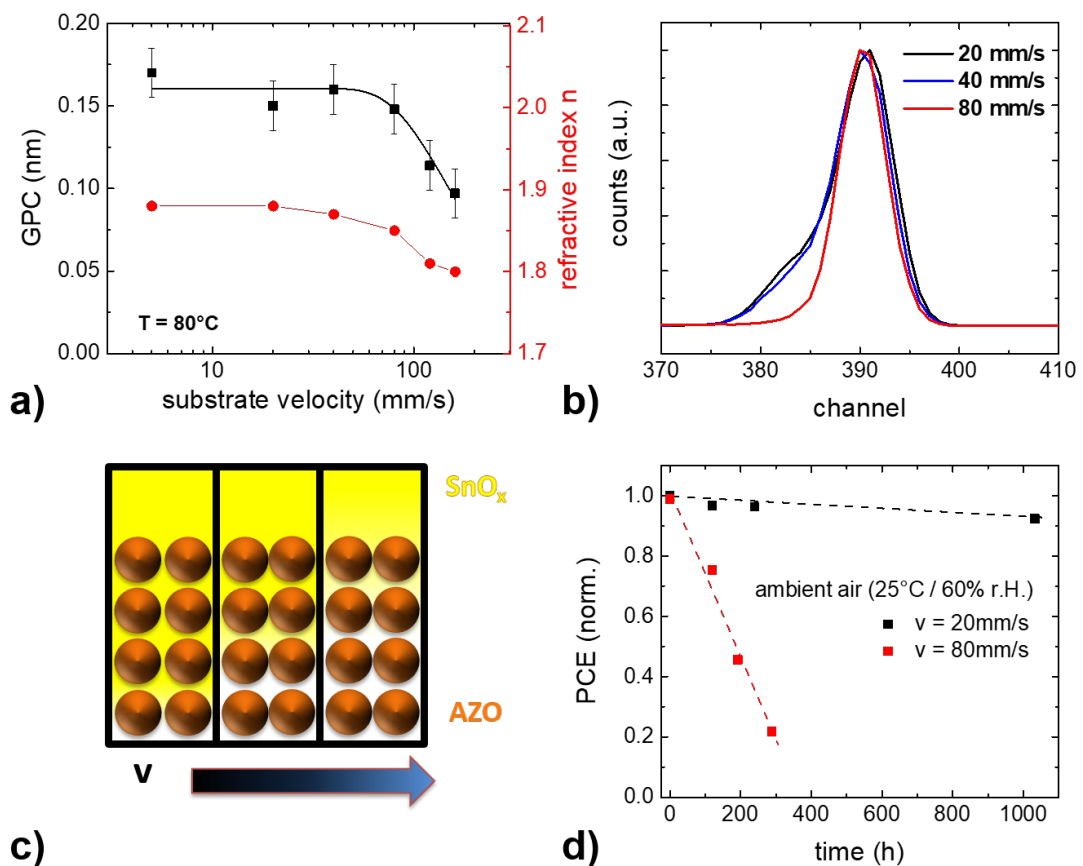
Figure 6.4.: Dependence of deposition speed on AZO/SnO$_x$ encapsulation layer: GPC and refractive index of SnO$_x$ vs. substrate velocity at 80°C deposition temperature (a). Normalized RBS signal of tin deposited on AZO at varied substrate velocities. a AZO/SnO$_x$ hybrid layer structures is reveals by the characteristic shoulder in the RBS signal (b). Schematic of the diffusion of SnOx (yellow) inside the AZO NP-layer (c). Lifetime of a PSC (Normalized PCE vs. time of storage) in ambient air (25°C, 60% r.H.) for solar cells with SnOx layer grown at 20 mm/s (saturated regime) and 80 mm/s (unsaturated regime), respectively (d).

The characteristic decrease in GPC after a certain saturation regime (here approximately 60 mm/s) is depicted in Figure 6.4. As already discussed above the refractive index is

decreasing in almost the same manner i.e. from 1.88 at 20 mm/s to 1.80 at 160 mm/s, indicating not fully-saturated ALD film growth and a lower film density. Aside from this, it has to be noted that the substrate velocity may have an additional effect on the encapsulation layer in the perovskite solar cell. As the Al:ZnO layer underneath the SnO_x layer is a porous structure, formed from a dispersion of nanoparticles, the Sn precursor is able to diffuse inside this porous structure. This diffusion directly depends on the substrate velocity, as illustrated in Figure 6.4c. The functionality of the AZO/SnO_x hybrid layer as a permeation barrier and protection layer relies critically on the penetration of ALD precursors i.e. the TDMASn into the pores of the AZO layer and on the concomitant growth of SnO_x inside these pores.[74] In Figure 6.4b single 20 nm of SnO_x is deposited on the AZO layer at different substrate velocities. As the characteristic shoulder in the RBS peak of tin shifts to lower energies (i.e to lower channels) tin is penetrating deeper into the AZO, revealing the formation of the AZO/SnO_x hybrid layer. At higher substrate speeds of 80 mm/s no diffusion can be observed any more, represented by the symmetric shape of the tin-peak in the RBS spectra. As direct result from the absence of tin-diffusion into the AZO pores, the barrier properties of the resulting hybrid layers are substantially inferior compared to those where the SnO_x can contribute to the pore filling (i.e at lower substrate velocities). In addition, the WVTR of single SnO_x layers grown at 80 mm/s show inferior permeation barrier properties (WVTR = 4×10^{-3} $gm^{-2}d^{-1}$) compared to their analogue grown in the saturation regime (v = 1 - 60 mm/s). This can be reasoned by the overall deterioration of layer density at elevated substrate speed, which is represented by observed drop of the refractive index as discussed above. As result of the discussion, the lifetime of the PSCs is strongly dependent on the choice of substrate speed. At ambient air (25°C / 60% r.H.) the PCE of those cells encapsulated with 80 mm/s in the spatial ALD decreases dramatically within the first 300 h due to an insufficient encapsulation layer. On the contrary, PSCs encapsulated at saturated conditions at 20 mm/s only slightly decrease even after more than 1000 h, see Figure 6.4d.

The observed drop in GPC at substrate velocities of 34 - 60 mm/s corresponds to precursor residence times between 70 and 120 ms. These critical substratet velocities are on the same order as reported for other spatial ALD setups at atmospheric pressure (ZnO: 3.5 m/min = 58 mm/s[19] and 3 m/min = 50 mm/s,[18] Al_2O_3: 1.57 m/min = 26 mm/s[53]). Indeed, there are also reports who observe extended CVD growth for web velocities higher than 7 mm/s,[140] but the common understanding is that residence times (i.e. exposure times of the precursors) can be reduced while still guaranteeing surface saturation.[170] As reported for TMA/H_2O processes, corresponding exposure times in the range of milliseconds already provide half of the saturated GPC, as a 15-27 ms

TMA/H$_2$O exposure time provides fully saturated growth.[170] Linked with those short exposure times, very high velocities can be achieved taking an adequate width in which the substrate is exposed to the precursor. For the setup used in this work, exposure times of 20 ms correspond to a maximum substrate velocity of 200 mm/s with a width of the precursor zone of 2 mm (the width of the precursor slit). Taking the width of the gas outlets into account, as already discussed in section 3.3, the exposure times necessary for saturated deposition increase to 2000 ms. Generally, Poodt et al. claim a limiting $\sqrt{t}$-dependency which indicates at diffusion limited mass transport of the precursor to the substrate.[170] In sharp contrast, the surface coverage of the thin film deposition in the spatial ALD in the investigated substrate velocities (1 - 200 mm/s) is dominated by a limited supply of precursor mass.

6.2 Simulation of ALD growth

To obtain better insight into the gas flow dynamics in the spatial ALD process, theoretical simulations are conducted. More specifically, these theoretical simulations of the gas flow dynamics in the spatial ALD were calculated, evaluating the limits of ALD growth in terms of substrate velocity. The simulations are carried out using the *OpenFoam* software platform, a solver for the relevant diffusion equations. In addition the *OpenFoam* library enables the inclusion of chemical reactions and the evaluating of a time-depending process. Also, compressible fluids can be calculated based on non-constant gas densities. Inside the structure the solver *reactingFoam* is used to solve the differential form of the species transport equation. Further details on the the implementation of the physical fundamentals can be found in section A.4.

6.2.1 Simulating the surface coverage

For all simulations a simulation grid, as depicted in Figure 6.5 has to be defined, framing the actual deposition design. With the help of boundary conditions (e.g. change in velocities equals zero), walls, but also surface sites are taken into account. The grid consists out of different cells which can be seen as smallest physic space of a single physical state.
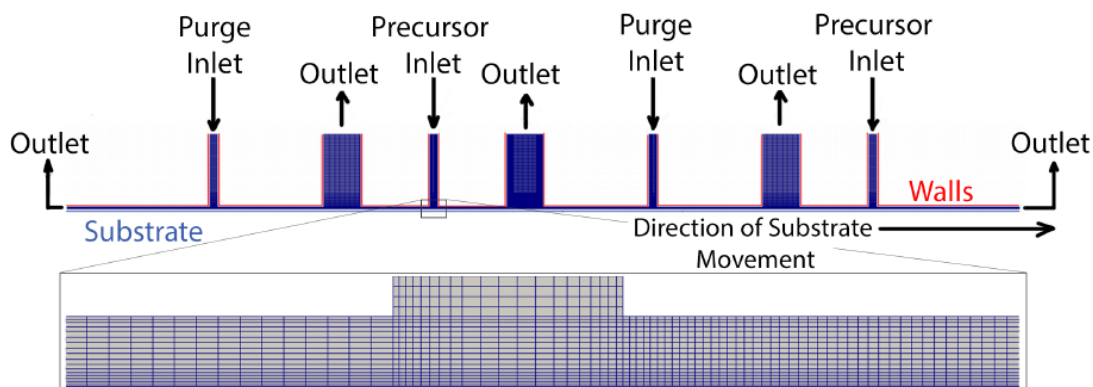
Figure 6.5.: Simplified two dimensional computational mesh for surface coverage simulation in spatial ALD. The mesh is adapted to the real distance of the ALD head. For surface coverage simulations this grid as to be modified in time and space. Different resolutions are chosen due to the desire of reducing the overall computing time. The lower edge of the grid can be understood as substrate sample in terms of evaluating the time-depending surface sites.

Note that the resolution chosen in the critical regimes (i.e edges, small gaps) is always a trade-off between accuracy and computing time. As of that, a resolution of 17 cells is chosen for all following simulations. With this, velocity profiles, temperature distributions or gas separation can be simulated. In the following, the increase of the surface coverage as representative for the deposition rate is calculated. Therefore, the simulation grid gets modified in time and space. The modification in space means for example that the grid, which is usually a fixed environment for the gas flows, is shifted to the left or the right depending on the direction of the substrate movement.

6.2.2 Model and assumption

For the follwing part the simulation is modified so that the surface reaction of injected precursor molecules can be estimated. Therefore, the physical boundary condition between the gap above the ALD table at the table itself has be changed, as illustrated in Figure 6.6. If no chemical reaction take place, the boundary was simulated as a wall with zero velocity gradient perpendicular to this wall. If the reaction of precursor molecules with the surface is desired, the diffusion of molecules on the surface (i.e through the 'wall') has to be considered. The concentration at the boundary cell face is initialized with a value of zero at the t = 0 s. The precursor gas concentration at the boundary cell center is taken from the results of the previous time step of iteration. Now, a mass flux can be obtained if the concentration at the boundary cell face is smaller than in the center of the cell. This diffusive flux can be calculated as follows (see Fick's law, Equation 2.14)

$$J_{diff} = -D \cdot \frac{dc}{dx} \tag{6.7}$$

$$J_{diff} = -D_{eff} \cdot \frac{\rho \cdot (c_{CC} - c_{BF})}{\frac{h_{cell}}{2}} \tag{6.8}$$

Here, the concentration gradient is represented by the difference between the concentration at the boundary cell center (c_{CC}) and the boundary cell face (c_{BF}) devided by the respective lenght, the half of the unit cell ($\frac{h_{cell}}{2}$). Also μ_{eff} is replacing the diffusion coefficient of the mixture as the Schmidt number equals 1. The Schmidt number represents the relation between momentum diffusivity and mass diffusivity, characterizing fluid flows.[72] For gaseous media the Schmidt number (normally) equals 1.[208] To calculate the increase of the surface coverage the diffusive mass flux has to consider the amount of the precursor. Here, TMA is taken as precursor system. The diffusive mass flux density is converted into a particle flux density (ΔQ) by respecting the Avogadro number and the molecular weight of TMA (72.09 g/mol). Afterwards, the flux is divided by
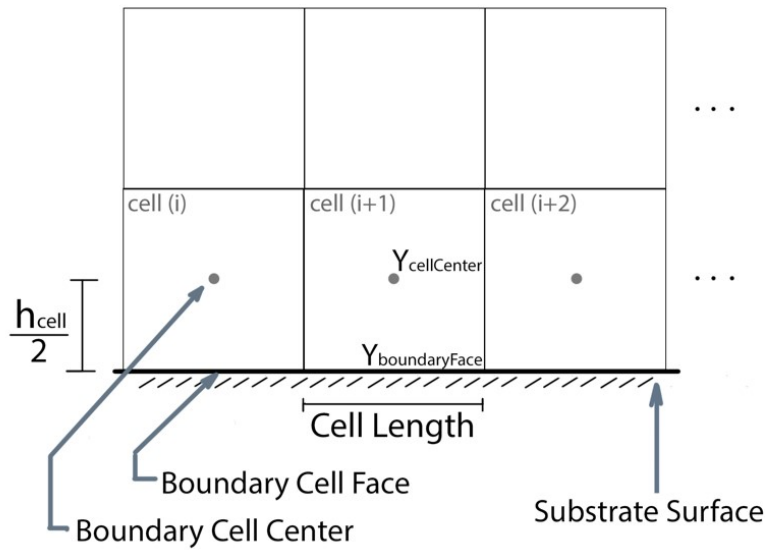
Figure 6.6.: Computational mesh for simulating the surface coverage: The reactive surface of the is represented by the cells which share a cell with the boundary. The boundary face of the lowermost cell is representing the substrate surface.

the sorption site density of the Al_2O_3 surface to calculate the increase of coverage. As this procedure is time-dependent the flux has to be multiplied by the duration of the previous interation Δt.

$$\Delta Q = \frac{J_{diff} \cdot N_A}{2 \cdot M_{mol,TMA} \cdot C_s} \cdot \Delta t \tag{6.9}$$

C_s represents the sorption site density on an Al_2O_3 surface. The sorption site density can be calculated, assuming the number of constituent particles (i.e. the Avogadro number) in a cubic volume of aluminum oxide Al_2O_3 which can be mathematically converted into a surface value (by using the exponent 2/3). Assuming the density of bulk Al_2O_3 ($\rho_{Al_2O_3}$ = 3.95 - 3.98 gcm^{-3}[209])and the molecular weight, C_s can be estimated as follows:

$$C_s = \left(\frac{N_A \cdot \rho_{Al_2O_3}}{M_{mol,Al_2O_3}} \right)^{\frac{2}{3}} \tag{6.10}$$

With this assumption the surface coverage can be calculated by the summation of the coverage Q in each respective time step. Here, the surface coverage is just based on Fick's law. Due to this the value Q could naturally exceed the value one, as diffusion is not limited. As $Q > 1$ is physically impossible in terms of ALD growth, in this case the value of Q is automatically reduced to one, representing a fully saturated, chemically inert surface. Also, the new precursor gas concentration at the boundary (Y_{BF}) is subse-

quently set equal to the concentration at the cell center (Y_{CC}), multiplied by the surface coverage Q. The precursor concentration gradient at the boundary now gets modified dynamically:

$$Y_{BF} = Y_{CC} \cdot Q. \tag{6.11}$$

Here, simulation cells with zero surface coverage result in the largest possible concentration gradient, implying a perfectly absorbing surface, and vice versa. Finally, to achieve the spatial character in the simulation, the motion of substrate in the Spatial ALD system is considered. Therefore, the surface coverage values of each boundary cell face (Y_{BF}) are shifted to their respective neighbour, strongly dependent on the substrate velocity. The latter defines the certain simulation time considering the respective cell length. All in all, this simulation is able to estimate surface coverage in dependency on the substrate velocity of the Spatial ALD. It is important to note that several assumptions were made in this model, for example just one precursor (especially the mass of TMA) is considered.

6.2.3 Analysis of the substrate coverage

Taking the model as described above, the surface coverage could be simulated for different precursor concentration in dependency of substrate velocity. The results are shown in Figure 6.7. Every data point represents the result of the simulation of the surface coverage. The data is fitted by the function Q_{fit}. The parameter A represents a fitting coefficient, which is proportional to the injected precursor concentration ($A \propto Y_{in}$).

$$Q_{fit} = \begin{cases} 1, & if \frac{A}{v} \geq 1 \\ \frac{A}{v}, & otherwise \end{cases} \tag{6.12}$$

This sectionwise defined function considers the fact that surface coverage can generally be divided into two regions: The saturated and the unsaturated regime, where the surface sites are not fully reacted with its co-reactors. The equilibrium surface coverage starts to decrease (from a fully saturated to a non-saturated value) after a critical substrate velocity. Obviously this is based on the fact that with increasing substrate velocity the exposure time of the substrate to the precursor is decreasing. In addition, the critical substrate velocity is strongly dependent on the precursor concentration. This result shows a linear proportionality between the surface converages and the precursor concentration (represented by the black arrows in Figure 6.7). For GPCs $<$ GPC$_{Sat}$ injecting

the triple of the precursor concentration (e.g. TMA) leads to a triple in surface coverage. This is in direct agreement with the classical reaction equations and the theory of Fick's law which provides the linear increase in diffusive mass transport per time as a result of an increasing species concentration.
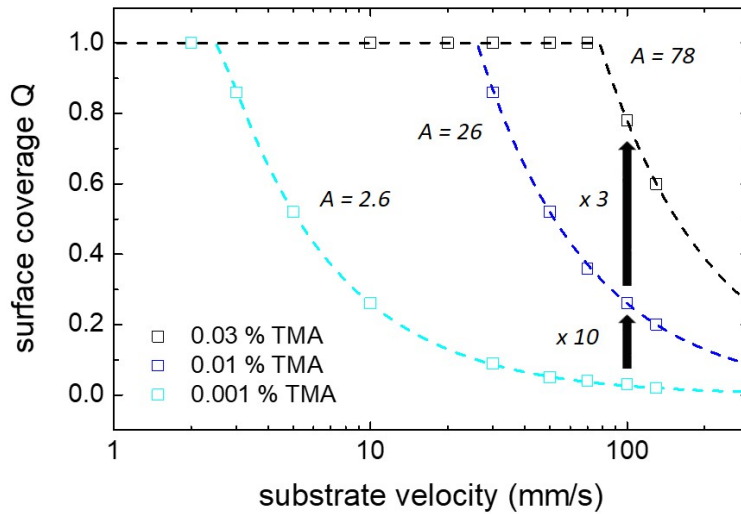
Figure 6.7.: Simulation of the surface coverage vs. substrate velocity for different TMA precursor concentration and with a constant volumetric flow. The fit is done by an composed function, assuming an $1/v$ behavior for the unsaturated precursor regime.

As the surface coverage is directly proportional to the substrate velocity and therefore to the exposure time, needed for fully covered surfaces, this behavior can be plotted in Figure 6.8b. Obviously, the critical velocity is reached when A/v is equal to one, or in other words: When the substrate velocity matches the fitting factor A. In addition, these simulations demonstrate that the deposition process under non-saturated conditions (e.g. at high substrate velocities) in not evenly distributed throughout the deposition zone.

All in all, assuming that the injected number of precursor molecules is not sufficient for surface saturation, the limited extension of the deposition zone leads to a potentially limited supply of the amount of precuror. This implies that the more precursor is injected, the further the critical velocity shifts towards higher numbers.

6.2.4 Validation of simulation and experiment

For further investigation, the experimental data can be directly compared with the data resulting from the simulation. Figure 6.8a shows the experimental data of an Al_2O_3 ALD process deposited with TMA and an Ar/O_2 plasma at 75°C deposition temperature as well as the corresponding simulation results. In the simulation the flow of TMA is varied from 0.5 sccm to 0.16 sccm. 0.16 sccm of pure TMA gas corresponds to the maximum yield if 10 sccm of N_2 gas is purged through the TMA bubbler and fully saturated with TMA considering the TMA vapor pressure (see Equation 3.1). In the experiment 10 sccm N_2 was used for the carrier flow through the TMA precursor. In addition, the simulations are based on the assumption that the substrate passes the precursor regimes just once. For further comparison, two way passing has to be considered as the substrate moves back and forward under the ALD head. This basically leads to doubling the width of the precursor zone. To convert the GPC measurements into an surface coverage Q per cycle, the following approach is used, based on the work of Puurunen et al:[49]

$$Q/cycle = GPC \cdot \frac{\rho_{Al_2O_3} \cdot N_A}{C_s \cdot M_{Al_2O_3}} \tag{6.13}$$

In this equation, N_A is Avogadro's number (mol^{-1}) and $M_{Al_2O_3}$ is the molar mass of Al_2O_3. C_s represents the number of the available surface sites. The model above only considers the resulting surface coverage per cycle by the TMA half reaction. The actual system is a result of the completion of both half reactions (TMA + Ar/O_2 plasma). As the growth characteristics is most likely defined by only one of the precursors (while the counterpart is saturated), this does not compromise the model. Taken the process data from the experiments ($\rho_{Al_2O_3}$ = 2.5 gcm^{-3}, GPC = 0.179 nm (compare section 4.2)) and assuming the boundary condition Q_{sat} = 0.5 due to the steric hindrance of the ligands as discussed in subsection 2.1.1, a density of the adsorbed TMA can be calculated to be 5.3 nm^{-2}, strongly agreeing earlier reports for TMA/water processes in conventional vacuum-based ALD systems. There, the adsorbed TMA molecules ranged from approximately 3.6 nm^{-2} to 5.2 nm^{-2}, depending on the hydroxyl surface concentrations as well as the surface temperature.[49,210,211] The assumption of the steric hindrance (with Q_{sat} = 0.5) is calcuted as follows:

$$Y = Y_{CC} \frac{Q}{Q_{sat}} \tag{6.14}$$

Note that the critical velocity would shift towards higher values, depending on the severity of the steric hindrance. Here, a higher steric hindrance (i.e a lower Q_{sat}) would shift the critical velocity towards higher numbers. The final comparison of the experimental data and the simulation is shown in Figure 6.8b.
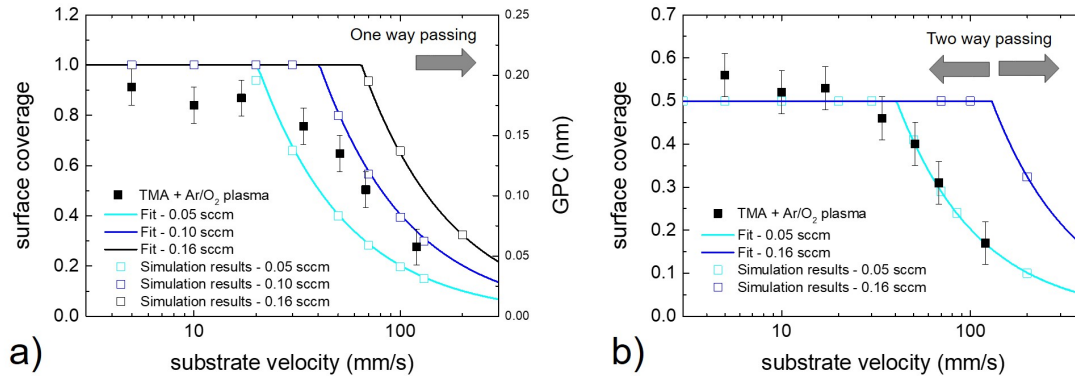
Figure 6.8.: Simulation of the surface coverage vs. substrate velocity for different TMA precursor concentration and with a constant volumetric flow. a) The fit is done using a composed function, assuming an $1/v$ behavior for the unsaturated precursor regime. Further parameter for both plots are: substrate temperature = 353 K, gap height between ALD table and ALD head = 300 μm, gas flow = 1200 sccm. Note that simulations in figure a) only consider one-way passing of the precursor regime, while simulations in b) take the back- and forward movement of the substrate table as well as the steric hindrance into account.

Interestingly, the simulations results (with TMA 0.05 sccm) show an excellent agreement with the experimental data despite the use of the simplified model. However, this observation may suggest an TMA flow of 0.05 sccm as actual yield of the precursor bubbler. On the other hand, previous experiments (see discussion to Figure 6.1) have shown that the process showed above is not limited by the TMA delivery but by the supply of oxidizing species. Note that assuming the maximum precursor yield of TMA would enhance the critical velocity by a factor of 3. In addition higher amounts of precursor gases would also extend the saturation regime towards an elevated substrate velocity. The projected theoretical improvement of this process by increasing the precursor flow rates is depicted in Figure 6.9. Here, the precursor flow for saturated growth is depicted in dependence of the critical exposure time and critical substrate velocity. Obviously, the currently attainable throughput is limited in the TMA/plasma process due to the already mentioned reasons. For ozone based processes higher throughputs are observed. Note that higher velocities entail concomitantly lower exposure times. Here, one has to further investigate on the expansion of the actual precursor regime. Thereby, two
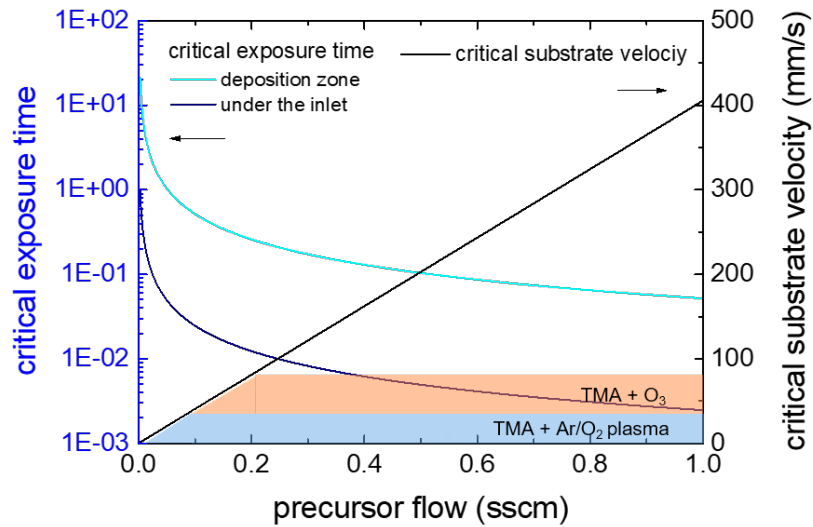
Figure 6.9.: Critical substrate velocity, related to the onset of the decreasing surface coverage and the critical exposure time as function of the precursor flow. For calculations, the carrier flow gas were set to 2000 sccm and the gap height to 300 μm. The actual regime achieved in the experiments are marked with the red and blue area.

different exposure times could be calculated, based on the width of the deposition zone (2 mm), or the width between the gas outlets, defining an even wider deposition zone. All in all, the theoretical investigation reveals that the amount of precursor is the dominating parameter for saturated ALD growth at high velocities, and therefore for high throughput ALD. Remarkable accordance of experimental and simulated data could be found in terms of the TMA/plasma process and the unsaturated regime. With the help of the simulation, a prediction of the preecursor yield at lower substrate velocities or the limitations towards higher substrate velocities could be made.

Summary: The deposition of Al_2O_3 and SnO_x thin films via spatial ALD with substrate speeds up to 75 mm/s have been achieved. The experimental dependence of film growth on substrate speed has been theoretically simulated with an excellent agreement. It has been shown that the supply of precursor critically governs the maximum (critical) velocity in the spatial ALD process.

7

Conclusion

With the increasing demand of (opto)electronic devices, large-scale roll-to-roll fabrication is elementary to fulfill the industrial throughput requirements. The deposition of those devices on roll-to-roll compatible substrates simultaneously enables the possibility of mechanical flexible devices. As OLEDs, PSCs etc. need barrier layers to protect the sensitive active material inside the devices against ambient influences, in terms of flexibility glass could not serves as encapsulation. Here, flexible, transparent gas diffusion barriers are required. More precisely, also conductive gas diffusion barriers have to be provided if the barrier is placed inside an (electrically) functional device (e.g. between the active material and the electrode of a solar cell). Generally, those GDBs have to posses a thickness larger than 20-30 nm to provide a sufficiently low intrinsic WVTR on the order of 10^{-5}-10^{-6} gm^{-2}d^{-1}.

In this work, conductive and non-conductive gas diffusion barriers were deposited in a spatial ALD system at atmospheric pressure, which show the intrinsic WVTR required to encapsulate OLEDs or to suppress the decomposition mechanism in PSCs. At first, Al_2O_3 thin films were deposited in batch-based plasma ALD system at atmospheric pressure. The saturation in the aluminium precursor dose and plasma duration was evidenced, resulting in a growth per cycle of (0.18 ± 0.02) nm at 80°C. Those thin films deposited on flexible PET-ITO substrates show a WVTR as low as 7×10^{-5} gm^{-2}d^{-1}. These excellent barrier properties even persist under mechanical strain. The concept of atmo-

spheric pressure ALD could be transfered to a spatially separated delivery of the ALD precursor sequence. Here, Al_2O_3 gas diffusion barriers prepared by spatial ALD using TMA and an Ar/O_2 plasma show a low WVTR in the range of $10^{-6}\,gm^{-2}d^{-1}$ at room temperature. The saturation in TMA dose and plasma exposure has been verified with a constant growth per cycle of $(0.17\pm0.02)\,nm$ at a low temperature of 75°C, resulting in smooth, dense alumina films ($2.5\,gcm^{-3}$). For water-based processes, ALD type growth could only be shown for deposition temperatures of 100 °C and above. Along with an increase of layer density, the WVTR decreased from $7\times10^{-4}\,gm^{-2}d^{-1}$ (at 60 °C and 60% rH) at a deposition temperature of 75°C down to $5\times10^{-5}\,gm^{-2}d^{-1}$ (at 60 °C and 60% rH) at elevated growth temperatures of 150°C. Using the activation energy of 62 kJ/mol for the temperature dependence of the water permeation process, a WVTR of $4\times10^{-6}\,gm^{-2}d^{-1}$ at RT has been extrapolated.

Furthermore, the growth of tin oxide thin films via spatial ALD at atmospheric pressure using TDMASn and various oxidants (Ar/O_2 plasma, ozone, water) at a process temperature between 80 and 165°C is reported. The self-limited ALD growth characteristics are verified with respect to TDMASn and the Ar/O_2 plasma (or ozone) dose resulting in a GPC of 0.16 and 0.11 nm for 80 and 150°C, respectively. In sharp contrast to processes based on plasma or ozone as oxidant, water-based SnO_x layers exhibit only very low electrical conductivity ($10^{-3}\,(\Omega cm)^{-1}$). Atmospheric pressure oxygen plasma or ozone are shown to afford layers with an electrical conductivity up to $10^2\,(\Omega cm)^{-1}$ (carrier mobility: $4.7\,cm^2V^{-1}s^{-1}$, carrier density: $2\times10^{20}\,cm^{-3}$). At the same time these layers provide water vapor transmission rates as low as $7\times10^{-4}\,gm^{-2}d^{-1}$ (at 60°C and 60% rH). Water-based SnO_x even show a WVTR of $1\times10^{-5}\,gm^{-2}d^{-1}$ (at 60°C and 60% rH), which makes SnO_x grown by atmospheric pressure spatial ALD a serious competitor to Al_2O_3, which is still the most famous metal oxide in terms of barrier properties. As such, SnO_x is used to form an excellent hybrid AZO/SnO_x electron extraction layer and permeation barrier that limits the ingress of moisture into the perovskite solar cells. Most significantly, the ALD-based SnO_x layer simultaneously forms a shield that protects constituents of the cell against corrosive halide-containing perovskite decomposition products. The resulting perovskite solar cells based on the roll-to-roll compatible ALD layer show stable characteristics beyond 1000 h in ambient air and over 3000 h at elevated temperatures (60°C).

The influence of the deposition speed on the thin film growth in spatial ALD is investigated. Experimentally, saturated ALD growth has been shown at a substrate velocity up to 75mm/s (i.e. 4.5m/min), strongly depend on the dose of the precursors used, respectively. Gas flow simulations reveal, that the growth in spatial ALD is not limited by development of a boundary layer above the substrate, but by the amount of precursor

supplied to the repective precursor delivery zone. The introduction of spatial ALD at atmospheric pressure paves the way to the future roll-to-roll manufacturing of electronic devices like stable perovskite solar cells. In addition spatial plasma assisted ALD is rendered as an excellent candidate for the continuous manufacturing of transparent and conductive gas permeations barriers based on SnO_x. The use of plasma ALD instead of water-based ALD enables the deposition of thin films with electrical conductivities five orders of magnitude higher (for SnO_x) as well as with enhanced barrier properties (one order of magnitude in WVTR) at low deposition temperatures (Al_2O_3).

Future prospects

This work reports on conductive and non-conductive barrier layers which could compete with their low-pressure ALD analogous. The development done in this work is in parallel with those in science and industry. As a matter of that, spatial ALD approaches industrial fabrication as roll-to-roll processing comes into the market in future applications. In addition, spatial ALD does not only allow for the deposition of metal oxides, but also of metals (e.g. Ar or Cu).[132] First reports on metal ALD date back to 2011.[212,213] Its principle is strongly connected to the use of reducing plasmas, which enable the removal of ligands from the metal precursor molecules, leaving pure metal atoms at the surface. This reaction could also be described in a self-limiting ALD process. Most common candidates for metal ALD are silver and an copper, which deposition in spatial ALD would broaden the roll-to-roll of electrical devices dramatically. First attempts of metal ALD were also done in the course this work, revealing that the percolation of the metal film i.e. the growth of continuous thin films instead of single cluster-like island is of special importance.[214]

Beyond the additional character of ALD growth, spatial atomic layer etching is proposed.[215,216] In parallel to an expanded pool of material systems, the possibility to etch thin films in closed roll-to-roll processing would fundamentally shorten the processing times and probably lower the cost of the final devices. As reports on ALE are still very limited, an exponential growth in scientific and technological output like ALD witnessed in mid-1990s, could be possible.[217] Several parallels are drawn with the more mature technology of ALD from which lessons and concepts are extracted to the field of ALE. As a matter of that, the development of ALD and its challenges in the last years, could be be beneficial for advancing the field of atomic layer etching.[218] Therefor, this thesis could draw possible lessons also for the roll-to-roll realization of ALE at

atmospheric pressure. Actually, first combined etching and deposition processing in a all-spatial concept including is already proposed in 2015.[219]

A

Appendix

A.1 Double-coating in water-based spatial ALD

Water-based ALD at low temperature shows special characteristics, mainly dependent on the high sticking coefficient of water. In spatial ALD this phenomenon either leads to no observable saturation (e.g. for the TMA/H_2O process) or to a special kind of *double-coating*. In this case, *double-coating* expresses the physical deposition of two ALD cycles instead of just one, even though only one cycle as been conducted intetionally. *Double-coating* was found for the TMDASn/H_2O process at low deposition in the spatial ALD. Saturation behavior in the TMDASn/H_2O process at 80° deposition temperature are shown in Figure A.1a. Obviously, the GPC does not saturate at the expected value of 0.15-0.16 nm for a simple TDMASn/H_2O arrangement in the ALD head. Instead, a saturation in GPC at 0.30 nm can be found, linked with a fixed refractive index of 1.88, comparable to these found in single coated Al_2O_3. Note that at a fixed water dose (8 sccm N_2 flow through the water bubbler) the saturated GPC does not shift when increasing the TDMASn dose (i.e. the flow of N_2 through the TDMASn bubbler), see Figure A.1b.
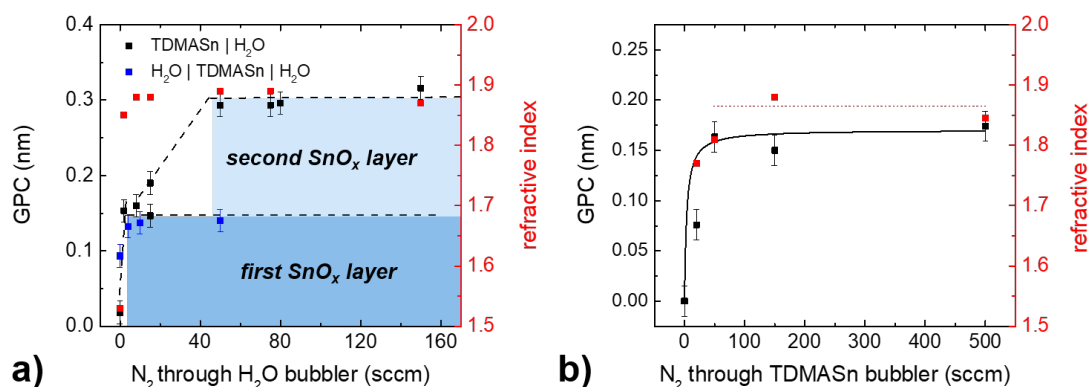
Figure A.1.: Saturation behavior in the TMDASn/H_2O process at 80°C deposition temperature. a) Enhancement of the water dose. b) Enhancement of the TDMASn dose

Due to the observation that the GPC is extended (or even doubled) predominantly at the left side of the substrate, it has to be assumed, that there is a second (artificial) water cycle present at the left side of the ALD head (directly after the TDMASn slot). As this double-coating is observed at high water flow rates, it is believed that the water inlet is the water source for the second oxidation step instead of the outer ambient air in the glove box.

This water reservoir can be understood by the high sticking coefficient of water at low temperatures[53][150] or the a water remaining in the exhaust system of the lower ALD head, leading to the additional ALD cycle. This mechanism is depicted schematically in Figure A.2. Furthermore, this scenario can be simulated by changing the precursor arrangement to H_2O/TDMASn/H_2O. Here, the second oxidation step is added intentionally. As a matter of fact, this setup provides two ALD cycles by the back and forth movement of the table. As shown in Figure A.1a the GPC saturates at 0.15 nm. Note that doubling the amount of purge does not reduce the effect of double coating dramatically. All in all, this phenomenon is strictly linked with low deposition temperatures and high amounts of precursors, typically water. Plasma based process did not show any kind of double coating, even at 80°C.
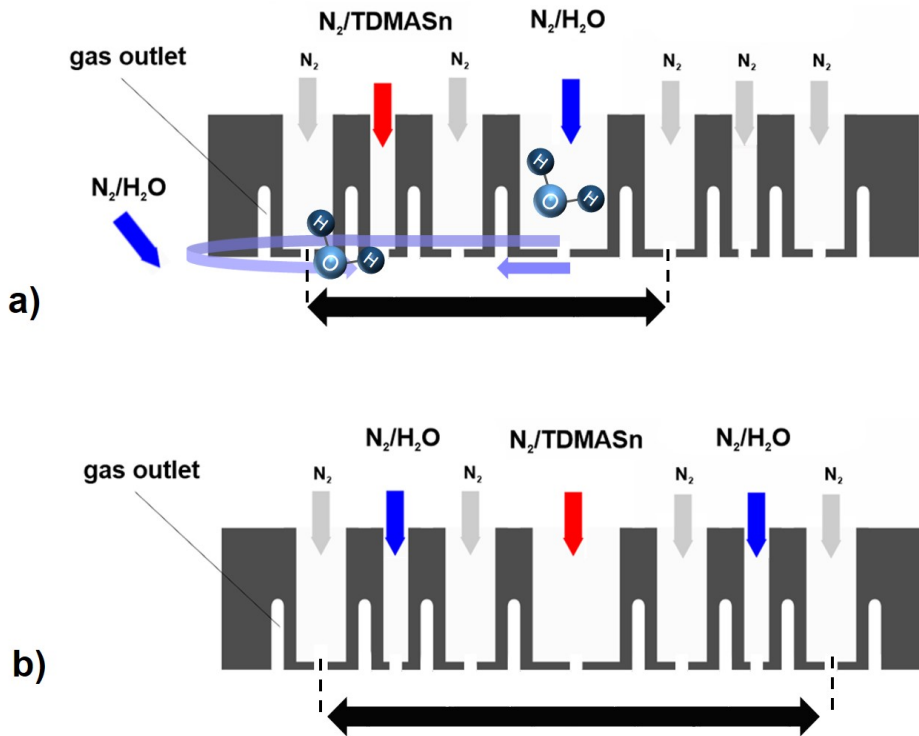
Figure A.2.: Schematic principle of double coating in the TMDASn/H$_2$O process. a) Residual water from the outside or from the inside of the ALD head lead to increased growth at the left side of the substrates. b) The second water cycle is added intentionally by changing the precursor arrangement. The black arrow represents the total width of the substrate movement.

A.2 Al$_2$O$_3$/Bectron multilayer barrier films

3 In fact, metal oxide thin films provide high-quality barriers with an intrinsic WVTR in the range of 10^{-4} gm^{-2}d^{-1} but they suffer from local degradation due to moisture and oxygen trough single macroscopic defects. Additional sealing by organic interlayers promises not only high intrinsic, but also high integral barrier properties. Integral encapsulation is used in terms of the enhancement of the area of encapsulation. Therefore, the barrier properties are not only provided in a small (2×2mm^2 wide) region, but in dimension of several cm^2. Alternating inorganic/organic multilayers lead to very long diffusion pathways by sealing defects which span the entire thickness of a single inorganic layer (e.g. Al$_2$O$_3$).[220,221] Very low WVTR are achieved with metal oxide nanolaminates (e.g Al$_2$O$_3$/ZrO$_2$). The overall barrier properties of these nanolaminates are based on the same phenomena.[14] Organic interlayers were deposited by spin coating *Bectron DP8441 VP* (by *ELANTAS*). *Bectron DP8441 VP* is an acrylate, whose viscosity was de-

signed to be 600 mPas. As the organic *Bectron* films were still wet after spin-coating, an additional drying process is necessary. Wetting could be achieved by UV-exposure or the heating in an oven. 20 min at 150°C lead to wet organic films, which do not show any damage after scratching the sample intentionally. Figure A.3a shows the film thickness of *Bectron* vs. spin coating roration speed on glass and on metal oxide surfaces. Resulting film thicknesses were measured to be between 4000 and 5000 nm. As the resulting film thickness is not only depended on the spin coating rotation speed, but also on the viscosity of the feed material, a further dilution with isopropanol or ethanol was required to achieve thin films with film thickness less than one micrometer. Thereby, *Bectron* films with a thickness of 20 nm were realized.
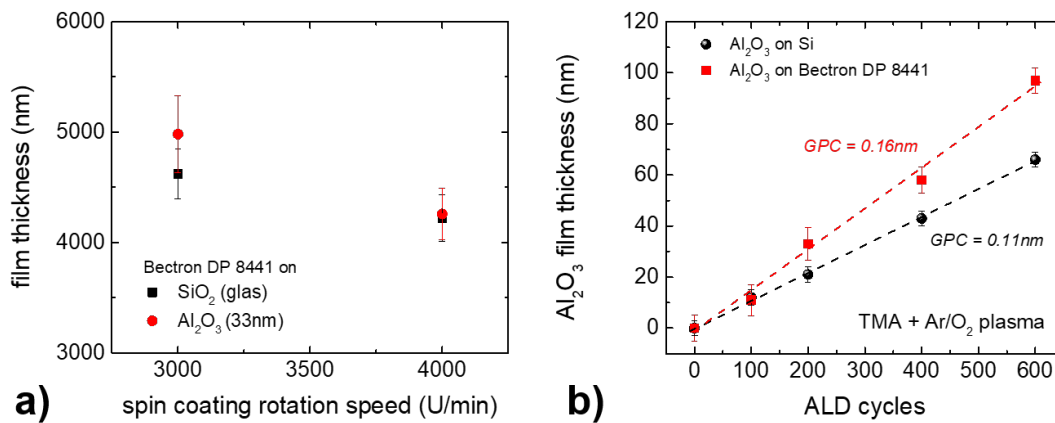
Figure A.3.: *Bectron* spin coating on ALD-Al_2O_3 and glas (a) and ALD growth on *Bectron* films and silicon(b). The Al_2O_3 is deposited in a spatial based APP ALD process at 100°C with a substrate speed of v = 20 mm/s.

To fabricate Al_2O_3/*Bectron* multilayers the respective growth on its counterpart has to be studied. The film thickness of spin coated *Bectron* on ALD layers as well as film thickness of Al_2O_3 films on the organic is shown in Figure A.3. Here, no difference could be found between an ALD film and a glass as substrate for the spin coating process. The other way round, Al_2O_3 on *Bectron* show somewhat higher growth rate (0.16 nm) compared to its growth on silicon substrates (0.11 nm). Additional growth could be explained by the presence of residual water in the *Bectron* film, which is diffusing to its surface during the ALD process. Probably further optimization of the wetting process is necessary to bring both growth rates into line. To evaluate the barrier properties of the Al_2O_3/ *Bectron* multilayers different film designs were deposited and its WVTR measured via the optical Ca-test. As the deposition of *Bectron* is based on a liquid solution process, its deposition could not take place on the calcium sensors. Instead, the mul-

tilayers were deposited on polymer substrates on which Ca-sensors were evaporated and encapsulation with a Al$_2$O$_3$/TiO$_2$ nano laminates (with low-pressure batch ALD), compare subsection 4.1.3. Multilayers with one and two *Bectron* interlayers were fabricated. Accordingly, two and three layers of Al$_2$O$_3$ (TMA and water at 100°C in spatial atmospheric pressure ALD) were applied. For comparison, the sum of the thickness of all metal oxide sub layers was set to 100 nm.
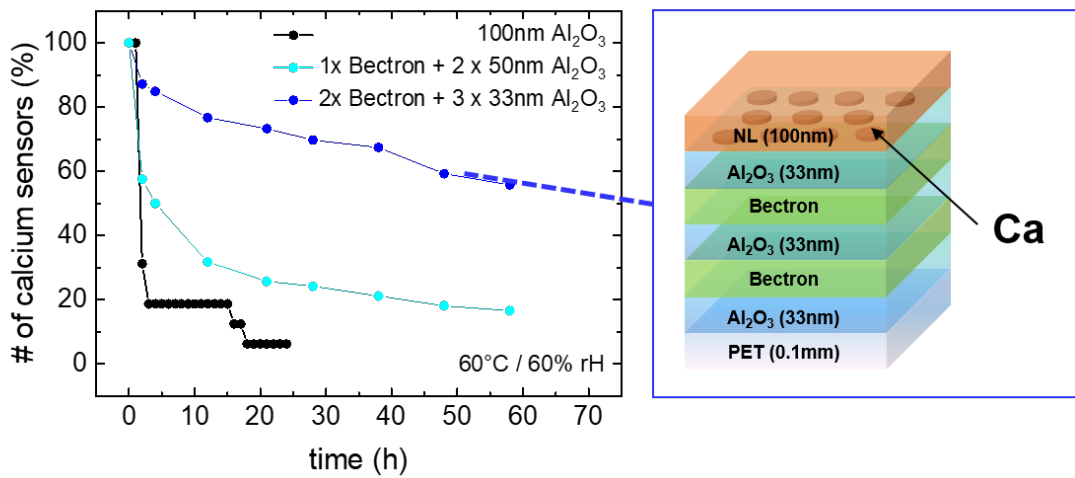
Figure A.4.: The number of calcium sensors vs. time represents the enhancement of the integral WVTR achieved by additional organic-inorganic multilayers. Different Al$_2$O$_3$/*Bectron* multilayer were deposited on PET and its WVTR were measured via the optical Ca-Test. Depicted are the numbers of calcium sensors which show are fully-degraded. Top-encapsulation layer (NL) was deposited by low pressure ALD (Al$_2$O$_3$/TiO$_2$ nanolaminate). The *Bectron* thickness could be estimated to be 2.4 μm.

Figure A.4 shows the number of faultless calcium sensors vs. time stored at 60°C and 60% r.H. For all barriers an intrinsic WVTR of 1×10^{-6}gm^{-2}d^{-1} was determined. Therefore, the intrinsic barrier properties are not influenced by the organic interlayers. But, the integral WVTR (represented by the number of intact calcium sensors) is strongly depended on the number of interlayers. While the number of Ca sensors with a single 100 nm Al$_2$O$_3$ encapsulation (on PET) degrades in the first 20 h to 5% of its initial state, the integration of one organic interlayer (together with two 50 nm thick Al$_2$O$_3$layers) leads to the conservation 20% of the Ca sensors after 60 h. Two *Bectron* interlayers even lead to 60% of failure-free Ca sensors after 60 h. Note that the intrinsic WVTR of a single layer of *Bectron* can not be estimated due to its incompatibility with calcium. Nevertheless, it can be assumed that its intrinsic WVTR is significantly higher than that of

Al$_2$O$_3$ layers as its multiple insertion into the stack does not change the overall intrinsic WVTR. As of that, the overall intrinsic WVTR is still dominated by the metal oxide barrier. The improvement of the integral WVTR could be explained by the encapsulation of particle or pinhole defects inside the multilayer system. Note that the overall high failure rate is a result of fabrication on (flexible) PET substrate. On the other head, the integral WVTR of the top-encapsulation layer cannot be optimized by the number of organic layers underneath. Futhermore, three organic interlayers would minimize the Al$_2$O$_3$ sub-layer thickness. Here, at least 20-30 nm are necessary to guarantee sufficient barrier quality (WVTR = 1×10^{-6} gm^{-2}d^{-1}).[1,222]

A.3 Further details on perovskite solar cells

The statistics of perovskite solar cell based SnO_x deposited by spatial ALD at atmospheric pressure and batch-based low pressure ALD are shown in Figure A.5. 15 and 11 devices are measured, respectively.

Figure A.6 shows the Perovskite solar cell characteristics at elevated temperature (60°C / N_2 atmosphere). Figure A.7 depicts the solar cell characteristics vs. ALD deposition temperature for spatial atmospheric pressure ALD and batch-based low pressure ALD.
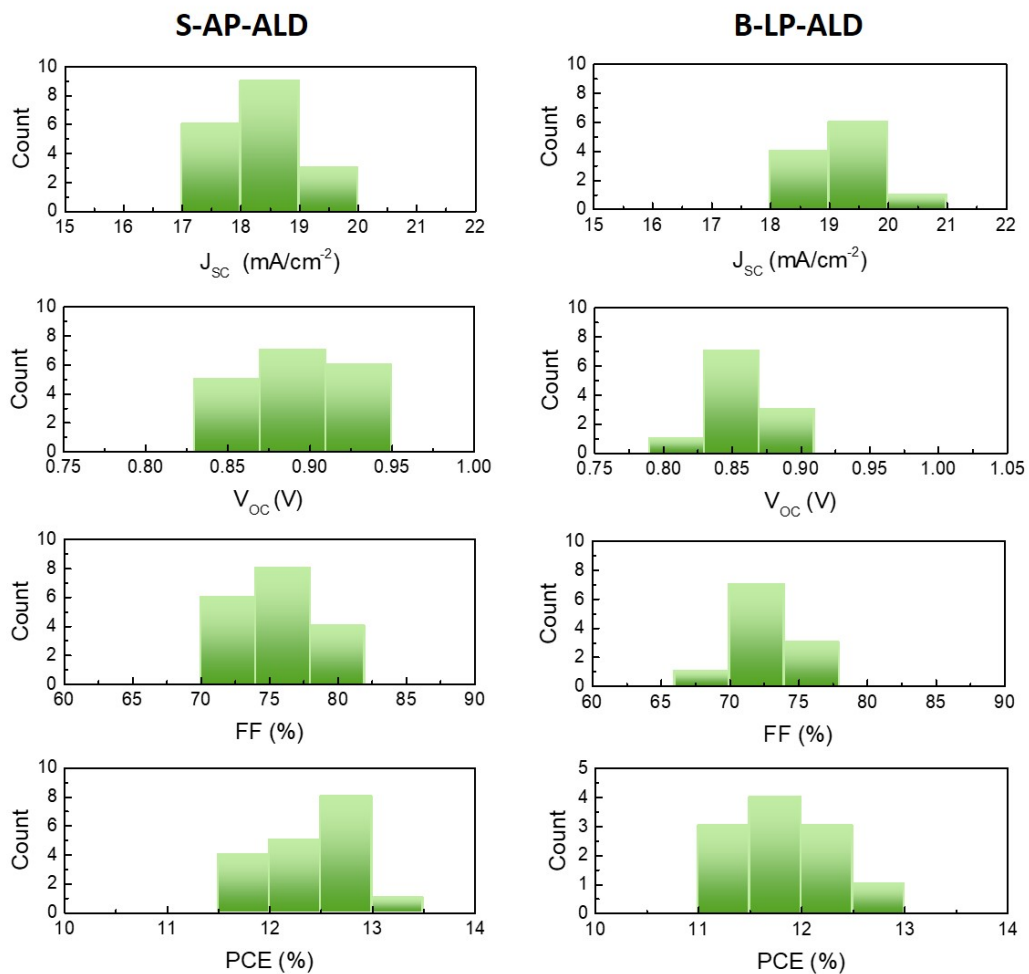
Figure A.5.: Statistical PSC characteristics comparing PSCs built with Spatial atmospheric pressure ALD (S-AP-ALD) (15 devices) and a low pressure batch ALD (B-LP-ALD) (11 devices). All current density values have been derived from EQE measurements.
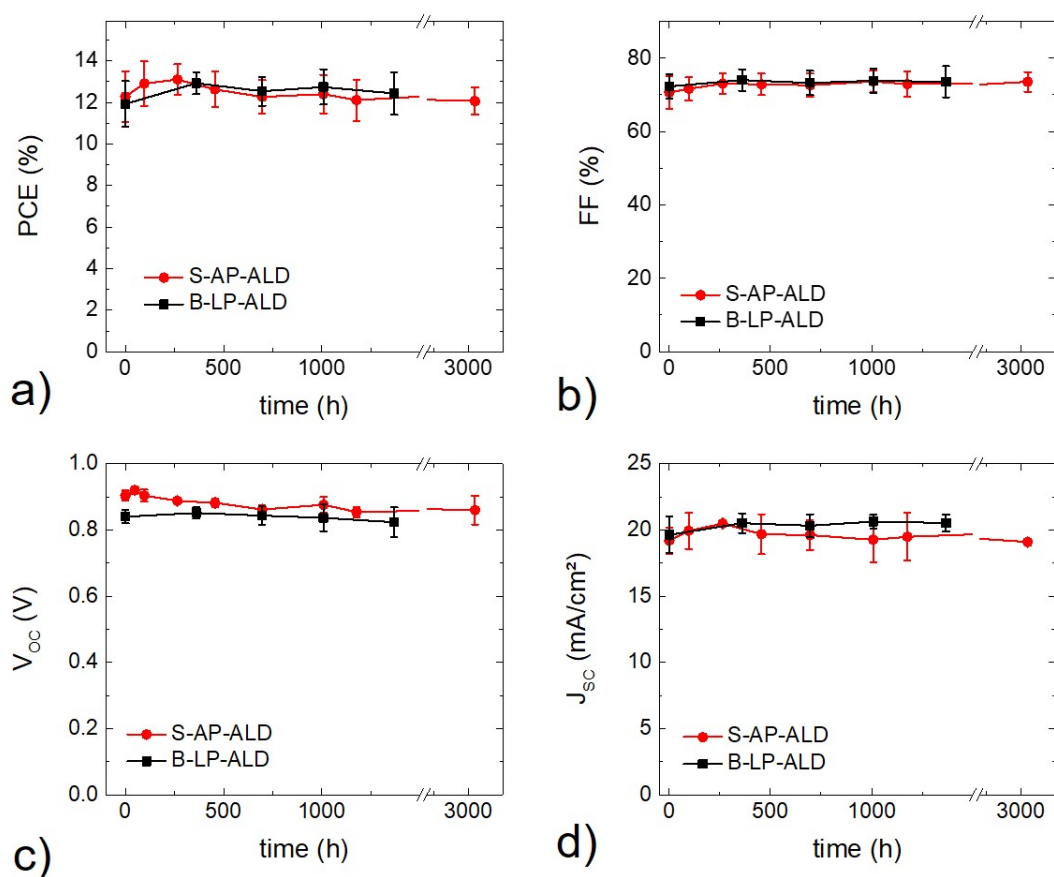
Figure A.6.: Perovksite solar cell characteristics at elevated temperature (60°C / N_2 atmosphere, 5 devices): a) PCE, b) filling factor, c) open circuit voltage, d) short circuit current) vs. time of storage.
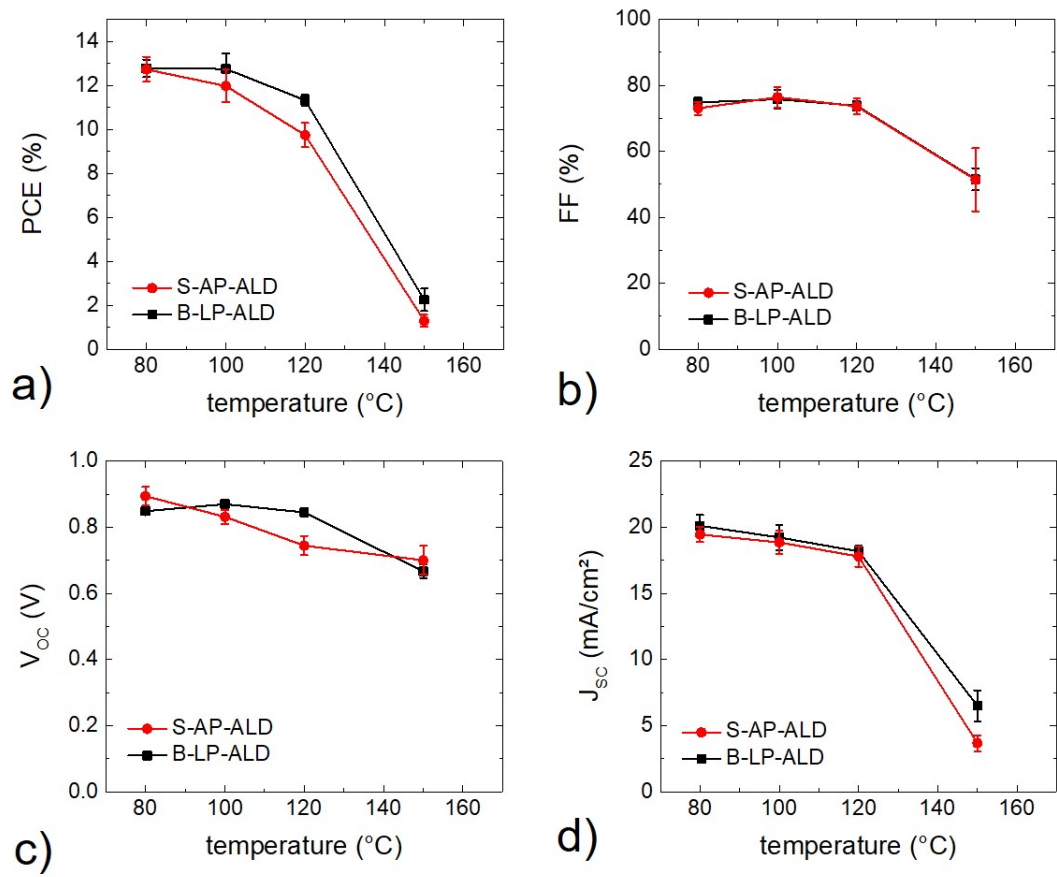
Figure A.7.: Perovskite solar cell characteristics for PSCs with SnO_x from spatial and low pressure batch-based ALD at different deposition temperatures.

A.4 Implementation of the simulations

In this section the implementation of differential equations in OpenFOAM and the reactingFoam solver are roughly discussed. Further information about the implementation and the source code of the simulations used in this work are shown in Ref.[152] OpenFoam is a C++ library, which is used to build solvers like the reactingFoam solver for different types of numerical problems. OpenFOAM is based on the finite volume method. The physical equations are coded in differential form, as seen below in Listing A.1, which is depicting the standard transport equation of mass.

```
fvScalarMatrix YiEqn
(
[1.]      fvm::ddt(rho, Yi)
[2.]      + mvConvection->fvmDiv(phi, Yi)
[3.]      - fvm::laplacian(turbulence->muEff(), Yi)
==
[4.]      reaction->R(Yi)
[5.]      + fvOptions(rho, Yi)
);
```

Listing A.1: Code of the transport of mass equation defined in OpenFoam. [1]: time derivation of the concentration of species [2] Term of convection of mass [3] Diffusive term in the transport equation [4] Generation of species [5] Additional term (often set to zero).

The convection term of the transport equation is further defined as shown in Listing A.2.

```
tmp<fv::convectionScheme<scalar> > mvConvection
(
fv::convectionScheme<scalar>::New
(
mesh,
fields,
phi,
mesh.divScheme("div(phi,Yi_hs)")
)
);
```

Listing A.2: Convection term of the transport equation defined in OpenFoam

```
type                    codedMixed;
```

```
refValue                    uniform0;
refGradient                 uniform0;
valueFraction    uniform1;
redirectType     catalyticSurface;//BC–Name


code
#{

//thesevaluesneedtobeadapted:

constintnumberCells=1360;
constdoublesubstrateLength=13e−2;//[m]
constdoublemoleculesPerMol=6.022e23;//[1/mol]
constdoublemolWeight=72.09e−3;//[kg/mol]
constdoublesorptionSights=8.16e18;//[reactionsights/m^2]


//Lookuppatchfieldsdirectly:

constfvPatch&boundaryPatch=patch();
constvectorField&u=
this−>patch().lookupPatchField<volVectorField,scalar>("U");
constscalarField&gasPatch=
this−>patch().lookupPatchField<volScalarField,scalar>("gasD");
constscalarField&muEff=
this−>patch().lookupPatchField<volScalarField,scalar> \\
("thermo:mu");
constscalarField&densityMix=
this−>patch().lookupPatchField<volScalarField,scalar>("rho");


//InitializingBuffers:

staticdoublesumMolecules[numberCells]={};
staticdoublesurfaceConzentration=0;
staticdoublej=0;
staticdoublemassPerDepth=0;
staticdoublemodulo=0;
staticdoublemodulo2=0;
```

```
staticinti=0;
staticintplatzhalter=0;
staticintplatzhalter2=0;
platzhalter=this->db().time().value()/((substrateLength/ \\
numberCells)
/u[0][0]);
modulo=this->db().time().value()-\\
(platzhalter*((substrateLength/numberCells)
/u[0][0]));

platzhalter2=this->db().time().value()/1e-3;
modulo2=this->db().time().value()-platzhalter2*1e-3;

Info<<"TIME:"<<this->db().time().value()<<nl;
forAll(gasPatch,faceI)
{
surfaceConzentration=gasPatch[faceI];
if(surfaceConzentration<1&&surfaceConzentration<this->
patchInternalField()()[faceI]
&&(sumMolecules[faceI])/(sorptionSights)<1)
{
j=muEff[faceI]
*(this->patchInternalField()()[faceI]-surfaceConzentration)*0.5
*this->patch().deltaCoeffs()[faceI];//[kg/m^2s]
massPerDepth=
j*this->db().time().deltaTValue();//[kg/m^2]

sumMolecules[faceI]+=
massPerDepth*moleculesPerMol/molWeight;//[1/m^2]
surfaceConzentration=
(sumMolecules[faceI])/(sorptionSights);//[1]

if(surfaceConzentration<1)
{
this->refValue()[faceI]=
this->patchInternalField()()[faceI]*surfaceConzentration;
if(modulo2<this->db().time().deltaTValue())
```

```
{
Info <<"face"<<faceI <<"="<<surfaceConzentration <<nl ;
}
}
else
{
this −>refValue ()[ faceI ]=this −>patchInternalField ()()[ faceI ];
if (modulo2<this −>db (). time (). deltaTValue ())
{
Info <<"face"<<faceI <<"="<<surfaceConzentration <<nl ;
}
}
}
else
{
this −>refValue ()[ faceI ]=this −>patchInternalField ()()[ faceI ];
if (modulo2<this −>db (). time (). deltaTValue ())
{
Info <<"face ∗"<<faceI <<"="<<surfaceConzentration <<nl ;
}
}
}
```

Listing A.3: Source code for the simulation of surface sites in OpenFoam

```
/*———————————————————*–C++–*————————————————*\
|=========                |                        |
|\\        /        F ield  |OpenFOAM:TOSCFDT       |
| \\      /         O peration  |Version :3.0.1     |
|  \\    /          A nd    |Web:www.OpenFOAM. org  |
|   \\/             M anipulation  |                |
\*—————————————————————————————————————*/
FoamFile
{
version2 .0;
formatascii ;
classdictionary ;
location "system ";
```

```
objectfvSchemes;
}
//*******************************//
ddtSchemes
{
defaultEuler;
}
gradSchemes
{
defaultGausslinear;
}
divSchemes
{
defaultnone;
div(phi,U)GausslimitedLinearV1;
div(phi,Yi_h)GaussmultivariateSelection
{
gasAlimitedLinear011;
gasBlimitedLinear011;
gasClimitedLinear011;
gasDlimitedLinear011;
gasElimitedLinear011;
gasFlimitedLinear011;
gasGlimitedLinear011;
hlimitedLinear1;
};
div(phi,K)GausslimitedLinear1;
div(phid,p)GausslimitedLinear1;
div(phi,epsilon)GausslimitedLinear1;
div(phi,k)GausslimitedLinear1;
div(((rho*nuEff)*dev2(T(grad(U))))) Gausslinear;
}
laplacianSchemes
{
defaultGausslinearorthogonal;
}
```

```
interpolationSchemes
{
defaultlinear;
}
snGradSchemes
{
defaultorthogonal;
} //***********************************************//
```

Listing A.4: Discretization schemes used in OpenFoam for defining the boundary conditions in the Spatial ALD.

Publications

1. L. Hoffmann, K. O. Brinkmann, J. Malerczyk, D. Rogalla, T. Becker, D. Theirich, I. Shutsko, P. Görrn, and T. Riedl:
   Spatial Atmospheric Pressure Atomic Layer Deposition of Tin Oxide as Impermeable Electron Extraction Layer for Perovskite Solar Cells with Enhanced Thermal Stability
   ACS Applied Mater. & Interfaces 10, 6006 (2018).

2. L. Hoffmann, D. Theirich, D. Schlamm, T. Hasselmann, S. Pack, K. O. Brinkmann, D. Rogalla, S. Peters, A. Räupke, H. Gargouri, and T. Riedl:
   Atmospheric pressure plasma enhanced spatial ALD of SnOx as conductive gas diffusion barrier
   J. Vac. Sci. & Technol. A 36, 1, 01A112 (2018).

3. L. Hoffmann, D. Theirich, S. Pack, F. Kocak, D. Schlamm, T. Hasselmann, H. Fahl, A. Raupke, H. Gargouri, T. Riedl:
   Gas Diffusion Barriers Prepared by Spatial Atmospheric Pressure Plasma Enhanced ALD *ACS Appl. Mater. Interfaces, 9 (4), 4171–4176 (2017).*

4. K.O. Brinkmann, J. Zhao, N. Pourdavoud, T. Becker, T. Hu, S. Olthof, K. Meerholz, L. Hoffmann, T. Gahlmann, R. Heiderhoff, M. Oszajca, N. Luechinger, D. Rogalla D., Y. Chen, B. Cheng, T. Riedl:
   Suppressed decomposition of organo-metal halide perovskites by impermeable electron extraction layers in inverted solar cells
   Nature Communications, 7, 13938 (2017).

5. L. Hoffmann, D. Theirich, T. Hasselmann, A. Räupke, D. Schlamm, and T. Riedl:
   Gas permeation barriers deposited by atmospheric pressure plasma enhanced atomic layer deposition
   J. Vac Sci. Technol. A 34, 01A114 (2016)

6. D. Lützenkirchen-Hecht, L. Müller, L. Hoffmann and R. Wagner:
   Analysis of engine motor oils by X-ray absorption and X-ray fluorescence spectroscopies
   X-Ray Spectrom, 43, 221–227 (2014)

Conference contributions

1. L. Hoffmann, K. O. Brinkmann, J. Zhao, T. Hu, D. Schlamm, J. Malerczyk, T. Becker, D. Theirich, S. Olthof, K. Meerholz, H. Gargouri, Y. Chen, B. Cheng, T. Riedl:
   ALD-Tin Oxide as Impermeable Electron Extraction Layers for Temperature Stable Roll-Ro-Roll-Compatible Perovskite Solar Cells
   17th Conference on Atomic Layer Deposition, Denver (USA) (2017)

2. K. Brinkmann, J. Zhao, N. Pourdavoud, T. Becker, T. Hu, S. Olthof, K. Meerholz, L. Hoffmann, T. Gahlmann, R. Heiderhoff, M. Oszajca, N. Luechinger, D. Rogalla, Y. Chen, B. Cheng, T. Riedl:
   Suppressed decomposition of organo-metal halide perovskites by impermeable electron extraction layers in inverted solar cells
   Best Poster awarded at 2016 MRS Fall Meeting & Exhibit, Boston (USA) (2016)

3. L. Hoffmann, D. Theirich, A. Räupke, D. Schlamm, S. Pack, T. Hasselmann, H.Fahl, T. Riedl:
   Conductive SnOx gas diffusion barriers deposited by spatial plasma enhanced ALD
   16th Conference on Atomic Layer Deposition, Dublin (Irland) (2017)

4. L. Hoffmann, D. Theirich, T. Hasselmann, D. Schlamm, A. Räupke, and T. Riedl:
   Gas Permeation Barriers Prepared by Spatial Plasma Enhanced ALD at Atmospheric Pressure
   MRS Fall Meeting, Boston (USA) BB3.11 (2015)

5. L. Hoffmann, D. Theirich, T. Hasselmann, D. Schlamm, A. Räupke, T. Riedl:
   Gas Permeation Barriers Deposited by Atmospheric Pressure Plasma Enhanced ALD
   15th Conference on Atomic Layer Deposition, Portland (USA), 223 (2015)

Supervised student thesis

1. Tobias Schneider: Fluid Dynamics Simulations of a Spatially Separated Atomic Layer Deposition under Atmospheric Pressure, *Master thesis (2017)*

2. Tim Hasselmann: Ultra-dünne Metallschichten mittels plasmaunterstützer Atomlagenabscheidung bei Atmosphärendruck, *Master thesis (2017)*

3. Felix Nauroth: Organische Zwischenschichten für Multibarrieren-Verkapselung von elektronischen Bauelementen, *Bachelor thesis (2016)*

4. Henry Fahl: Spatial ALD auf flexiblen Foliensubstraten, *Bachelor thesis (2016)*

5. Daniel Schlamm: Abscheidung von Multischichten und leitfähigen Schichten mittels Spatial ALD bei Atmosphärendruck, *Master thesis (2016)*

6. Firat Kocak: Entwicklung eines Plasma-ALD-Prozesses bei Niederdruck für die Abscheidung von Aluminiumoxid-Schichten als Wasserdampfbarrieren, *Bachelor thesis (2015)*

7. Sven Pack: Diffusionsbarrieren mittels räumlich separierter Atmosphärendruck ALD, *Bachelor thesis (2015)*

8. Tim Hasselmann: Abscheidung und Charakterisierung von Aluminiumoxid-Schichten auf PET-Folie mittels Plasma-ALD bei Atmosphärendruck für die Verkapselung Organischer Elektronik, *Bachelor thesis (2014)*

Bibliography

[1] L. Hoffmann, D. Theirich, T. Hasselmann, A. Räupke, D. Schlamm, and T. Riedl. Gas permeation barriers deposited by atmospheric pressure plasma enhanced atomic layer deposition. *J. Vac. Sci. Technol. A*, 34(1):01A114, 2016.

[2] L. Hoffmann, D. Theirich, S. Pack, F. Kocak, D. Schlamm, T. Hasselmann, H. Fahl, A. Räupke, H. Gargouri, and T. Riedl. Gas Diffusion Barriers Prepared by Spatial Atmospheric Pressure Plasma Enhanced ALD. *ACS Appl. Mater. Interfaces*, 9(4):4171–4176, 2017.

[3] L. Hoffmann, D. Theirich, D. Schlamm, T. Hasselmann, S. Pack, K.O. Brinkmann, D. Rogalla, S. Peters, A. Räupke, H. Gargouri, and T. Riedl. Atmospheric pressure plasma enhanced spatial atomic layer deposition of SnOx as conductive gas diffusion barrier. *J. Vac. Sci. Technol. A*, 36(1):01A112, 2018.

[4] L. Hoffmann, K.O. Brinkmann, J. Malerczyk, D. Rogalla, T. Becker, D. Theirich, I. Shutsko, P. Görrn, and T. Riedl. Spatial Atmospheric Pressure Atomic Layer Deposition of Tin Oxide as an Impermeable Electron Extraction Layer for Perovskite Solar Cells with Enhanced Thermal Stability. *ACS Appl. Mater. Interfaces*, 10(6):6006–6013, 2018.

[5] Guangda Niu, Wenzhe Li, Fanqi Meng, Liduo Wang, Haopeng Dong, and Yong Qiu. Study on the stability of CH3NH3PbI3 films and the effect of post-modification by aluminum oxide in all-solid-state hybrid solar cells. *J. Mater. Chem. A*, 2(3):705, 2014.

[6] J.M. Frost, K.T. Butler, F. Brivio, C.H. Hendon, M. Van Schilfgaarde, and A. Walsh. Atomistic origins of high-performance in hybrid halide perovskite solar cells. *Nano Lett.*, 14(5):2584–2590, 2014.

[7] W. A. MacDonald, K. Rollins, Du. MacKerron, K. Rakos, R. Eveson, K. Hashimoto, and B. Rustin. Engineered Films for Display Technologies. *Flex. Flat Panel Displays*, pages 11–33, 2005.

[8] P. E. Burrows, V. Bulovic, S. R. Forrest, L. S. Sapochak, D. M. McCarty, and M. E. Thompson. Reliability and degradation of organic light emitting devices. *Appl. Phys. Lett.*, 65(23):2922–2924, 1994.

[9] J.A. Liddle and G.M. Gallatin. Nanomanufacturing: A Perspective. *ACS Nano*, 10(3):2995–3014, 2016.

[10] P.E. Burrows, G.L. Graff, M.E. Gross, P.M. Martin, M. Hall, E. Mast, C. C. Bonham, W.D. Bennett, L.A. Michalski, M.S. Weaver, J.J. Brown, D. Fogarty, and LS. Sapochak. Gas Permeation and Lifetime Tests On Polymer-Based Barrier Coatings. *Int. Symp. Opt. Sci. Technol.*, 4105:75–83, 2001.

[11] L. Moro and R.J. Visser. Barrier Films for Photovoltaics Applications. *Org. Photovoltaics Mater. Device Physics, Manuf. Technol.*, pages 491–510, 2009.

[12] M. Knez, K. Nielsch, and L. Niinistö. Synthesis and surface engineering of complex nanostructures by atomic layer deposition. *Adv. Mater.*, 19(21):3425–3438, 2007.

[13] J. Meyer, D. Schneidenbach, T. Winkler, S. Hamwi, T. Weimann, P. Hinze, S. Ammermann, H.-H. Johannes, T. Riedl, and W. Kowalsky. Reliable thin film encapsulation for organic light emitting diodes grown by low-temperature atomic layer deposition. *Appl. Phys. Lett.*, 94(23):233305, 2009.

[14] J. Meyer, H. Schmidt, W. Kowalsky, T. Riedl, and A. Kahn. The origin of low water vapor transmission rates through Al2O3/ZrO2 nanolaminate gas-diffusion barriers grown by atomic layer deposition. *Appl. Phys. Lett.*, 96(24):243308, 2010.

[15] S. Franke, M. Baumkötter, C. Monka, S. Raabe, R. Caspary, H.H. Johannes, W. Kowalsky, S. Beck, A. Pucci, and H. Gargouri. Alumina films as gas barrier layers grown by spatial atomic layer deposition with trimethylaluminum and different oxygen sources. *J. Vac. Sci. Technol. A Vacuum, Surfaces, Film.*, 35(1):01B117, 2017.

[16] R.L. Puurunen. A short history of atomic layer deposition: Tuomo Suntola's atomic layer epitaxy. *Chem. Vap. Depos.*, 20(10-12):332–344, 2014.

[17] S.M. George. Atomic layer deposition: an overview. *Chem. Rev.*, 110(1):111–31, 2010.

[18] D.H. Levy, D. Freeman, S.F. Nelson, P.J. Cowdery-Corvan, and L.M. Irving. Stable ZnO thin film transistors by fast open air atomic layer deposition. *Appl. Phys. Lett.*, 92(19):2006–2009, 2008.

[19] D.H. Levy, S.F. Nelson, and D. Freeman. Oxide Electronics by Spatial Atomic Layer Deposition. *J. Disp. Technol.*, 5(12):484–494, 2009.

[20] P. Poodt, A. Lankhorst, F. Roozeboom, K. Spee, D. Maas, and A. Vermeer. High-speed spatial atomic-layer deposition of aluminum oxide layers for solar cell passivation. *Adv. Mater.*, 22(32):3564–7, 2010.

[21] Paul Poodt, David C. Cameron, Eric Dickey, Steven M. George, Vladimir Kuznetsov, Gregory N. Parsons, Fred Roozeboom, Ganesh Sundaram, and Ad Vermeer. Spatial atomic layer deposition: A route towards further industrialization of atomic layer deposition. *J. Vac. Sci. Technol. A Vacuum, Surfaces, Film.*, 30(1):010802, 2012.

[22] Lotus. *TransFlex - ALD*, 2018.

[23] Solliance. Solliance sets world record for roll-to-roll produced perovskite based solar cells with a stabilized efficiency of 12,6%. *Press Release*, pages 2–5, 2017.

[24] T.O. Kääriäinen and D.C. Cameron. Plasma-Assisted Atomic Layer Deposition of Al 2 O 3 at Room Temperature. *Plasma Process. Polym.*, 6(S1):S237–S241, 2009.

[25] S.S. Shin, E.J. Yeom, W.S. Yang, S. Hur, M.G. Kim, J. Im, J. Seo, J.H. Noh, and S.I. Seok. Colloidally prepared La-doped BaSnO3 electrodes for efficient, photostable perovskite solar cells. *Science*, 356(6334):167–171, 2017.

[26] W.S. Yang, B.W. Park, E.H. Jung, N.J. Jeon, Y.C. Kim, D.U. Lee, S.S. Shin, J. Seo, E.K. Kim, J.H. Noh, and S.I. Seok. Iodide management in formamidinium-lead-halide–based perovskite layers for efficient solar cells. *Science*, 356(6345):1376–1379, 2017.

[27] M. Stolterfoht, C.M. Wolff, Y. Amir, A. Paulke, L. Perdigón-Toro, P. Caprioglio, and D. Neher. Approaching the fill factor Shockley–Queisser limit in stable, dopant-free triple cation perovskite solar cells. *Energy Environ. Sci.*, 10(6):1530–1539, 2017.

[28] National Renewable Energy Laboratory (NREL). https://www.nrel.gov/pv/, 2018.

[29] B. Conings, J. Drijkoningen, N. Gauquelin, A. Babayigit, J. D'Haen, L. D'Olieslaeger, A. Ethirajan, J. Verbeeck, J. Manca, E. Mosconi, F.D. Angelis, and

H.G. Boyen. Intrinsic Thermal Instability of Methylammonium Lead Trihalide Perovskite. *Adv. Energy Mater.*, 5(15):1500477, 2015.

[30] F. Xu, T. Zhang, G. Li, and Y. Zhao. Mixed cation hybrid lead halide perovskites with enhanced performance and stability. *J. Mater. Chem. A*, 5(23):11450–11461, 2017.

[31] E.J. Juarez-Perez, Z. Hawash, S.R. Raga, L.K. Ono, and Y. Qi. Thermal degradation of CH3NH3PbI3 perovskite into NH3 and CH3 I gases observed by coupled thermogravimetry–mass spectrometry analysis. *Energy Environ. Sci.*, 9(11):3406–3410, 2016.

[32] G. Niu, X. Guo, and L. Wang. Review of recent progress in chemical stability of perovskite solar cells. *J. Mater. Chem. A*, 3(17):8970–8980, 2015.

[33] Y. Kato, L.K. Ono, M. V. Lee, S. Wang, S.R. Raga, and Y. Qi. Silver Iodide Formation in Methyl Ammonium Lead Iodide Perovskite Solar Cells with Silver Top Electrodes. *Adv. Mater. Interfaces*, 2(13):1500195, 2015.

[34] A. Kim, H. Lee, H.C. Kwon, H.S. Jung, N.G. Park, S. Jeong, and J. Moon. Fully solution-processed transparent electrodes based on silver nanowire composites for perovskite solar cells. *Nanoscale*, 8(12):6308–6316, 2016.

[35] Y. Bai, Q. Dong, Y. Shao, Y. Deng, Q. Wang, L. Shen, D. Wang, W. Wei, and J. Huang. Enhancing stability and efficiency of perovskite solar cells with crosslinkable silane-functionalized and doped fullerene. *Nat. Commun.*, 7:12806, 2016.

[36] K. Domanski, J. Correa-Baena, N. Mine, M. K. Nazeeruddin, A. Abate, M. Saliba, W. Tress, A. Hagfeldt, and M. Grätzel. Not All That Glitters Is Gold: Metal-Migration-Induced Degradation in Perovskite Solar Cells. *ACS Nano*, 10(6):6306–6314, 2016.

[37] G. Grancini, C. Roldán-Carmona, I. Zimmermann, E. Mosconi, X. Lee, D. Martineau, S. Narbey, F. Oswald, F. De Angelis, M. Graetzel, and Mohammad Khaja Nazeeruddin. One-Year stable perovskite solar cells by 2D/3D interface engineering. *Nat. Commun.*, 8:15684, 2017.

[38] E.M. Sanehira, B.J. Tremolet de Villers, P. Schulz, M.O. Reese, S. Ferrere, K. Zhu, L.Y. Lin, J.J. Berry, and J.M. Luther. Influence of Electrode Interfaces on the Stability of Perovskite Solar Cells: Reduced Degradation Using MoOx/Al for Hole Collection. *ACS Energy Lett.*, 1(1):38–45, 2016.

[39] K.A. Bush, C.D. Bailie, Y. Chen, A.R. Bowring, W. Wang, W. Ma, T. Leijtens, F. Moghadam, and M.D. McGehee. Thermal and Environmental Stability of Semi-Transparent Perovskite Solar Cells for Tandems Enabled by a Solution-Processed Nanoparticle Buffer Layer and Sputtered ITO Electrode. *Adv. Mater.*, 28(20):3937–3943, 2016.

[40] J. You, L. Meng, T. Song, T.F. Guo, Y. M. Yang, W.H. Chang, Z. Hong, H. Chen, H. Zhou, Q. Chen, Y. Liu, N. De Marco, and Y. Yang. Improved air stability of perovskite solar cells via solution-processed metal oxide transport layers, 2015.

[41] W. Chen, Y. Wu, Y. Yue, J. Liu, W. Zhang, X. Yang, Han Chen, E. Bi, I. Ashraful, M. Gratzel, and L. Han. Efficient and stable large-area perovskite solar cells with inorganic charge extraction layers. *Science*, 350(6263):944–948, 2015.

[42] K.A. Bush, A.F. Palmstrom, Z.J. Yu, M. Boccard, R. Cheacharoen, J.P. Mailoa, D.P. McMeekin, R.L.Z. Hoye, C.D. Bailie, T. Leijtens, I.M. Peters, M.C. Minichetti, N. Rolston, R. Prasanna, S. Sofia, D. Harwood, W. Ma, F. Moghadam, H.J. Snaith, T. Buonassisi, Z.C. Holman, S.F. Bent, and M.D. McGehee. 23.6%-Efficient Monolithic Perovskite/Silicon Tandem Solar Cells With Improved Stability. *Nat. Energy*, 2(4):1–7, 2017.

[43] T. Suntola and J. Antson. Method for producing compound thin films. *US Pat. 4,058,430*, 1977.

[44] T.S. Suntola, S.G. Lindfors, and A.J. Pakkala. Apparatus for performing growth of compound thin films. *US Pat. 4,389,973*, 1983.

[45] T. Kääriäinen, D. Cameron, M.L. Kääriäinen, and A. Sherman. *Atomic Layer Deposition : Principles, Characteristics, and Nanotechnology Applicatons*. John Wiley & Sons, Ltd, 2 edition, 2013.

[46] C.S. Hwang and C.Y. Yoo. *Atomic layer deposition for semiconductors*. Springer, 2014.

[47] M. Leskelä and M. Ritala. Atomic layer deposition (ALD): from precursors to thin film structures. *Thin Solid Films*, 409(1):138–146, 2002.

[48] R.W. Johnson, A. Hultqvist, and S.F. Bent. A brief review of atomic layer deposition: From fundamentals to applications. *Mater. Today*, 17(5):236–246, 2014.

[49] R.L. Puurunen. Surface chemistry of atomic layer deposition: A case study for the trimethylaluminum/water process. *J. Appl. Phys.*, 97(12):121301, 2005.

[50] Q. Xie, Y.-L. Jiang, C. Detavernier, D. Deduytsche, R.L. Van Meirhaeghe, G.-P. Ru, B.-Z. Li, and X.-P. Qu. Atomic layer deposition of TiO2 from tetrakis-dimethyl-amido titanium or Ti isopropoxide precursors and H2O. *J. Appl. Phys.*, 102(8):083521, 2007.

[51] M.N. Mullings, C. Hägglund, and S.F. Bent. Tin oxide atomic layer deposition from tetrakis(dimethylamino)tin and water. *J. Vac. Sci. Technol. A*, 31(6):061503, 2013.

[52] I. Langmuir. The adsorption of gases on plane surfaces of glass, mica and platinum. *J. Am. Chem. Soc.*, 40(9):1361–1403, 1918.

[53] P.S. Maydannik, A. Plyushch, M. Sillanpää, and D.C. Cameron. Spatial atomic layer deposition: Performance of low temperature H2O and O3 oxidant chemistry for flexible electronics encapsulation. *J. Vac. Sci. Technol. A Vacuum, Surfaces, Film.*, 33(3):031603, 2015.

[54] R.L. Puurunen. Growth Per Cycle in Atomic Layer Deposition: A Theoretical Model. *Chem. Vap. Depos.*, 9(5):249–257, 2003.

[55] A. Niskanen. *Radical Enhanced Atomic Layer Deposition of Metals and Oxides*. PhD thesis, University of Helsinki, 2006.

[56] S.E. Potts, W. Keuning, E. Langereis, G. Dingemans, M.C.M. van de Sanden, and W.M.M. Kessels. Low Temperature Plasma-Enhanced Atomic Layer Deposition of Metal Oxide Thin Films. *J. Electrochem. Soc.*, 157(7):P66, 2010.

[57] M. de Keijser and C. van Opdorp. Atomic layer epitaxy of gallium arsenide with the use of atomic hydrogen. *Appl. Phys. Lett.*, 58(1991):1187–1189, 1991.

[58] M. Mäkelä, T. Hatanpää, K. Mizohata, K. Meinander, J. Niinistö, J. Räisänen, M. Ritala, and M. Leskelä. Studies on Thermal Atomic Layer Deposition of Silver Thin Films. *Chem. Mater.*, 29(5):2040–2045, 2017.

[59] D. J. Hagen, J. Connolly, R. Nagle, I. M. Povey, S. Rushworth, P. Carolan, P. Ma, and M. E. Pemble. Plasma enhanced atomic layer deposition of copper: A comparison of precursors. *Surf. Coatings Technol.*, 230:3–12, 2013.

[60] H.B. Profijt, S.E. Potts, M.C.M. van de Sanden, and W.M.M. Kessels. Plasma-Assisted Atomic Layer Deposition: Basics, Opportunities, and Challenges. *J. Vac. Sci. Technol. A Vacuum, Surfaces, Film.*, 29(5):050801, 2011.

[61] J.W. Lim and S.J. Yun. Electrical Properties of Alumina Films by Plasma-Enhanced Atomic Layer Deposition. *Electrochem. and Solid-State Lett.*, 7(8):F45, 2004.

[62] J. L. van Hemmen, S. B. S. Heil, J. H. Klootwijk, F. Roozeboom, C. J. Hodson, M. C. M. van de Sanden, and W. M. M. Kessels. Plasma and Thermal ALD of Al2O3 in a Commercial 200 mm ALD Reactor. *J. Electrochem. Soc.*, 154(7):G165, 2007.

[63] H.B. Profijt, P. Kudlacek, M.C.M. van de Sanden, and W.M.M. Kessels. Ion and Photon Surface Interaction during Remote Plasma ALD of Metal Oxides. *J. Electrochem. Soc.*, 158(4):G88, 2011.

[64] S.B.S. Heil, E. Langereis, F. Roozeboom, M.C.M. van de Sanden, and W.M.M. Kessels. Low-Temperature Deposition of TiN by Plasma-Assisted Atomic Layer Deposition. *J. Electrochem. Soc.*, 153(11):G956, 2006.

[65] O. Reynolds. An Experimental Investigation of the Circumstances Which Determine Whether the Motion of Water Shall Be Direct or Sinuous, and of the Law of Resistance in Parallel Channels. Osborne. *Proc. R. Soc. L.*, 35:84–99, 1883.

[66] Engineering ToolBox. Gases - Dynamic Viscosity, 2014.

[67] J. Rotta. Experimenteller Beitrag zur Entstehung turbulenter Strömung im Rohr. *Ingenieur-Archiv*, 24(4):258–281, 1956.

[68] N. Rott. Note on the history of the reynolds number. *Annu. Rev. Fluid Mech*, 24(22):1–11, 1990.

[69] D. Hänel. *Molekulare Gasdynamik*. Springer, 2004.

[70] K. Schwister and V. Leven. *Verfahrenstechnik für Ingenieure*. Carl Hanser Verlag, 2014.

[71] R.W. Barber and D.R. Emerson. The influence of Knudsen number on the hydrodynamic development length within parallel plate micro-channels. *Adv. Fluid Mech. IV*, pages 207–216, 2002.

[72] J. R. Welty, C. E. Wicks, R. E. Wilson, and G. L. Rorrer. *Fundamentals of momentum, heat and mass transfer*, volume 13. John Wiley & Sons, 5 edition, 2000.

[73] Y.A. Cengel and J.M. Cimbala. *Fluid Mechanics: Fundamentals and Applications*. McGraw-Hill, 1 edition, 2006.

[74] K.O. Brinkmann, J. Zhao, N. Pourdavoud, T. Becker, T. Hu, S. Olthof, K. Meerholz, L. Hoffmann, T. Gahlmann, R. Heiderhoff, M. F. Oszajca, N. A. Luechinger, D. Rogalla, Y. Chen, B. Cheng, and T Riedl. Suppressed decomposition of organometal halide perovskites by impermeable electron-extraction layers in inverted solar cells. *Nat. Commun.*, 8:13938, 2017.

[75] K. Jung, J.Y. Bae, S.J. Park, S. Yoo, and B.S. Bae. High performance organic-inorganic hybrid barrier coating for encapsulation of OLEDs. *J. Mater. Chem.*, 21(6):1977, 2011.

[76] O.G. Piringer and A.L. Baner. *Plastic Packaging*. Wiley, 2 edition, 2008.

[77] Jay S. Lewis and Michael S. Weaver. Thin-film permeation-barrier technology for flexible organic light-emitting devices. *IEEE J. Sel. Top. Quantum Electron.*, 10(1):45–57, 2004.

[78] A. Behrendt. Gasdiffusionsbarrieren für die organische Optoelektronik - Prozesstechnologie und physikalische Eigenschaften. *Dissertation*, 2016.

[79] R.C. Kwong, M.R. Nugent, L. Michalski, T. Ngo, K. Rajan, Y.J. Tung, M.S. Weaver, T.X. Zhou, M. Hack, M.E. Thompson, S.R. Forrest, and J.J. Brown. High operational stability of electrophosphorescent devices. *Appl. Phys. Lett.*, 81(1):162–164, 2002.

[80] R. Søndergaard, M. Hösel, D. Angmo, T.T. Larsen-Olsen, and F.C. Krebs. Roll-to-roll fabrication of polymer solar cells. *Mater. Today*, 15(1-2):36–49, 2012.

[81] S. Zeman and L. Kubík. Permeability of Polymeric Packaging Materials. *Tech. Sci.*, 10(-1):33–34, 2007.

[82] H. Ibach. *Physics of surfaces and interfaces*. Springer, 2006.

[83] L. Czepirski, M.R. Balys, and E. Komorowska-Czepirska. Some generalization of Langmuir adsorption isotherm. *Internet J. Chem.*, 3:14–1099, 2000.

[84] H. Klumbies. *Encapsulations for Organic Devices and their Evaluation using Calcium Corrosion Tests*. PhD thesis, University of Dresden, 2013.

[85] H. G. Karge and J. Weitkamp. *Adsorption and diffusion*. Springer, 2008.

[86] F.C. Krebs. *Stability and Degradation of Organic and Polymer Solar Cells*. Wiley, 2012.

[87] M. Hanika. Zur Permeation durch aluminiumbedampfte Polypropylen- und Polyethylenterephtalatfolien. *Dissertation*, 2004.

[88] T.-L. Kuo, S. Garcia-Manyes, J. Li, I. Barel, H. Lu, B. J. Berne, M. Urbakh, J. Klafter, and J. M. Fernandez. Probing static disorder in Arrhenius kinetics by single-molecule force spectroscopy. *Proc. Natl. Acad. Sci.*, 107(25):11336–11340, 2010.

[89] B.M. Henry, A.G. Erlat, A McGuigan, C.R.M. Grovenor, G.A.D. Briggs, Y Tsukahara, T Miyamoto, N Noguchi, and T Niijima. Characterization of transparent aluminium oxide and indium tin oxide layers on polymer substrates. *Thin Solid Films*, 382(1-2):194–201, 2001.

[90] Y.G. Tropsha and N.G. Harvey. Activated Rate Theory Treatment of Oxygen and Water Transport through Silicon Oxide /. *J. Phys. Chem. B*, 101(13):2259–2266, 1997.

[91] R.M. Barrer. Diffusion in and through solids. *J. Franklin Inst.*, 232(5):505, 1941.

[92] G.L. Graff, R.E. Williford, and P.E. Burrows. Mechanisms of vapor permeation through multilayer barrier films: Lag time versus equilibrium permeation. *J. Appl. Phys.*, 96(4):1840–1849, 2004.

[93] J. Crank. *the Mathematics of Diffusion*. Oxford University Press, 2 edition, 1975.

[94] S. Cros, S. Guillerez, R.D. Bettignies, N. Lemaître, S. Bailly, and P. Maisse. Relationship between encapsulation barrier performance and organic solar cell lifetime. *Proc. of SPIE*, 7048:70480U, 2008.

[95] S. Franke. *Räumliche Atomlagenabscheidung bei Atmosphärendruck zur Herstellung von Gaspermeationsbarrieren*. PhD thesis, University of Braunschweig, 2017.

[96] G. Nisato, H. Klumbies, J. Fahlteich, L. Müller-Meskamp, P. Van De Weijer, P. Bouten, C. Boeffel, D. Leunberger, W. Graehlert, S. Edge, S. Cros, P. Brewer, E. Kucukpinar, J. De Girolamo, and P. Srinivasan. Experimental comparison of high-performance water vapor permeation measurement methods. *Org. Electron. physics, Mater. Appl.*, 15(12):3746–3755, 2014.

[97] P. F. Carcia, R. S. McLean, M. D. Groner, a. a. Dameron, and S. M. George. Gas diffusion ultrabarriers on polymer substrates using Al2O3 atomic layer deposition and SiN plasma-enhanced chemical vapor deposition. *J. Appl. Phys.*, 106(2):023533, 2009.

[98] D.-S. Han, D.-K. Choi, and J.-W. Park. Al2O3/TiO2 multilayer thin films grown by plasma enhanced atomic layer deposition for organic light-emitting diode passivation. *Thin Solid Films*, 552:155–158, 2014.

[99] H. Chatham. Oxygen diffusion barrier properties of transparent oxide coatings on polymeric substrates. *Surf. Coatings Technol.*, 78(1-3):1–9, 1996.

[100] A.P. Roberts, B.M. Henry, A.P. Sutton, C.R.M. Grovenor, G.A.D Briggs, T. Miyamoto, M. Kano, Y. Tsukahara, and M. Yanaka. Gas permeation in silicon-oxide/polymer (SiOx/PET) barrier films: role of the oxide lattice , nano-defects and macro-defects. *Jounral Membr. Sci.*, 208(1-2):75–88, 2002.

[101] M. Elrawemi, L. Blunt, L. Fleming, F. Sweeney, D. Robbins, and D. Bird. Metrology of Al2O3 Barrier Film for Flexible CIGS Solar Cells. *International Journal of Energy Optimization and Engineering*, 4(4):46–60, 2015.

[102] M.D. Kempe. Modeling of rates of moisture ingress into photovoltaic modules. *Sol. Energy Mater. Sol. Cells*, 90(16):2720–2738, 2006.

[103] G. L. Graff, R. E. Williford, and P. E. Burrows. Mechanisms of vapor permeation through multilayer barrier films: Lag time versus equilibrium permeation. *J. Appl. Phys.*, 96(4):1840, 2004.

[104] S.-H. Jen, B.H. Lee, S.M. George, R.S. McLean, and P.F. Carcia. Critical tensile strain and water vapor transmission rate for nanolaminate films grown using Al2O3 atomic layer deposition and alucone molecular layer deposition. *Appl. Phys. Lett.*, 101(23):234103, 2012.

[105] H.J. Snaith. Estimating the maximum attainable efficiency in Dye-sensitized solar cells. *Adv. Funct. Mater.*, 20(1):13–19, 2010.

[106] F. Hanusch. *Solution Processed Perovskite Solar Cells*. PhD thesis, University of München, 2015.

[107] D.B. Mitzi, C.A. Feild, Z. Schlesinger, and R.B. Laibowitz. Transport, Optical, and Magnetic Properties of the Conducting Halide Perovskite CH3NH3SnI3, 1995.

[108] A. Kojima, Y. Teshima, K.and Shirai, and T. Miyasaka. Organometal Halide Perovskites as Visible-Light Sensitizers for Photovoltaic Cells. *J. Am. Chem. Soc.*, 131(17):6050–6051, 2009.

[109] J.H. Im, C.R. Lee, J.W. Lee, S.W. Park, and N.G. Park. 6.5% Efficient Perovskite Quantum-Dot-Sensitized Solar Cell. *Nanoscale*, 3(10):4088, 2011.

[110] W.E.I. Sha, X. Ren, and W.C.H. Chen, L.and Choy. The efficiency limit of CH3NH3PbI3 perovskite solar cells. *Appl. Phys. Lett.*, 106(22):221104, 2015.

[111] N.G. Park. Perovskite solar cells: An emerging photovoltaic technology. *Mater. Today*, 18(2):65–72, 2015.

[112] M.H. Park, J.Y. Kim, T.H. Han, T.S. Kim, H. Kim, and T.W. Lee. Flexible Lamination Encapsulation. *Adv. Mater.*, 27(29):4308–4314, 2015.

[113] S. Luo and W.A. Daoud. Recent progress in organic–inorganic halide perovskite solar cells: mechanisms and material design. *J. Mater. Chem. A*, 3(17):8992–9010, 2015.

[114] F. Goucher, G. Pearson, M. Sparks, G. Teal, and W. Shockley. Theory and Experiment for a Germanium p-n Junction. *Phys. Rev.*, 81(4):637–638, 1951.

[115] B. Kippelen and J.-L. Bredas. Organic photovoltaics. *Energy & Environmental Science*, 2(3):251, 2008.

[116] K. Zilberberg. *Solution-processed charge extraction interlayers and electrodes for organic solar cells*. PhD thesis, University of Wuppertal, 2014.

[117] K.P. Musselman, C.F. Uzoma, and M.S. Miller. Nanomanufacturing: High-Throughput, Cost-Effective Deposition of Atomic Scale Thin Films via Atmospheric Pressure Spatial Atomic Layer Deposition. *Chemistry of Materials*, 28(23):8443–8452, 2016.

[118] S.F. Nelson, D.H. Levy, L.W. Tutt, and M. Burberry. Cycle time effects on growth and transistor characteristics of spatial atomic layer deposition of zinc oxide. *J. Vac. Sci. Technol. A Vacuum, Surfaces, Film.*, 30(1):01A154, 2012.

[119] A. Illiberi, B. Cobb, A. Sharma, T. Grehl, H. Brongersma, F. Roozeboom, G. Gelinck, and P. Poodt. Spatial Atmospheric Atomic Layer Deposition of InGaZnO for Thin Film Transistors. *ACS Appl. Mater. Interfaces*, 7(6):3671–3675, 2015.

[120] B. Vermang, F. Werner, W. Stals, A. Lorenz, A. Rothschild, J. John, J. Poortmans, R. Mertens, R. Gortzen, P. Poodt, F. Roozeboom, and J. Schmidt. Spatially-separated atomic layer deposition of Al2O3, a new option for high-throughput si solar cell passivation. In *2011 37th IEEE Photovolt. Spec. Conf.*, pages 001144–001149. IEEE, 2011.

[121] P. Poodt, V. Tiba, F. Werner, J. Schmidt, A. Vermeer, and F. Roozeboom. Ultrafast Atomic Layer Deposition of Alumina Layers for Solar Cell Passivation. *J. Electrochem. Soc.*, 158(9):H937, 2011.

[122] F. Werner, W. Stals, R. Görtzen, B. Veith, R. Brendel, and J. Schmidt. High-rate atomic layer deposition of Al2O3 for the surface passivation of Si solar cells. *Energy Procedia*, 8:301–306, 2011.

[123] R.L.Z. Hoye, D. Muñoz-Rojas, D.C. Iza, K.P. Musselman, and J.L. Macmanus-Driscoll. High performance inverted bulk heterojunction solar cells by incorporation of dense, thin ZnO layers made using atmospheric atomic layer deposition. *Sol. Energy Mater. Sol. Cells*, 116:197–202, 2013.

[124] B. Ehrler, K.P. Musselman, M.L. Böhm, F.S.F. Morgenstern, Y. Vaynzof, B.J. Walker, J.L. MacManus-Driscoll, and N.C. Greenham. Preventing interfacial recombination in colloidal quantum dot solar cells by doping the metal oxide. *ACS Nano*, 7(5):4210–4220, 2013.

[125] T. Hirvikorpi, M. Laine, R.and Vähä-Nissi, V. Kilpi, E. Salo, W.M. Li, S. Lindfors, J. Vartiainen, E. Kenttä, J. Nikkola, A. Harlin, and J. Kostamo. Barrier properties of plastic films coated with an Al2O 3 layer by roll-to-toll atomic layer deposition. *Thin Solid Films*, 550:164–169, 2014.

[126] P. Poodt, F. Lankhorst, A.and Roozeboom, K. Spee, D. Maas, and A. Vermeer. High-speed spatial atomic-layer deposition of aluminum oxide layers for solar cell passivation. *Adv. Mater.*, 22(32):3564–7, 2010.

[127] E. Dickey and W.A Barrow. High rate roll to roll atomic layer deposition, and its application to moisture barriers on polymer films. *J. Vac. Sci. Technol. A Vacuum, Surfaces, Film.*, 30(2):021502, 2012.

[128] W.M.M. Kessels and M. Putkonen. Advanced process technologies: Plasma, direct-write, atmospheric pressure, and roll-to-roll ALD. *MRS Bull.*, 36(11):907–913, 2011.

[129] L.F. Hakim, J. Blackson, S.M. George, and A.W. Weimer. Nanocoating Individual Silica Nanoparticles by Atomic Layer Deposition in a Fluidized Bed Reactor. *Chem. Vap. Depos.*, 11(10):420–425, 2005.

[130] A.P. Didden, J. Middelkoop, W.F.A. Besling, D.E. Nanu, and R. van de Krol. Fluidized-bed atomic layer deposition reactor for the synthesis of core-shell nanoparticles. *Review of Scientific Instruments*, 85(1):013905, 2014.

[131] R. Beetstra, U. Lafont, J. Nijenhuis, E.M. Kelder, and J.R. van Ommen. Atmospheric Pressure Process for Coating Particles Using Atomic Layer Deposition. *Chem. Vap. Depos.*, 15(7-9):227–233, 2009.

[132] F.J. van den Bruele, M. Smets, A. Illiberi, Y. Creyghton, P. Buskens, F. Roozeboom, and P. Poodt. Atmospheric pressure plasma enhanced spatial ALD of silver. *J. Vac. Sci. Technol. A Vacuum, Surfaces, Film.*, 33(1):01A131, 2015.

[133] S. Franke, S. Beck, R. Caspary, H.-H. Johannes, A. Pucci, and W. Kowalsky. Silicon stabilized alumina thin films as gas permeation barriers prepared by spatial atomic layer deposition. *MRS Adv.*, 2(17):933–938, 2017.

[134] J.S. Jur and G.N. Parsons. Atomic Layer Deposition of Al 2 O 3 and ZnO at Atmospheric Pressure in a Flow Tube Reactor. *ACS Appl. Mater. Interfaces*, 3(2):299–308, 2011.

[135] M.B.M. Mousa, C.J. Oldham, and G.N. Parsons. Atmospheric Pressure Atomic Layer Deposition of Al2O3 Using Trimethyl Aluminum and Ozone. *Langmuir*, 30(13):3741–3748, 2014.

[136] D. Theirich, R. Müller, K. Zilberberg, S. Trost, A. Behrendt, and T. Riedl. Atmospheric Pressure Plasma ALD of Titanium Oxide. *Chem. Vap. Depos.*, 19(4-6):167–173, 2013.

[137] M. Mousa, C. Oldham, J.S. Jur, and G.N. Parsons. Effect of temperature and gas velocity on growth per cycle during Al2O3 and ZnO atomic layer deposition at atmospheric pressure. *J. Vac. Sci. Technol. A*, 30(January):01A155–01A155, 2012.

[138] K. Sharma, N. Routkevitch, D.and Varaksa, and S.M. George. Spatial atomic layer deposition on flexible porous substrates: ZnO on anodic aluminum oxide films and Al2O3 on Li ion battery electrodes. *J. Vac. Sci. Technol. A Vacuum, Surfaces, Film.*, 34(1):01A146, 2016.

[139] H. Choi, S. Shin, H. Jeon, Y. Choi, J. Kim, S. Kim, S.C. Chung, and K. Oh. Fast spatial atomic layer deposition of Al2O3 at low temperature (<100°C) as a gas permeation barrier for flexible organic light-emitting diode displays. *J. Vac. Sci. Technol. A Vacuum, Surfaces, Film.*, 34(1):01A121, 2016.

[140] K. Ali, K.-H. Choi, and N.M. Muhammad. Roll-to-Roll Atmospheric Atomic Layer Deposition of Al2O3 Thin Films on PET Substrates. *Chem. Vap. Depos.*, 20:380–387, 2014.

[141] Z. Deng, W. He, C. Duan, R. Chen, and B. Shan. Mechanistic modeling study on process optimization and precursor utilization with atmospheric spatial atomic layer deposition. *J. Vac. Sci. Technol. A Vacuum, Surfaces, Film.*, 34(1):01A108, 2016.

[142] A.S. Yersak, Y.C. Lee, J.A. Spencer, and M.D. Groner. Atmospheric pressure spatial atomic layer deposition web coating with in situ monitoring of film thickness. *J. Vac. Sci. Technol. A Vacuum, Surfaces, Film.*, 32(1):01A130, 2014.

[143] A. Illiberi, F. Roozeboom, and P. Poodt. Spatial atomic layer deposition of zinc oxide thin films. *ACS Appl. Mater. Interfaces*, 4(1):268–72, 2012.

[144] Y. Creyghton, A. van der Bruele, A Illiberi, F. Roozeboom, and P. Poodt. Atmospheric pressure plasma enhanced spatial atomic layer deposition. *Phys. Status Solidi RRL Rapid Res. Lett.*, 5(4):165–167, 2011.

[145] S.-Y. Lien, C.-H. Yang, K.-C. Wu, and C.-Y. Kung. Investigation on the passivated Si/Al2O3 interface fabricated by non-vacuum spatial atomic layer deposition system. *Nanoscale Res. Lett.*, 10(1):93, 2015.

[146] D. Muñoz-Rojas, H. Sun, D.C. Iza, J. Weickert, L. Chen, H. Wang, L. Schmidt-Mende, and J.L. MacManus-Driscoll. High-speed atmospheric atomic layer deposition of ultra thin amorphous TiO2 blocking layers at 100 C for inverted bulk heterojunction solar cells. *Prog. Photovoltaics Res. Appl.*, 20(1):6–11, 2012.

[147] R. Chen, J.-L. Lin, W.-J. He, C.-L. Duan, Q. Peng, X.-L. Wang, and B. Shan. Spatial atomic layer deposition of ZnO/TiO2 nanolaminates. *J. Vac. Sci. Technol. A Vacuum, Surfaces, Film*, 34(5):051502, 2016.

[148] M. Aghaee, P.S. Maydannik, P. Johansson, J. Kuusipalo, M. Creatore, T.áš Homola, and D.C. Cameron. Low temperature temporal and spatial atomic layer deposition of TiO2 films. *J. Vac. Sci. Technol. A Vacuum, Surfaces, Film.*, 33:041512, 2015.

[149] M.A. Mione, I. Katsouras, Y. Creyghton, W. van Boekel, J. Maas, G. Gelinck, F. Roozeboom, and A. Illiberi. Atmospheric Pressure Plasma Enhanced Spatial ALD of ZrO2 for Low-Temperature, Large-Area Applications. *ECS Journal of Solid State Science and Technology*, 6(12):N243–N249, 2017.

[150] P. Poodt, R. Knaapen, A. Illiberi, F. Roozeboom, and A. van Asten. Low temperature and roll-to-roll spatial atomic layer deposition for flexible electronics. *J. Vac. Sci. Technol. A Vacuum, Surfaces, Film.*, 30(1):01A142, 2012.

[151] Ingredients Information. *Trimethylaluminum - Material Safety Data Sheet (MSDS)*, 2012.

[152] T. Schneider. Fluid Dynamics Simulation of a Spatially Separated Atomic Layer Deposition under Atmospheric Pressure. Master's thesis, University of Wuppertal, 2017.

[153] H.-E. Wagner, R. Brandenburg, K.V. Kozlov, A. Sonnenfeld, P. Michel, and J.F. Behnke. The barrier discharge: basic properties and applications to surface treatment. *Vacuum*, 71(3):417–436, 2003.

[154] U. Kogelschatz and B. Eliasson. Die Renaissance der stillen elektrischen Entladung. *Phys. J.*, 52(4):360–362, 1996.

[155] G. Nisato, H. Klumbies, J. Fahlteich, L. Müller-Meskamp, P. van de Weijer, P. Bouten, C. Boeffel, D. Leunberger, W. Graehlert, S. Edge, S. Cros, P. Brewer, E. Kucukpinar, J. de Girolamo, and P. Srinivasan. Experimental comparison of high-performance water vapor permeation measurement methods. *Org. Electron.*, 15(12):3746–3755, 2014.

[156] P. F. Carcia, R. S. McLean, M. H. Reilly, M. D. Groner, and S. M. George. Ca test of Al2O3 gas diffusion barriers grown by atomic layer deposition on polymers. *Appl. Phys. Lett.*, 89(3):031915, 2006.

[157] S. Cros, M. Firon, S. Lenfant, P. Trouslard, and L. Beck. Study of thin calcium electrode degradation by ion beam analysis. *Nucl. Instruments Methods Phys. Res. Sect. B*, 251(1):257–260, 2006.

[158] S. Schubert, H. Klumbies, L. Müller-Meskamp, and K. Leo. Electrical calcium test for moisture barrier evaluation for organic devices. *Rev. Sci. Instrum.*, 82(9):094101, 2011.

[159] R. Paetzold, A. Winnacker, D. Henseler, V. Cesari, and K. Heuser. Permeation rate measurements by electrical analysis of calcium corrosion. *Rev. Sci. Instrum.*, 74(12):5147, 2003.

[160] J.A. Bertrand. *Gas Diffusion Barriers Using Atomic Layer Deposition : A New Calcium Test and Polymer Substrate Effects*. PhD thesis, University of Colorado, 2012.

[161] J. A. Bertrand, D. J. Higgs, M. J. Young, and S. M. George. H2O vapor transmission rate through polyethylene naphthalate polymer using the electrical Ca test. *J. Phys. Chem. A*, 117(46):12026–12034, 2013.

[162] P. J. Brewer, B. a. Goody, Y. Kumar, and M. J T Milton. Accurate measurements of water vapor transmission through high-performance barrier layers. *Rev. Sci. Instrum.*, 83(7):075118, 2012.

[163] M.D. Groner, S.M. George, R.S. McLean, and P.F. Carcia. Gas diffusion barriers on polymers using Al2O3 atomic layer deposition. *Appl. Phys. Lett.*, 88(5):51907, 2006.

[164] E. Rutherford. The scattering of α and β particles by matter and the structure of the atom. *Philos. Mag.*, 21(6):669–688, 1911.

[165] S. Rubin, T.O. Passell, and L.E. Bailey. Chemical Analysis of Surfaces by Nuclear Methods. *Anal. Chem.*, 29(5):736–743, 1957.

[166] J. Perrire. Rutherford backscattering spectrometry. *Vacuum*, 37(5):429–432, 1987.

[167] F. Brown and W. D. Mackintosh. The Use of Rutherford Backscattering to Study the Behavior of Ion-Implanted Atoms During Anodic Oxidation of Aluminum: Ar, Kr, Xe, K, Rb, Cs, Cl, Br, and l. *J. Electrochem. Soc.*, 120(8):1096, 1973.

[168] S.B.S. Heil, J.L. van Hemmen, M.C.M. van de Sanden, and W.M.M. Kessels. Reaction mechanisms during plasma-assisted atomic layer deposition of metal oxides: A case study for Al2O3. *J. Appl. Phys.*, 103(10):103302, 2008.

[169] M.D. Groner, F.H. Fabreguette, J.W. Elam, and S.M. George. Low-Temperature Al2O3 Atomic Layer Deposition. *Chem. Mater.*, 16(4):639–645, 2004.

[170] P. Poodt, J. van Lieshout, A. Illiberi, R. Knaapen, F. Roozeboom, and A. van Asten. On the kinetics of spatial atomic layer deposition. *J. Vac. Sci. Technol. A*, 31:01A108, 2013.

[171] G.N. Parsons, S.E. Atanasov, E.C. Dandley, C.K. Devine, B. Gong, J.S. Jur, K. Lee, C.J. Oldham, Q. Peng, J.C. Spagnola, and P.S. Williams. Mechanisms and reactions during atomic layer deposition on polymers. *Coord. Chem. Rev.*, 257(23-24):3323–3331, 2013.

[172] J. Meyer, P. Görrn, F. Bertram, S. Hamwi, T. Winkler, H.-H. Johannes, T. Weimann, P. Hinze, T. Riedl, and W. Kowalsky. Al2O3/ZrO2 Nanolaminates as Ultrahigh Gas-Diffusion Barriers-A Strategy for Reliable Encapsulation of Organic Electronics. *Adv. Mater.*, 21(18):1845–1849, 2009.

[173] L.H. Kim, K. Kim, S. Park, Y.J. Jeong, H. Kim, D.S. Chung, S.H. Kim, and C.E. Park. Al 2 O 3 /TiO 2 Nanolaminate Thin Film Encapsulation for Organic Thin Film Transistors via Plasma-Enhanced Atomic Layer Deposition. *ACS Appl. Mater. Interfaces*, 6(9):6731–6738, 2014.

[174] L.H. Kim, Y.J. Jeong, T.K. An, S. Park, J.H. Jang, S. Nam, J. Jang, S.H. Kim, and C.E. Park. Optimization of Al2O3/TiO2 nanolaminate thin films prepared with different oxide ratios, for use in organic light-emitting diode encapsulation, via plasma-enhanced atomic layer deposition. *Phys. Chem. Chem. Phys.*, 18(2):1042–1049, 2016.

[175] E. Langereis, M. Creatore, S. B. S. Heil, M. C. M. van de Sanden, and W. M. M. Kessels. Plasma-assisted atomic layer deposition of Al2O3 moisture permeation barriers on polymers. *Appl. Phys. Lett.*, 89(8):081915, 2006.

[176] P. Poodt, R. Knaapen, A. Illiberi, F. Roozeboom, and A. van Asten. Low temperature and roll-to-roll spatial atomic layer deposition for flexible electronics. *J. Vac. Sci. Technol. A Vacuum, Surfaces, Film.*, 30(1):01A142, 2012.

[177] P. Kumar, M.K. Wiedmann, C.H. Winter, and I. Avrutsky. Optical properties of Al2O3 thin films grown by atomic layer deposition. *Appl. Opt.*, 48(28):5407–12, 2009.

[178] Z.-Y. Wang, R.-J. Zhang, H.-L. Lu, X. Chen, Y. Sun, Y. Zhang, Y.-F. Wei, J.-P. Xu, S.-Y. Wang, Y.-X. Zheng, and L.-Y. Chen. The impact of thickness and thermal annealing on refractive index for aluminum oxide thin films deposited by atomic layer deposition. *Nanoscale Res. Lett.*, 10(1):46, 2015.

[179] Y. Zhang, Y.-Z. Zhang, D.C. Miller, J.A. Bertrand, S.-H. Jen, R. Yang, M.L. Dunn, S.M. George, and Y.C. Lee. Fluorescent tags to visualize defects in Al2O3 thin films grown using atomic layer deposition. *Thin Solid Films*, 517:6794–6797, 2009.

[180] Y. Leterrier. Durability of nanosized oxygen barrier coatings on polymers. *Progr. Mater. Sci.*, 48:1, 2003.

[181] S.-H. Jen, J.A. Bertrand, and S.M. George. Critical tensile and compressive strains for cracking of Al 2 O 3 films grown by atomic layer deposition. *J. Appl. Phys.*, 109(8):084305, 2011.

[182] V.R. Rai, V. Vandalon, and S. Agarwal. Influence of surface temperature on the mechanism of atomic layer deposition of aluminum oxide using an oxygen plasma and ozone. *Langmuir*, 28(1):350–357, 2012.

[183] ISP Optics. *Sapphire DataSheet*, 2018.

[184] S.E. Potts, H.B. Profijt, R. Roelofs, and W.M.M. Kessels. Room-Temperature ALD of Metal Oxide Thin Films by Energy-Enhanced ALD. *Chem. Vap. Depos.*, 19(4-6):125–133, 2013.

[185] E. Langereis, M. Creatore, S. B S Heil, M. C M Van De Sanden, and W. M M Kessels. Plasma-assisted atomic layer deposition of Al2O3 moisture permeation barriers on polymers. *Appl. Phys. Lett.*, 89(8):28–30, 2006.

[186] V.R. Rai, V. Vandalon, and S. Agarwal. Surface reaction mechanisms during ozone and oxygen plasma assisted atomic layer deposition of aluminum oxide. *Langmuir*, 26(17):13732–5, 2010.

[187] A. C. Dillon, A. W. Ott, J. D. Way, and S. M. George. Surface chemistry of Al2O3 deposition using Al(CH3)3 and H2O in a binary reaction sequence. *Surf. Sci.*, 322(1-3):230–242, 1995.

[188] H. Viirola, L. Niinisto. Controlled growth of tin dioxide thin films by atomic layer epitaxy. *Thin Solid Films*, 249:144–149, 1994.

[189] C. Duecsoe, N.Q. Khanh, Z. Horvath, I. Barsony, M. Utriainen, S. Lehto, M. Nieminen, and L. Niinistö. Deposition of Tin Oxide into Porous Silicon by Atomic Layer Epitaxy. *J. Electrochem. Soc.*, 143(2):683, 1996.

[190] A. Tarre, A. Rosental, A. Aidla, J. Aarik, J. Sundqvist, and A. Hårsta. New routes to SnO2 heteroepitaxy. *Vacuum*, 67(3-4):571–575, 2002.

[191] D. V. Nazarov, N. P. Bobrysheva, O. M. Osmolovskaya, M. G. Osmolovsky, and V. M. Smirnov. Atomic layer deposition of tin dioxide nanofilms: A review. *Rev. Adv. Mater. Sci.*, 40(3):262–275, 2015.

[192] D.-W. Choi, W.J. Maeng, and J.-S. Park. The conducting tin oxide thin films deposited via atomic layer deposition using Tetrakis-dimethylamino tin and peroxide for transparent flexible electronics. *Appl. Surf. Sci.*, 313:585–590, 2014.

[193] J.W. Elam, D.A. Baker, A. J. Hryn, A.B.F. Martinson, M.J. Pellin, and J.T. Hupp. Atomic layer deposition of tin oxide films using tetrakis(dimethylamino) tin. *J. Vac. Sci. Technol. A*, 26(2):244, 2008.

[194] D. Wang, C.and Zhao, C.R. Grice, W. Liao, Y. Yu, A. Cimaroli, N. Shrestha, P.J. Roland, J. Chen, Z. Yu, P. Liu, N. Cheng, R.J. Ellingson, X. Zhao, and Y. Yan. Low-temperature plasma-enhanced atomic layer deposition of tin oxide electron selective layers for highly efficient planar perovskite solar cells. *J. Mater. Chem. A*, 4(31):12080–12087, 2016.

[195] A. Behrendt, C. Friedenberger, T. Gahlmann, S. Trost, T. Becker, K. Zilberberg, A. Polywka, P. Görrn, and T. Riedl. Highly Robust Transparent and Conductive Gas Diffusion Barriers Based on Tin Oxide. *Adv. Mater.*, 27(39):5961–5967, 2015.

[196] J. Heo, S.B. Kim, and R.G. Gordon. Atomic layer deposition of tin oxide with nitric oxide as an oxidant gas. *J. Mater. Chem.*, 22(11):4599, 2012.

[197] J. Heo, A.S. Hock, and R.G. Gordon. Low temperature atomic layer deposition of tin oxide. *Chem. Mater.*, 22(17):4964–4973, 2010.

[198] A.K. Singh, M. Janotti, A.and Scheffler, and C.G. Van De Walle. Sources of electrical conductivity in SnO2. *Phys. Rev. Lett.*, 101(5):055502, 2008.

[199] Ç. Kiliç and A. Zunger. N-type doping of oxides by hydrogen. *Appl. Phys. Lett.*, 81(1):73–75, 2002.

[200] M. Batzill and U. Diebold. The surface and materials science of tin oxide. *Prog. Surf. Sci.*, 79(2-4):47–154, 2005.

[201] S. Baco, A. Chik, and F. Md. Yassin. Study on Optical Properties of Tin Oxide Thin Film at Different Annealing Temperature. *J. Sci. Technol.*, 4:61–72, 2012.

[202] D. won Choi and J.S. Park. Highly conductive SnO2 thin films deposited by atomic layer deposition using tetrakis-dimethyl-amine-tin precursor and ozone reactant. *Surf. Coatings Technol.*, 259(PB):238–243, 2014.

[203] T. Hu, T. Becker, N. Pourdavoud, J. Zhao, K.O. Brinkmann, R. Heiderhoff, T. Gahlmann, Z. Huang, S. Olthof, K. Meerholz, D. Többens, B. Cheng, Y. Chen, and T. Riedl. Indium-Free Perovskite Solar Cells Enabled by Impermeable Tin-Oxide Electron Extraction Layers. *Adv. Mater.*, 29(27):1606656, 2017.

[204] I.S. Kim and A.B.F. Martinson. Stabilizing hybrid perovskites against moisture and temperature via non-hydrolytic atomic layer deposited overlayers. *J. Mater. Chem. A*, 3(40):20092–20096, 2015.

[205] D. Koushik, W.J.H. Verhees, Y. Kuang, S. Veenstra, D. Zhang, M.A. Verheijen, M. Creatore, and R.E.I. Schropp. High-efficiency humidity-stable planar perovskite solar cells based on atomic layer architecture. *Energy Environ. Sci.*, 10(1):91–100, 2017.

[206] M.B.M. Mousa, C.J. Oldham, J.S. Jur, and G.N. Parsons. Effect of temperature and gas velocity on growth per cycle during Al2O3 and ZnO atomic layer deposition at atmospheric pressure. *J. Vac. Sci. Technol. a*, 30(1):01A155–01A155, 2012.

[207] S. Shin, H. Choi, G. Ham, J. Park, J. Lee, H. Choi, S. Lee, H. Kim, and H. Jeon. Effect of scan speed on moisture barrier properties of aluminum oxide using spatial atomic layer deposition. *J. Vac. Sci. Technol. A Vacuum, Surfaces, Film.*, 35(2):021514, 2017.

[208] N. Takagaki, R. Kurose, A. Kimura, and S. Komori. Effect of Schmidt number on mass transfer across a sheared gas-liquid interface in a wind-driven turbulence. *Sci. Rep.*, 6:1–8, 2016.

[209] P. Patnaik. *Handbook of Inorganic Chemicals.* McGraw-Hill, 2003.

[210] A.W. Ott, J.W. Klaus, J.M. Johnson, and S.M. George. Al3O3 thin film growth on Si(100) using binary reaction sequence chemistry. *Thin Solid Films*, 292(1-2):135–144, 1997.

[211] M.D. Groner, J.W. Elam, F.H. Fabreguette, and S.M. George. Electrical characterization of thin Al2O3 films grown by atomic layer deposition on silicon and various metal substrates. *Thin Solid Films*, 413(1–2):186–197, 2002.

[212] M. Kariniemi, J. Niinistö, T. Hatanpää, M. Kemell, T. Sajavaara, M. Ritala, and M. Leskelä. Plasma-Enhanced Atomic Layer Deposition of Silver Thin Films. *Chem. Mater.*, 23(11):2901–2907, 2011.

[213] M. Ritala and M. Leskela. Atomic Layer Deposition of Noble Metals and Their Oxides Jani Ha m. *Chem. Mater.*, 26:786–801, 2014.

[214] A. Mameli, F. van den Bruele, C. K. Ande, M.A. Verheijen, W.M.M. Kessels, and F. Roozeboom. On the Growth, Percolation and Wetting of Silver Thin Films Grown by Atmospheric-Plasma Enhanced Spatial Atomic Layer Deposition. *ECS Trans.*, 75(6):129–142, 2016.

[215] K.J. Kanarik, T. Lill, E. A. Hudson, S. Sriraman, S. Tan, J. Marks, V. Vahedi, and R. A. Gottscho. Overview of atomic layer etching in the semiconductor industry. *J. Vac. Sci. Technol. A*, 33(2):020802, 2015.

[216] G. S. Oehrlein, D. Metzler, and C. Li. Atomic Layer Etching at the Tipping Point: An Overview. *ECS J. Solid State Sci. Technol.*, 4(6):N5041–N5053, 2015.

[217] C. T. Carver, J. J. Plombon, P. E. Romero, S. Suri, T. A. Tronic, and R. B. Turkot. Atomic Layer Etching: An Industry Perspective. *ECS J. Solid State Sci. Technol.*, 4(6):N5005–N5009, 2015.

[218] T. Faraz, F. Roozeboom, H.C.M. Knoops, and W.M.M. Kessels. Atomic Layer Etching: What Can We Learn from Atomic Layer Deposition? *ECS J. Solid State Sci. Technol.*, 4(6):N5023–N5032, 2015.

[219] F. Roozeboom, F. van den Bruele, Y. Creyghton, P. Poodt, and W.M.M. Kessels. Cyclic Etch/Passivation-Deposition as an All-Spatial Concept toward High-Rate

Room Temperature Atomic Layer Etching. *ECS J. Solid State Sci. Technol.*, 4(6):N5067–N5076, 2015.

[220] R. Grover, R. Srivastava, O. Rana, D.S. Mehta, and M.N. Kamalasanan. New Organic Thin-Film Encapsulation for Organic Light Emitting Diodes. *J. Encapsulation Adsorpt. Sci.*, 2011(June):23–28, 2011.

[221] J.D. Affinito, M.E. Gross, C.A. Coronado, G.L. Graff, I.N. Greenwell, and P.M. Martin. A new method for fabricating transparent barrier layers. *Thin Solid Films*, 290-291:63–67, 1996.

[222] P. F. Carcia, R. S. McLean, and M H Reilly. Permeation measurements and modeling of highly defective Al2O3 thin films grown by atomic layer deposition on polymers. *Appl. Phys. Lett.*, 97(22):221901, 2010.